ROYAUME DU MAROC
Université Mohammed V - RABAT -
جامعة محمد الخامس – الرباط –
Faculté des sciences
كلية العلوم
CENTRE D'ETUDES DOCTORALES - SCIENCES ET TECHNOLOGIES

N° d'ordre : 3376

THESE

En vue de l'obtention du : DOCTORAT

Structure de Recherche : Laboratoire de la Matière Condensée et Sciences Interdisciplinaires
Discipline : Physique
Spécialité : Matière Condensée et Modélisation des Systèmes

Présentée et soutenue le 21/11/2020

Par :

Rachida LAMOURI

Magnetic properties of spinel ferrites and M-type hexaferrites for permanent magnet applications

JURY

Abdelilah BENYOUSSEF	PES, Académie Hassan II des Sciences et Techniques-Rabat	Président
Abdelmajid AINANE	PES, Faculté des Sciences, Université Moulay Ismaïl -Meknès	Rapporteur/Examinateur
Abdallah EL KENZ	PES, Faculté des Sciences, Université Mohammed V-Rabat	Rapporteur/Examinateur
Noureddine MASAIF	PES, Faculté des Sciences, Université Ibn Tofail -Kénitra	Rapporteur/Examinateur
Omar MOUNKACHI	PA, Faculté des Sciences, Université Mohammed V-Rabat	Co-directeur de Thèse
Hamid EZ-ZAHRAOUY	PES, Faculté des Sciences, Université Mohammed V-Rabat	Directeur de Thèse

Année Universitaire : 2020/2021

Acknowledgements

First and foremost, All praises are to almighty **ALLAH (SWT)** who guides me when I bewilder in the darkness of ignorance and enlighten my ways.

This thesis work has been conducted at the Laboratory of Condensed Matter and Interdisciplinary Sciences (LaMCScI) of the Faculty of Science, University Mohammed V-Rabat under the supervision of professor **Hamid EZ-ZAHRAOUY** and the co-supervision of professor **Omar MOUNKACHI**, Assistant professor at Mohammed V University in Rabat, in collaboration with "Materials and Nanomaterials" Center at MAScIR Foundation, Rabat, Morocco.

During my thesis work, I received a lot of support from many people in different ways. I would like to take this opportunity to express my gratitude.

It is my privilege to express my deep sense of gratitude to my Supervisor, prof. **Hamid EZ-ZAHRAOUY** for his constant persuasion, valuable suggestions, constructive criticism and efficient supervision at each and every stage during my thesis. I would particularly like to thank him for the freedom of action he has given me at every stage of this thesis. I hope that I have been able to prove that I am deserving his trust and that this work is finally fulfilling his expectations.

I would also like to express my sincere thanks and gratitude to my co-supervisor prof. **Omar MOUNKACHI** who was available each time I need his help despite his many responsibilities.

I am indebted to prof. **Abdelilah BENYOUSSEF** for his erudite discussion, valuable suggestions and constructive advice throughout the progress of this research work. He was always ready to provide a straightforward explanation of the various concepts involved in the project and to be the president of the jury members of this thesis.

I would like to thank the thesis committee for reviewing my work and giving their insightful and useful comments. It is an honor for me that they agreed to judge this work.

I would like to thank prof. **Abdelmajid AINANE** from University Moulay Ismaïl-Meknès, Faculty of Sciences, for reporting and reviewing this thesis.

I would like to thank prof. **Abdallah EL KENZ** from University Mohammed V-Rabat, Faculty of Sciences, for reporting and reviewing this thesis.

I would like to thank prof. **Noureddine MASAIF** from University Ibn Tofail - Kénitra, Faculty of Sciences, for reporting and reviewing this thesis.

My sincere thanks also go to prof. **Mohammed HAMEDOUN** for his availability and the time he devoted to the project. I thank him for his encouragement and also for his daily good cheerfulness.

My thanks go also to Dr. **Frederic BOSCHINI** from GREENMAT, CESAM Research Unit, University of Liege, Belgium, for the very constructive remarks in the experimental part of my thesis project.

My thanks go also to Dr. **Abdelfettah MAHMOUD** from GREENMAT, CESAM Research Unit, University of Liege, Belgium, for his very constructive remarks in our collaboration in the experimental studies performed in this project.

I would like to thank the thesis committee for reviewing my work and giving their insightful and useful comments. It is an honor for me that they agreed to judge this work.

I would also like to thank prof. **El Mehdi SALMANI** for his help in my first steps towards research and his friendly guidance.

I would like to express my thanks to my colleagues at the faculty of Sciences of Rabat, in particular, Dr. **Zineb KERRAMI**, Dr. **Hanane ABSIKE**, Dr. **Anass SIBARI**, Dr. **Mohammed HAJJI**, Dr. **Abdelmjid KADIRI**, **Khadija DAOUDI**, **Nora BAAALLA**, **Oualid ARYBOU**, **Bouchra YAGOUTI**, **FatimaZahra NAINAA**, and my colleagues at MAScIR foundation, Dr. **Lahcen FKHAR**, **Aicha EL BOUKILI**, **Laila EL FOUJJI**, **Sara LAKHOUIL**, **Hafssa BOULENOUAR**, **Zineb EL KACEMI**, and Dr. **Siham DIFI** with whom I shared the good and bad moments of my PhD. Without forgetting my friends **Imane LAKHOUAJA**, **Amal MOUNTASSIR**, **Souad AFYLAL**, **Nawal LAMHAMSI** and **Sara EL MERZAK**.

I would like to point out that the experimental part of this project was done in col-

laboration with Materials and Nanomaterials Center at MAScIR foundation in Rabat, MOROCCO. My thanks go also to all Professors, Researchers, Engineers, administrative employees and PhD students and internships at MAScIR Foundation. Words cannot express my gratitude, nor my thanks for all your help and guidance. It has been a great honor to closely work with you.

I am really grateful to the MESRSFC (Ministère de l'Enseignement Supérieur, de la Recherche Scientifique et de la Formation des Cadres) for the financial support and giving me facilities to do my research works in the Framework of the national program PPR under contract no. PPR/2015/71.

Lastly, I am indebted to my family members. The love and prayers of my mother **Lalla Keltouma NAJI**, continuing support and guidance of my father **Mly Said LAMOURI**, my brothers **Mly Es-sddik** and **Mly Youssef** and my sweethearts and sisters **Saadia**, **Khadija**, **Fddila**, **Soumiya**, **Rajae** and **Aziza**. In fact, it is the result of their love, affection, encouragement and incredible support that enable me to accomplish this study. I would like to express my apologies to anyone that I did not mention his name.

Thank you all for your support without expecting any return

Abstract

Permanent magnet materials have attracted a lot of interest of researchers worldwide because of their use in many technological and industrial applications. The largest market of permanent magnets is essentially made up of rare-earth based magnets or ferrites magnets. However, it should be noticed that each permanent magnet application is particular and responds to specific needs and therefore to different conditions.

The present thesis work was focused on Cobalt spinel ferrites $CoFe_2O_4$ and M-type Strontium hexaferrites $SrFe_{12}O_{19}$, as potential candidates to replace rare-earth based magnets, by studying their structural, electronic and magnetic properties using a combination of theoretical and experimental investigations.

Our theoretical results based on density functional theory and Monte Carlo simulation showed the strong dependence of the magnetic properties of Cobalt spinel nanoferrites to the nanoparticles size and we extracted a theoretical value of the maximum energy product $(BH)_{max}$ of about 2.83 MG.Oe for cubic-shaped $CoFe_2O_4$ nanoparticles with an average particle size of 21 nm. Experimentally, the possibility to improve the maximum energy product $(BH)_{max}$ of M-type Strontium hexaferrites has been proved, by varying the synthesis methods with some common conditions, and through the preparation of hard/soft nanocomposites with the presence of the exchange-coupling behavior.

Keywords: spinel ferrites, M-type hexaferrites, Density Functional Theory, Monte Carlo simulation, Co-precipitation method, Sol-gel auto-combustion, Solid-State reaction, magnetic properties, Permanent magnet applications.

Résumé

Les matériaux pour aimants permanents ont suscité beaucoup d'intérêt de la part des chercheurs du monde entier en raison de leur utilisation dans de nombreuses applications technologiques et industrielles. Les aimants à base de terres rares ou de ferrites constituent le marché le plus large des aimants permanents. Cependant, il convient de noter que chaque application d'aimant permanent est particulière et répond à des besoins spécifiques et donc à des conditions différentes.

Le présent travail s'est concentré sur les ferrites spinelles "$CoFe_2O_4$" et les hexaferrites de type-M "$SrFe_{12}O_{19}$" en étudiant leurs propriétés structurelles, électroniques et magnétiques grâce à une combinaison d'étude théoriques et expérimentales. Nos résultats théoriques basés sur la théorie de la fonctionnelle de la densité et la simulation de Monte Carlo montrent la forte dépendance des propriétés magnétiques des ferrites spinelles de cobalt à la taille des nanoparticules et nous avons extrait une valeur théorique du produit énergétique maximal $(BH)_{max}$ d'environ 2,83 MG.Oe pour une taille moyenne de particule de 21 nm. La possibilité d'améliorer le produit énergétique maximal $(BH)_{max}$ des hexaferrites de Strontium de type-M a été prouvée expérimentalement en variant les méthodes de synthèse et en utilisant des nanocomposites durs/doux avec un comportement de couplage d'échange.

Mots clés: ferrites spinelles, hexaferrites de type-M, théorie de la fonctionnelle de la densité, simulation Monte Carlo, méthode de coprécipitation, sol-gel auto-combustion , réaction à l'état solide, propriétés magnétiques, applications des aimants permanents.

Résumé détaillé

Les ferrites spinelles de cobalt "$CoFe_2O_4$" et les hexaferrites de strontium de type-M "$SrFe_{12}O_{19}$" ont été considérés comme des candidats prometteurs pour remplacer les aimants à base de terres rares et les aimants en alliages intermétalliques dans les applications d'aimants permanents à faible énergie. Ces matériaux, comme étant des matériaux magnétiques durs, ont fait l'objet de nombreuses études en physique et en science des matériaux. Le défi pour les aimants en ferrite est qu'ils ne présentent pas simultanément une forte aimantation et une forte coercivité. Une coercivité élevée peut être obtenue soit par la haute anisotropie magnéto-cristalline intrinsèque des matériaux, soit par la taille fine des particules/grains. Alors que l'aimantation rémanente élevée nécessite une aimantation à saturation élevée et un degré élevé d'alignement des grains le long de l'axe magnétique facile.

L'objectif de notre thèse est de combiner des études théoriques et expérimentales sur les propriétés structurelles, micro-structurales, électroniques et magnétiques de $CoFe_2O_4$ et $SrFe_{12}O_{19}$. Nous avons cherché à comprendre l'origine des propriétés magnétiques de ces matériaux en étudiant leurs propriétés structurelles, électroniques et magnétiques à l'aide de différents outils numériques tels que la théorie de la fonctionnelle de la densité, l'approximation du champ moyen et la simulation de Monte Carlo. En outre, nous avons cherché à préparer facilement et à faible coût des ferrites et des nanoferrites ayant des propriétés magnétiques améliorées en étudiant dans un premier temps les effets des méthodes de synthèse, et par la suite la possibilité de préparer des nanocomposites dures/doux en assurant la présence du mécanisme de couplage d'échange entre les deux phases dures et doux.

En effet, nous avons commencé notre travail de thèse par une combinaison d'étude théorique et expérimentale des propriétés magnétiques du $CoFe_2O_4$. Une aimantation à saturation élevée (Ms) a été démontrée pour les ferrites spinelles de cobalt massif. Cependant, le système en vrac présente une faible coercitivité (Hc), ce qui donne un produit énergétique maximal faible $(BH)_{max}$ d'environ 0,02 MG.Oe d'après les mesures expérimentales et de 0,07 MG.Oe d'après la simulation de Monte Carlo. Pour surmonter

cette faiblesse de la coercivité, nous avons étudié les effets de la taille sur les propriétés magnétiques des nanoparticules simples de forme cubique "$CoFe_2O_4$" en utilisant la simulation de Monte Carlo. Nous avons constaté que la saturation et l'aimantation rémanente augmentaient avec l'augmentation de la taille des particules vers les valeurs de masse. En outre, la limite de taille à domaine unique est observée pour une taille d'environ 21 nm, où la performance des nanoparticules de forme cubique, en termes de $(BH)_{max}$, a atteint sa valeur maximale d'environ 2,83 MG.Oe à la température ambiante.

D'autre part, nous avons exploré les propriétés structurelles, micro-structurales et électroniques du $SrFe_{12}O_{19}$ afin d'améliorer ses propriétés magnétiques. Les effets de la méthode de synthèse sur les propriétés structurelles et magnétiques de ce matériau ont été étudiés en considérant deux méthodes simples, faciles et peu coûteuses, à savoir la coprécipitation et Sol-gel auto-combustion , avec les mêmes conditions de calcination. La pureté cristalline des échantillons obtenus a été confirmée par les rayons-X avec une taille de cristallite d'environ 37,8 nm pour les nanoparticules synthétisées par la méthode de coprécipitation, tandis que la méthode sol-gel auto-combustion donne lieu à des nanoparticules plus grandes avec une taille moyenne de cristallite d'environ 85,4 nm. Une aimantation de saturation et une aimantation rémanente élevées d'environ 95,11 emu/g et 46,39 emu/g, respectivement, ont été obtenues pour les nanoparticules préparées en utilisant la méthode sol-gel auto-combustion. De plus, il a été démontré que les nanoparticules de $SrFe_{12}O_{19}$ préparées par la méthode sol-gel auto-combustion présentent un produit énergétique maximal $(BH)_{max}$ d'environ 1,36 MG.Oe par rapport à l'échantillon préparé par la méthode de co-précipitation (1,13 MG.Oe). une étude théorique sur les effets de substitution sur les propriétés électroniques et magnétiques du $SrFe_{12}O_{19}$ a été effectué en se basant sur la DFT. Il a été constaté que l'insertion de l'élément Cobalt dans les sites de Sr conduit à l'amélioration du moment magnétique des hexaferrites de Strontium de 40,03 μ_B à 42,24 μ_B avec un changement clair du comportement électronique d'un caractère semi-conducteur à un caractère semi-métallique.

Le dernier chapitre de cette thèse concerne la préparation de $(SrFe_{12}O_{19})_{1-X}/(CoFe_2O_4)_X$ nanocomposites de différents rapports molaires (x= 0,05, 0,10, 0,20), où le matériau

$CoFe_2O_4$ a été utilisé comme matériau magnétique doux. Les ferrites de spinelle et les hexaferrites de type-M ont été préparés selon la méthode classique de coprécipitation, suivie d'un mélange physique pour la préparation des nanocomposites. La diffraction des rayons-X (XRD) a montré l'existence de phases mélangées de ferrite de spinelle et d'hexaferrite de type M, ce qui a été confirmé par les images de la microscopie électronique à balayage (MEB). Les cycles d'hystérésis magnétiques de tous les échantillons ont montré un bon comportement magnétique monophasé, ce qui prouve l'interaction ressort d'échange entre la phase magnétique douce $CoFe_2O_4$ et la phase magnétique dure $SrFe_{12}O_{19}$. De plus, le nanocomposite $(SrFe_{12}O_{19})_{0.95}/(CoFe_2O_4)_{0.05}$ a montré les valeurs les plus élevées de l'aimantation de saturation, de l'aimantation rémanente et de la coercivité d'environ 93,77 emu/g, 45,34 emu/g et 5,50 KOe, respectivement. Une amélioration du produit énergétique maximal est observée pour $(SrFe_{12}O_{19})_{0.95}/(CoFe_2O_4)_{0.05}$ d'environ 26,5 % par rapport à l'hexaferrite de Strontium pure $SrFe_{12}O_{19}$.

Nous croyons qu'un travail de recherche n'a jamais de fin, c'est pourquoi nous avons l'intention de continuer notre travail de thèse avec :

- L'introduction d'autres paramètres dans notre modèle Ising tels que les interactions inter-particules et l'orientation des nanoparticules afin de mieux comprendre les propriétés magnétiques des nanoparticules de forme cubique.

- modélisation et simulation d'autres formes de nanoparticules telles que les octaèdres et les sphères en utilisant la théorie fonctionnelle de la densité et la simulation de Monte Carlo.

Contents

List of Tables

List of Figures

List of abbreviations

Ms	Saturation magnetization
Mr	Remanent magnetization
Br	Remanent induction
$(BH)_{max}$	Maximum energy product
DFT	Density Functional Theory
GGA	Generalized Gradient Approximation
PBE	Perdew-Bruker-Ernzerhof
LSDA	Local Spin Density Approximation
KS	Khon Sham
MT	Muffin-Tin
APW	Augmented-Plane-Wave
LAPW	Linearized-Augmented-Plane-Wave
FP-LAPW	Full Potential Linearized-Augmented-Plane-Wave
MCS	Monte Carlo simulation
MAE	Magneto-crystalline anisotropy energy
K_B	Boltzmann constant
SSR	Solid-State reaction
CP	Coprecipitation
SG/AC	Sol-gel Auto-combustion
XRD	X-ray diffraction
SEM	Scanning Electron Microscopy
SQUID	Superconducting Quantum Interference Device
MPMS	Magnetic Properties Measurement System
CFO	$CoFe_2O_4$
SFO	$SrFe_{12}O_{19}$

General introduction

A permanent magnet is a material, which is initially magnetized and then creates its own persistent magnetic field in a particular volume of space, without the need for continuous electric power and thus no heat generation. The magnetic energy stored in the magnet is not drained away by its use and remains into the material indefinitely if it is properly made and handled. An efficient permanent magnet material should present high remanent induction (Br), high saturation magnetization (Ms), large coercive field (Hc) and a squareness ratio close as possible to one. The most important parameter of permanent magnet materials, which makes them essential for many applications is that they have the ability to maintain a large magnetic flux in the absence of an applied magnetic field. Thus, a permanent magnet is nothing else than an energy storage device, whose figure of merit is its maximum energy product $(BH)_{max}$ [1, 2].

Rare-earth based magnets manufacturing has been considered as a mature technology that requires high-performance magnets. Although, the economic and environmental issues related to the exploitation of rare-earth elements and the 2011 crisis of rare-earth elements require worldwide efforts to develop new magnets without rare-earth elements or containing little or heavy rare-earth elements [3, 4].

Therefore, rare earth free magnets have taken the interest of research groups worldwide to replace rare earth magnets in either high-energy as well as low-energy applications [5–7].

Ferrite magnets (known as ceramic magnets) have the lowest magnetic strength of all permanent magnetic materials with a maximum energy product range of 0.8 to 5.3 MG.Oe. However, they are the most economical to produce in large volumes, which is the reason why they are commonly used for high-volume commercial production cycles where space, and therefore the size of the magnet, is not a limiting factor [8] . For that, many research programs have been launched in order to enhance the magnetic properties of hard ferrites [9–11].

This thesis work is being carried out in the framework of a ministerial project in collaboration with Mohammed V University and MAScIR Foundation, where theoretical and experimental research works are closely performed together to understand and find

out the theoretical limits of the magnetic properties as well as optimizing the synthesis processes and conditions to achieve moderate properties and performance of Cobalt spinel ferrites $CoFe_2O_4$ and M-type Strontium hexaferrites $SrFe_{12}O_{19}$.

The theoretical research is performed based on a combination of Density Functional Theory (DFT) and Monte Carlo Simulation (MCS) to predict the electronic and magnetic properties of bulk $CoFe_2O_4$, to study the size effects on the $(BH)_{max}$ of cubic-shaped $CoFe_2O_4$ nanoparticles, and to study the stability, electronic and magnetic properties of Co-substituted $SrFe_{12}O_{19}$.

Density Functional Theory was used to determine the electronic and magnetic properties of the studied materials at 0K, especially the magnetic exchange interaction that are considered as the most important parameters to better understand the magnetic behavior of any material. The calculated exchange interactions are then used as input parameters in a Monte Carlo program, which consists of simulating the magnetic properties of materials at finite temperature. In this thesis work, we are interested in the magnetic hysteresis loop at room temperature to extract the maximum energy product, which is the key parameter to evaluate the performance of a permanent magnet.

Different synthesis routes have been used in this thesis work such as Solid-State Reaction, Co-precipitation and Sol-gel Auto-combustion methods to explore and to look for possible enhancement of the magnetic properties of bulk ferrites, nanoferrites and hard/soft nanocomposites.

This thesis is presented in two main parts :

The first part concerns the state of the art and basic concepts, which contains two chapters:

* ***Chapter 1:*** A general introduction to magnetism and the necessary guidelines to understand and study hard magnetic materials for permanent magnet applications are presented in this chapter.

* ***Chapter 2:*** This chapter focuses, in the first part, on the needed background of the computational methods, especially, Density Functional Theory and Monte Carlo Simulation for the calculations of the structural, electronic and magnetic properties that

are performed in this thesis work. The second part of this chapter focuses on the experimental techniques used for the synthesis and the characterization of the studied $CoFe_2O_4$ and $SrFe_{12}O_{19}$ materials.

The second part concerns the obtained experimental and theoretical results, presented in three chapters:

* ***Chapter 3:*** We explore in chapter 3 the magnetic properties of bulk and cubic-shaped $CoFe_2O_4$ nanoparticles. For bulk $CoFe_2O_4$ ferrite, we used the solid-state reaction to prepare the sample and then some characterization techniques for the structural, microstructural and magnetic characterizations. Density Functional Theory is used to study and discuss the electronic structure, the exchange coupling interactions and the magnetocrystalline anisotropy. To calculate the magnetic hysteresis loop the $(BH)_{max}$ of bulk $CoFe_2O_4$, Monte Carlo simulation is used with periodic boundary conditions and a large enough size of the system. For cubic-shaped $CoFe_2O_4$ nanoparticles, We used Monte Carlo simulation to study the size effects on the magnetic properties and take out the theoretical limits of the $(BH)_{max}$ of cobalt ferrite.

* ***Chapter 4:*** A possible improvement of the magnetic properties of M-type Strontium hexaferrites is presented in this chapter. In the first part, we studied the effect of the synthesis route on the magnetic properties by using two simple, easy and low-cost synthesis methods to prepare $SrFe_{12}O_4$ nanoparticles viz. Sol-gel auto-combustion and co-precipitation methods with some common conditions. The second part focused on the substitution effects on the electronic and magnetic properties of $SrFe_{12}O_4$ by using Density Functional Theory.

* ***Chapter 5:*** This chapter presents the exchange-coupling mechanism in hard/soft $SrFe_{12}O_{19}/CoFe_2O_4$ nanocomposite with a small content of the soft phase and the improvement of the energy product by $\approx 26\%$ compared to the parent M-type Strontium hexaferrite.

Part I

State of the art and basic concepts

Chapter 1

Magnetism and Permanent Magnet Materials

1.1 Introduction

This chapter presents the necessary guidelines for the study of hard magnetic materials for permanent magnet applications. These materials exhibit a spontaneous magnetization, which is irreversible with the application of an external magnetic field. The irreversibility of the magnetization is summarized in a magnetic hysteresis loop. A general introduction to magnetic materials and their classification regarding their behavior in the presence of an external magnetic field is given. Then, we will give a look on some basic concepts that classify ferromagnetic and ferrimagnetic materials into soft and hard magnetic materials. The last part of this chapter will be devoted to hard magnetic materials for permanent magnet applications.

1.2 Magnetic materials

1.2.1 Introduction to magnetic materials

Generally, since all substances (with a few exceptions) are made up of individual atoms or associated in molecules or ions, the electrons are not free (except for conduction elec-

trons in metals) but are located in orbitals. The movement of these charges around the nuclei constitutes a microscopic current responsible for an electronic magnetic moment. At the atomic, ionic or molecular level, the total moment is the vectorial sum of all the electronic moments and is worth a certain value.

On a macroscopic scale, the magnetic moment of a sample of matter is zero if the individual moments of atoms, ions or molecules are null. Otherwise, the thermal agitation constantly orients these dipoles in random directions, with equal probability for all orientations making the sum of the vectors zero. Thus, no environment shows spontaneous magnetization when the temperature is high enough.

The introduction of an exciting magnetic field disturbs the electronic movements and changes the magnetic moment of each electron. So that the total magnetic moment can take on a non-null value.

Magnetic materials are classified into five types based on their behavior in the presence and the absence of an external magnetic field

1.2.1.1 Diamagnetic materials

When all electrons in a material subjected to a magnetic field are oriented in the opposite direction to the applied magnetic field, the magnet and the material repeal each other. This is called “diamagnetism”.

Diamagnetic materials are materials that contain only non-magnetic atoms; the magnetization is then induced by the applied magnetic field and disappears when this field is no longer present (see figure 1.1).

1.2.1.2 Paramagnetic materials

In paramagnetic materials, the atoms carry a magnetic moment whose orientation is random. The inter-atomic or inter-molecular distances are larger enough that the moments do not interact with each other.

As we can see in figure 1.2. In the absence of an external field, paramagnetic materials are only subjected to thermal agitation and the overall magnetization is zero. In the

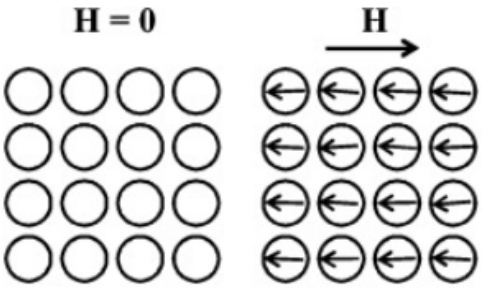

Figure 1.1: Diamagnetic material: In the absence of the external magnetic field (H = 0), the atoms or molecules do not have magnetic moments. In the presence of the external magnetic field (H ≠ 0), the external field induces moments in the opposite direction [12].

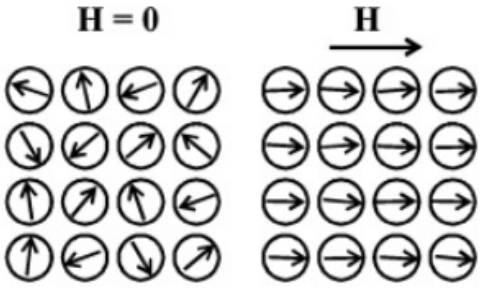

Figure 1.2: Paramagnetic material in the absence of the external magnetic field (H = 0) and in the presence of the external magnetic field (H ≠ 0) [12].

presence of a magnetic field, the average orientation of the moments changes under the effect of the torque that brings them back according to both direction and orientation of the field. Therefore, appearance of induced magnetization parallel to the magnetic field.

1.2.1.3 Antiferromagnetic materials

Antiferromagnetic materials are materials that spontaneously align their magnetic moments antiparallel when an external magnetic field is applied or temperatures below a critical temperature called "Néel Temperature T_N" [13].

The magnetization of an antiferromagnetic material remains constant below T_N and the material retains its antiparallel alignment when the external field is removed (figure 1.3).

1.2.1.4 Ferromagnetic materials

Ferromagnetic materials contain atoms or molecules that each have an individual magnetic moment and interact with closest neighbors with a positive exchange coupling lead-

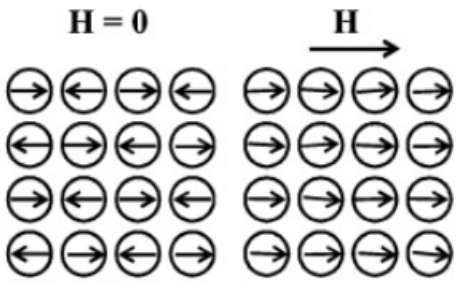

Figure 1.3: Antiferromagnetic material in the absence of the external magnetic field (H = 0) and in the presence of the external magnetic field (H ≠ 0) [12].

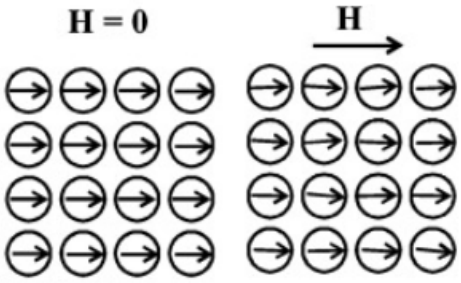

Figure 1.4: Ferromagnetic material in the absence of the external magnetic field (H = 0) and in the presence of the external magnetic field (H ≠ 0) [12].

ing to a collective alignment on micrometer domains called "Weiss domains" with variable direction of magnetization from one domain to another due to the thermal agitation [14].

In the presence of an external magnetic field, an induced magnetization parallel to the applied field appears. By removing the external field, the domains partially regain their independence, but the residual magnetocrystalline interactions ensure that the magnetic moments of each domain remain partially aligned with the initial field (remanent magnetization) which disappears if the temperature increases or if a new field of the opposite direction is applied (see figure 1.4).

1.2.1.5 Ferrimagnetic materials

Ferrimagnetism is the magnetic property of materials having atomic moments aligned in opposite directions like antiferromagnetic materials. The opposing moments in these materials are unequal. Thus, the material can spontaneously be magnetized. A well-known material, which shows ferrimagnetism, is magnetite. Most of the iron oxides show ferrimagnetic behavior because these compounds have complex crystal structures.

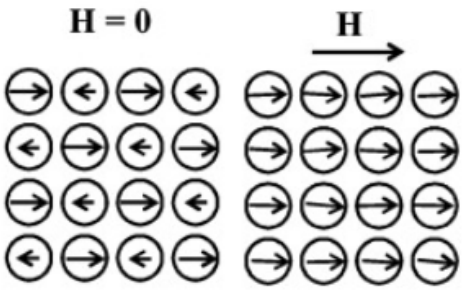

Figure 1.5: Ferrimagnetic material in the absence of the external magnetic field (H = 0) and in the presence of the external magnetic field (H ≠ 0) [12].

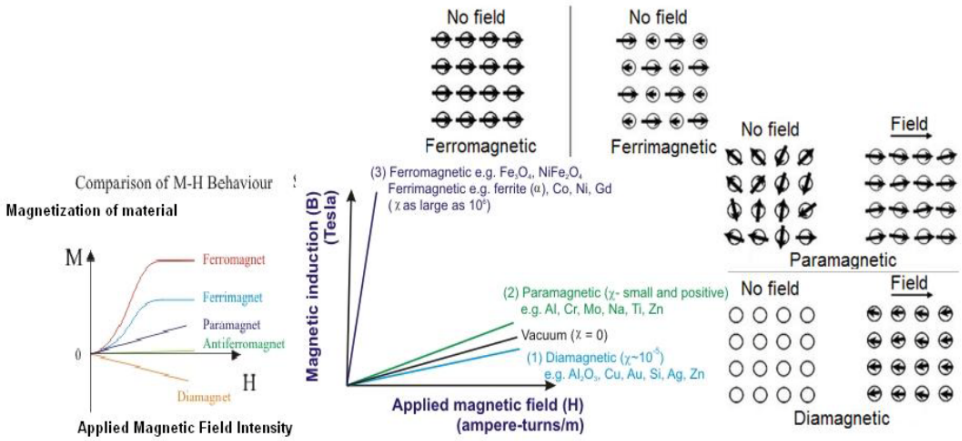

Figure 1.6: Classification of magnetic materials and comparison of magnetization behavior of each class [15].

Ferrimagnetic materials, such as ferrites, exhibit a magnetic behavior just like ferromagnetic materials. They also have temperature dependence of magnetization characterized by the Curie temperature T_C. Typically; ferrimagnetic materials have a high magnetization at room temperature.

Ferrimagnetic materials consist of magnetically saturated domains and exhibit magnetic saturation with a paramagnetic behavior above T_N. They behave similarly to ferromagnetic materials in terms of basic characteristics (figure 1.5).

To summarize, the response of the intrinsic magnetic dipole and the net magnetization in the presence and absence of an applied magnetic field are the key parameters to classify the magnetic materials as presented in figure 1.6.

As ferromagnetic materials are used in a wide range of technological applications. We will discuss more this type of materials according to its magnetic hysteresis loop in the

next section.

1.2.2 Classification of ferromagnetic materials

In this section, we will discuss the basic concepts and definitions of a magnetic hysteresis, and we will see briefly the two categories of ferromagnetic materials depending on the shape of the magnetic hysteresis loop, which are: Soft magnetic materials and Hard magnetic materials

1.2.2.1 Magnetic hysteresis

The hysteresis loop is the response curve of magnetic materials, through which they keep the memory of all their previous magnetization states through the elementary domains [16]. It was J. A. Ewing who showed this specific behavior in the case of Iron, and he called it "hysteresis" [17], which means delay of the effect over the cause (here, magnetization over the applied field).

The hysteresis loop of a ferromagnetic material depends on the mobility of the Bloch walls, which in their turn depend on the magnetic energies and the applied field [18]. Therefore, it can be considered as a characteristic of the material and in any case a very detailed and necessary mathematical method. Hysteresis is the delay in magnetization and the duplication of the B(H) characteristic of the magnetic material [19]. So, the hysteresis loop can be simply defined as the induction plot as a function of the applied external field H.

$$B = \mu_0(H + M) \tag{1.1}$$

Where B, M, H and μ_0 represent the induction, the magnetization, the applied magnetic field and the vacuum permeability, respectively.

The curve of the first magnetization and the hysteresis loop are the most important properties of ferromagnetic materials. Indeed, most technological applications are based on the existence of the hysteresis cycle.

First magnetization curve:

When an external magnetic field H is applied to a ferromagnetic material, the magnetic

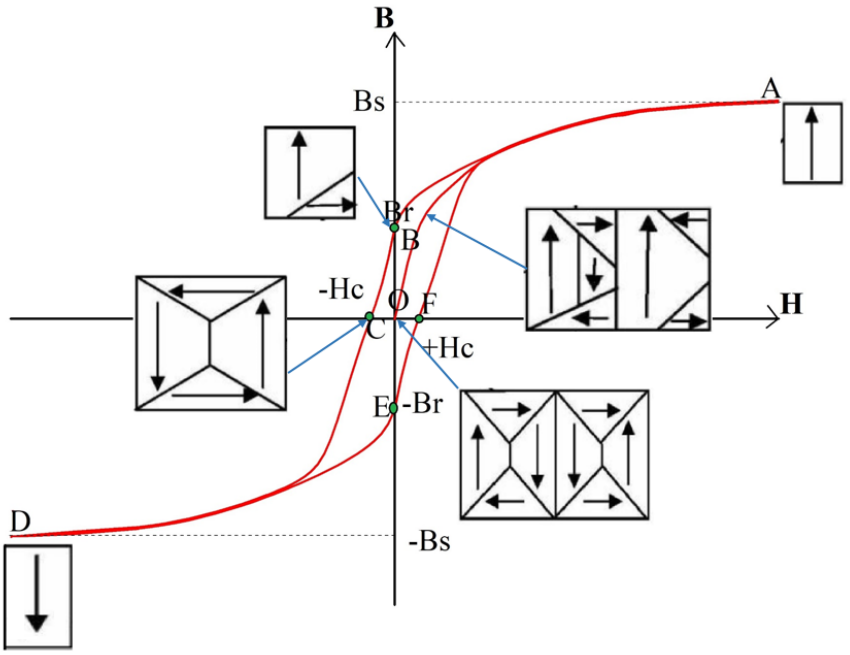

Figure 1.7: B-H hysteresis loop of a ferromagnetic material showing the first magnetization curve (OA) and the hysteresis cycle (ABCDEFA).

domains, whose orientation is close to that of the field H, increase at the detriment of those whose orientation is opposite to that of H. Therefore, the Bloch walls move within the material. At the limit, when the external magnetic field reaches a critical value Hs, the single crystal is only made up of a single ferromagnetic domain whose orientation is the same as that of H; the induction then reaches a maximum value, Bs, called "saturation induction" [20]. The OA line of the curve in figure 1.7, which is called "the first magnetization curve", represents this phenomenon.

Hysteresis loop:

When the intensity of the applied field H decreases to zero, the magnetic domains tend to reappear (AB curve, figure 1.7). However, since the displacement of the Bloch walls is not instantaneous due to the magnetic anisotropy; a non-zero induction Br occurs in the material (point B, figure 1.7), this Br value is called "remanent induction". In fact, a magnetic field in the opposite direction to the field of first magnetization must be applied for the induction to be zero (BC curve, figure 1.7). The Tc value of the field that generate this null induction corresponds to the coercive force (point C, figure 1.7). As the field strength H increases, the induction reaches again the maximum value

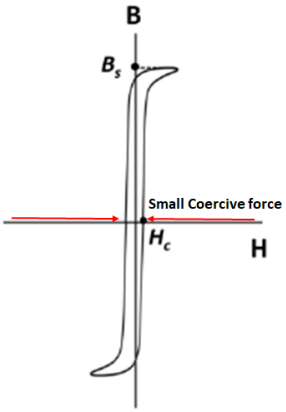

Figure 1.8: B-H hysteresis loop of a soft ferromagnetic material [24].

Bs (CD curve, figure 1.7). Finally, when the direction of the field is changed and its intensity is varied, the DEFA curve is obtained (figure 1.7). The obtained magnetization curve is then a hysteresis loop or hysteresis cycle (ABCDEFA, figure 1.7) whose main characteristic parameters are Bs, Br and Hc [21].

1.2.2.2 Soft magnetic materials

Soft magnetic materials are materials in which the coercive field is low (usually less than 1000A/m). For these materials, when the external field varies, there must be no obstacles to prevent the movement of the Bloch walls and the reorientation of the magnetic domains. In other words, these materials have few defects in their crystalline structure, as well as reduced anisotropy [22, 23].

Soft magnetic materials are characterized by a very high permeability, high saturation induction Bs, low coercive field Hc and low hysteresis losses (low surface area of the hysteresis loop as shown in figure 1.8) [24].

A soft magnetic material is used when it has to conduct a variable magnetic flux at high frequencies. The magnetic material must react quickly and strongly to small changes in the inductive field without heating up or being too sensitive to the field frequency. For this purpose, soft magnetic materials are used in the cores (or magnetic circuits) of transformers, motors and generators, in precision inductors in electronic circuits, magnetic shields and many other applications [25, 26].

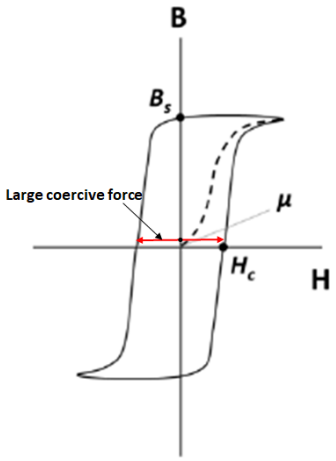

Figure 1.9: B-H hysteresis loop of a hard ferromagnetic material [24].

1.2.2.3 Hard magnetic materials

A high coercive field (generally above 10KA/m), high remanent induction and a large hysteresis loop characterize hard magnetic materials. In these materials, the reorientation of the magnetic moments in the Weiss domains and the displacement of the Bloch walls are sought to be minimally hindered [27, 28]. Thus, a good quality of permanent magnet will be characterized by a high value of the magnetic anisotropy, which is required for the persistence of an important part of the spontaneous (remanent) magnetization and the high value of the coercive field (figure 1.9) [24, 29].

Hard magnetic materials are used when the magnetic field generated by the material is stable over time and, if possible, remains high. The same applies in the presence of stray external magnetic fields [30]. This type of materials can be used in permanent magnets and lifting magnets applications, loudspeaker cores, low-power electric motors, magnetic lenses for cathode ray tube and other applications [31].

In the present thesis, we are interested to study hard magnetic materials for permanent magnet applications. For that, we will discuss in the next section, the basic characteristic of permanent magnets, their applications and a brief description of the basic families of permanent magnet materials.

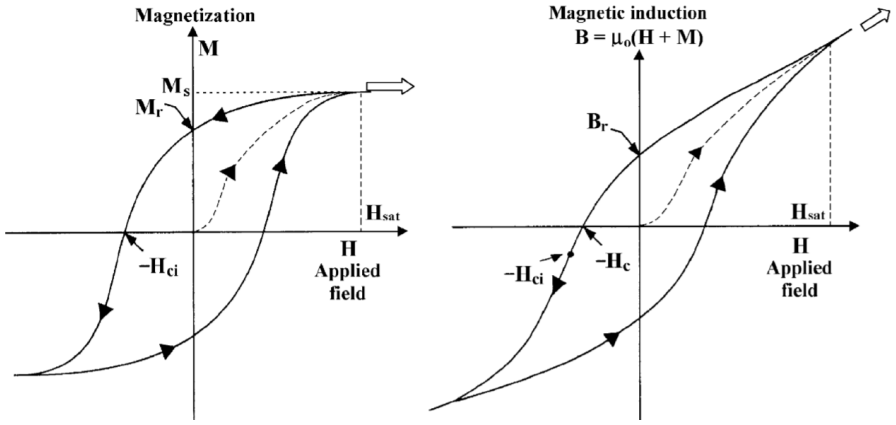

Figure 1.10: Magnetization and magnetic induction as a function of the applied magnetic field [32].

1.3 Permanent magnet materials

1.3.1 Definitions and Basic characteristics

Permanent magnets are the main feature of a wide variety of applications all over the world. The increased interest and necessity of these materials arises from their ability to transform the magnetic force of attraction or repulsion into mechanical work, and to convert mechanical energy into electrical energy. All these advantages allow their use as consumer products in transportation devices and renewable energy technologies. However, there is a need for small magnets with moderate magnetic energy, whose production is inexpensive and environmentally friendly, which has been the reason for numerous researches. In this section, we will first look at what a permanent magnet is and what are its basic characteristics before addressing to the family of permanent magnet materials and their applications.

A permanent magnet is a material, which is initially magnetized and then creates its own persistent magnetic field in a particular volume of space, without the need for continuous electric power and thus no heat generation. The magnetic energy stored in the magnet is not drained away by its use and remains into it indefinitely if it is properly made and handled. An efficient permanent magnet materials should presents high remanent induction (Br), high saturation magnetization (Ms), large coercive field (Hc) and a squareness ratio close as possible to one as presented in figure 1.10 [29–32].

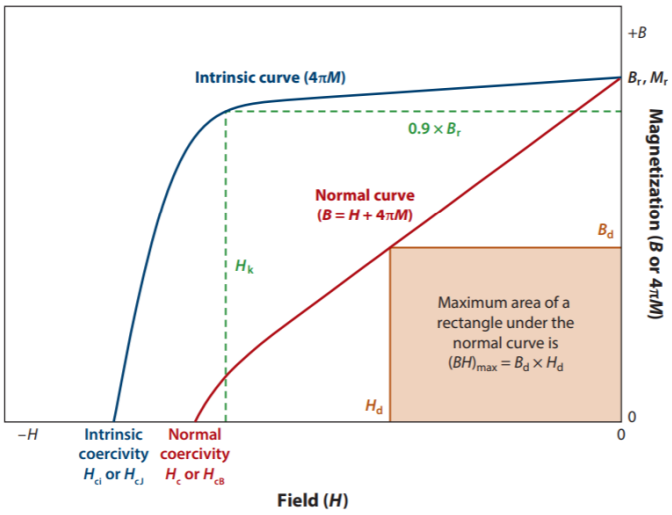

Figure 1.11: The second-quadrant demagnetization curves for a permanent magnet obtained in a decreasing field after saturation in the +H direction [35].

Thus, a permanent magnet is nothing else than an energy storage device, whose figure of merit is its energy product, $(BH)_{max}$. It is a measurement for the maximum amount of magnetic energy stored in a magnet. It is the maximally attainable product of flux density B and field strength H for a hard magnetic material [33, 34].

It concerns the product, maximally attainable with a magnetic material, made out of flux density B and field strength H. Experimentally, the maximum energy product $(BH)_{max}$ can be described as the maximum area swept by a rectangle in the second quadrant of a B-H hysteresis loop as shown in figure 1.11 [35]. Theoretically, the $(BH)_{max}$ is calculated using the following formula [36, 37]:

$$(BH)_{max} = (\mu_0 B_r^2)/4 \tag{1.2}$$

Where μ_0 is the vacuum permeability ($\mu_0 = 1$ in the CGS system of units) and Br is the remanent induction.

The maximum energy product is an indicator of magnet strength. You can use either a small magnet with a higher energy product or a large magnet with a lower energy product for the same application.

It should be noticed that each permanent magnet application is particular and responds

to specific needs and therefore to different conditions. Thus, when it comes to the basic characteristics of a good permanent magnet, it is impossible to find a definitive answer. Parameters such as temperature stability, flux density, energy product, physical strength and corrosion, cost of raw materials and availability, as well as the size and the weight of the product should be taken into account when choosing a magnetic material [38–40].

1.3.2 Family of permanent magnet materials

The permanent magnet family consists, in general terms, of rare-earth magnets and non-rare-earth based magnets classified generally, into two types of magnets: Alnico and Ceramics. In this sections, a brief introduction to these families will be given.

1.3.2.1 Rare-earth magnets

Rare earth elements are ferromagnetic and can be magnetized. However, as most of the rare earth elements have low Curie temperatures, these elements are magnetic only at low temperatures. To enhance their natural magnetic properties, most of them form compounds with transition metals such as iron, nickel and cobalt, which have higher Curie temperatures [41–43].

Samarium-Cobalt (Sm-Co) and Neodymium-Iron-Boron (Nd-Fe-B) magnets, collectively known as rare-earth magnets, have taken a great interest for technologies that require highly coercive permanent magnets [44–50]. Figure 1.12 presents the crystalline structure of Sm-Co with the three basic structures according to the stoichiometry and the crystalline structure of $Nd_2Fe_{14}B$ materials [51].

Samarium-Cobalt magnets were the first discovered rare-earth type magnets by Karl J. Strnat in 1966. They are essentially composed of an alloy of samarium, cobalt, iron, copper, hafnium, zirconium and praseodymium [52, 53]. Sm-Co were the strongest magnets, until 1980's when Dr. John Croat of General Motors and Dr. Masato Sagawa of Sumitomo Special Metals discovered Neodymium-based magnets [54, 55]. They provide about two-thirds of the strength of a neodymium magnet of the same size [56, 57]. Samarium cobalt magnets excel in high temperature and humid environments because they have

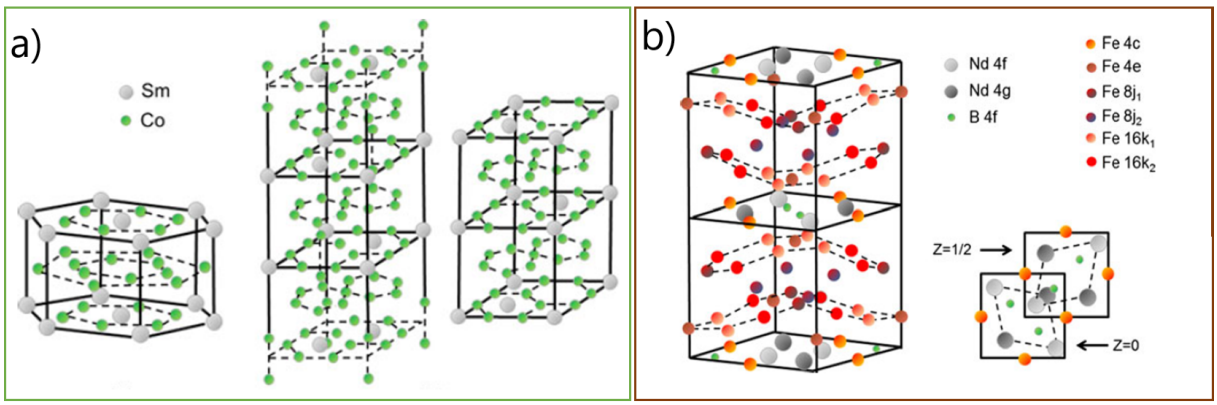

Figure 1.12: (a) Basic crystal structures of Sm-Co magnet (left) near the 1-5 stoichiometry: ($CaCu_5$-type), 2-17 stoichiometry: rhombohedral Th_2Zn_{17}-type structure (center), hexagonal Th_2Ni_{17}-type structure (right). (b) The crystal structure of $Nd_2Fe_{14}B$. A view looking down the tetragonal c-axis is shown on the right [51].

superior corrosion resistance and have a maximum operating temperature of at least 250 degrees Celsius [58–60].

Since their discovery in 1982, Neodymium-Iron-Boron (Nd-Fe-B) magnets took the title of the strongest magnets available on the market and are incredibly resistant to demagnetization. Surprisingly, a Neodymium-based magnet can support 1000 times its own weight. However, standard grades have a maximum operating temperature of 80 degrees Celsius and are not suitable for humid environments unless they are coated with a corrosion resistant coating [61–66]. Commercially, Neodymium-based magnets are classified into eight standard grades according to the amount of the rare-earth elements in the alloy mixture and their maximum energy product $(BH)_{max}$.

As presented in figure 1.13, more than 80 % of the world's production of rare earth metals originating in China with major use in catalyst and magnet applications [67]. Although, the economic and the environmental issues related to the exploitation of rare earth elements require major efforts worldwide to develop new hard magnets containing little or no rare earth (or heavy rare earth) [6, 7].

Thus, rare earth free magnets have taken the interest of research groups worldwide to replace rare earth magnet in either high-energy applications as well as low-energy applications. Rare earth free magnets family can be divided into two major types, intermetallic

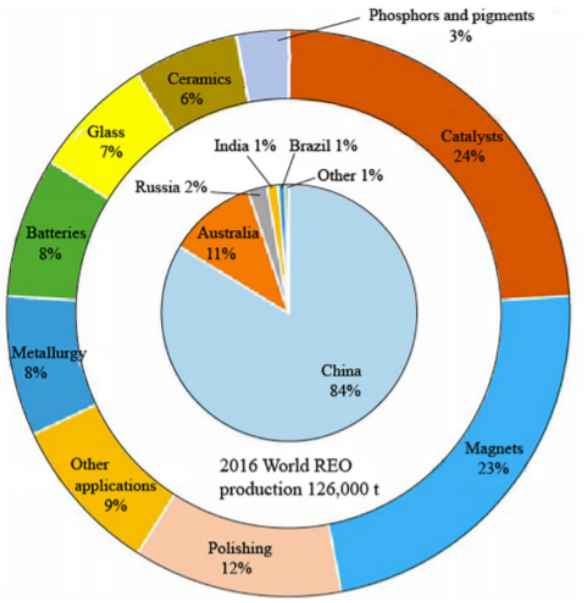

Figure 1.13: Global rare earth production and consumption by market and application in 2016 [67].

alloys and ceramics (hard ferrites), which will be discussed in the next section.

1.3.2.2 AlNiCo magnets

A variety of intermetallic magnets has been developed by combining different transition metals. In this section, we will be focused on Alnico type magnets because of their interesting properties required for wide range of permanent magnet applications.

Alnico magnets are primarily made up of assembly of Aluminum (Al), Nickel (Ni) and Cobalt (Co) elements in the transition group, but they can also contain elements such as Copper (Cu), Iron (Fe) and Titanium (Ti). As it is shown in figure 1.14, they were the strongest magnets available in the market before the development of rare earth Sm-Co magnet in 1966. This category of magnets is not powerful as rare-earth magnets in term of the maximum energy product. Although, it took a place in the market because of its remarkable temperature stability, its good mechanical properties and most importantly its high operating temperature that is required for many applications such as electric motors, guitar pickups, sensors, aerospace applications and others [68–70].

The magnetic strength of Alnico magnets raises from its high coercivity, due to a phase separation in the cast alloy into ferromagnetic FeCo-rich and weakly magnetic NiAl-rich

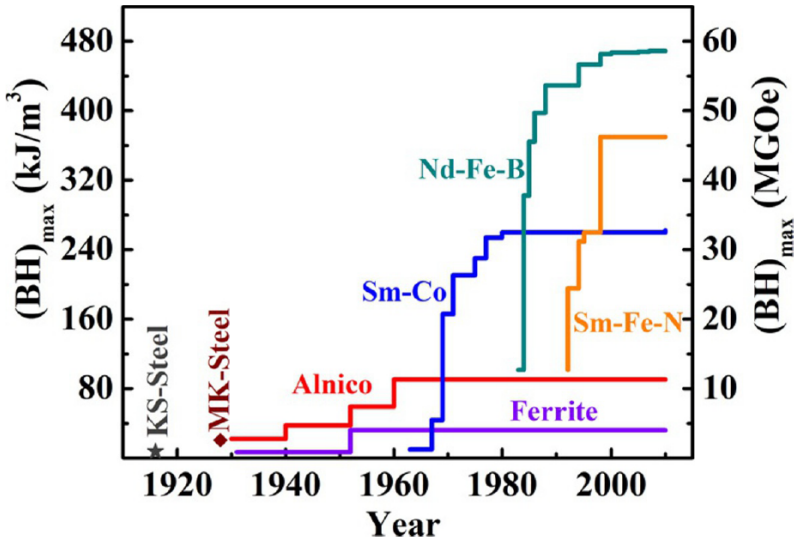

Figure 1.14: Development of permanent magnet families in time [7].

phases precipitated from the high-temperature homogeneous composition, rather than the magnetocrystalline anisotropy, which is the case of rare-earth permanent magnets [68, 71].

The main limitation of the Alnico materials is that they are easily demagnetized by a stronger or opposite magnetic field; even forcing two repelling Alnico magnets together can weaken their magnetic performance. To counteract this, it is normal for Alnico magnets to be manufactured so that their length is five times their diameter (width for block magnets), because a magnet with a higher length to diameter ratio has more resistance to demagnetization than a magnet with a lower length to diameter ratio [72, 73].

1.3.2.3 Hard ferrites:

Ferrite magnets (known as ceramic magnets), have the lowest magnetic field strength of all permanent magnetic materials with a maximum energy product range of 0.8 to 5.3 MG.Oe [74–76]. However, they are the most economic to produce in large volumes, which is the reason why they are commonly used for high-volume commercial production cycles where space, and therefore the size of the magnet, is not a limiting factor. M-type hexa-ferrites magnets are the most popular and manufactured oxide magnets as they provide the best magnetic properties [77–79]. However, Cobalt spinel ferrites have attracted the interest of many research groups because of its stability over time, easy synthesis route

with low cost and the possibility to improve their magnetic properties to be suitable for many technological applications [80, 81]. In this part, we will discuss the structural and the magnetic properties of M-type hexaferrites and Cobalt spinel ferrites magnets.

As presented in figure 1.15, the crystal structure of M-type hexaferrites is made up of altered cubic block S with a spinel-type structure, and a hexagonal block R containing the transition metal M^{2+} (Sr, Ba or Pb). It consists of 64 ions per unit cell on 11 different symmetry sites in a hexagonal structure with the space group P63/mmc. Each unit cell contains 38 oxygen ions occupying 4f, 4e, 6h and 12k sites; 2 metal cations (Sr^{2+}, Ba^{2+} or Pb^{2+}) occupying the 2d sites; and 24 ferric ions Fe^{3+} distributed over five different crystallographic sites: one tetrahedral site ($4f_1$), one trigonal bi-pyramidal site (2b) and three octahedral sites (12k,2a and $4f_2$). The net magnetic moment of the M-type hexaferrites compound comes essentially from the spins distribution of the ferric ions (Fe^{3+}) over the five crystallographic sites. Hence, the spins in the 2a, 2b, and 12k sublattices are parallel to each other in the upward direction, and anti-parallel to those of the $4f_1$ and $4f_2$ sublattices, which are in the downward direction [82–85].

Hard magnetic hexagonal ferrites with the general formula $MFe_{12}O_{19}$ (M=Pb,Sr,Ba) have been extensively used as permanent magnets, magnetic recording media, magneto-optic materials, as materials with potential catalyst and medical applications [86–88]. Pb-based hexaferrites compounds are not commercialized because of the toxicological reasons. While Barium and Strontium hexaferrites (referred as Ba-M and Sr-M) have attracted a great attention because of their interesting properties such as low manufacturing cost, high magneto-crystalline anisotropy, high Curie temperature, high coercivity and relatively high saturation magnetization, as well as excellent chemical stability and corrosion resistivity required for permanent magnet applications.

Other structural category of ferrites, which is the spinel ferrites, has attracted the attention of researchers for many years. Spinel ferrites materials, having the general formula AFe_2O_4, crystallize in the face-centered cubic system of oxygen ions, with the presence of two types of interstices, tetrahedral and octahedral sites, which can be filled by the metal ions. According to the distribution of metal cations among the tetrahedral

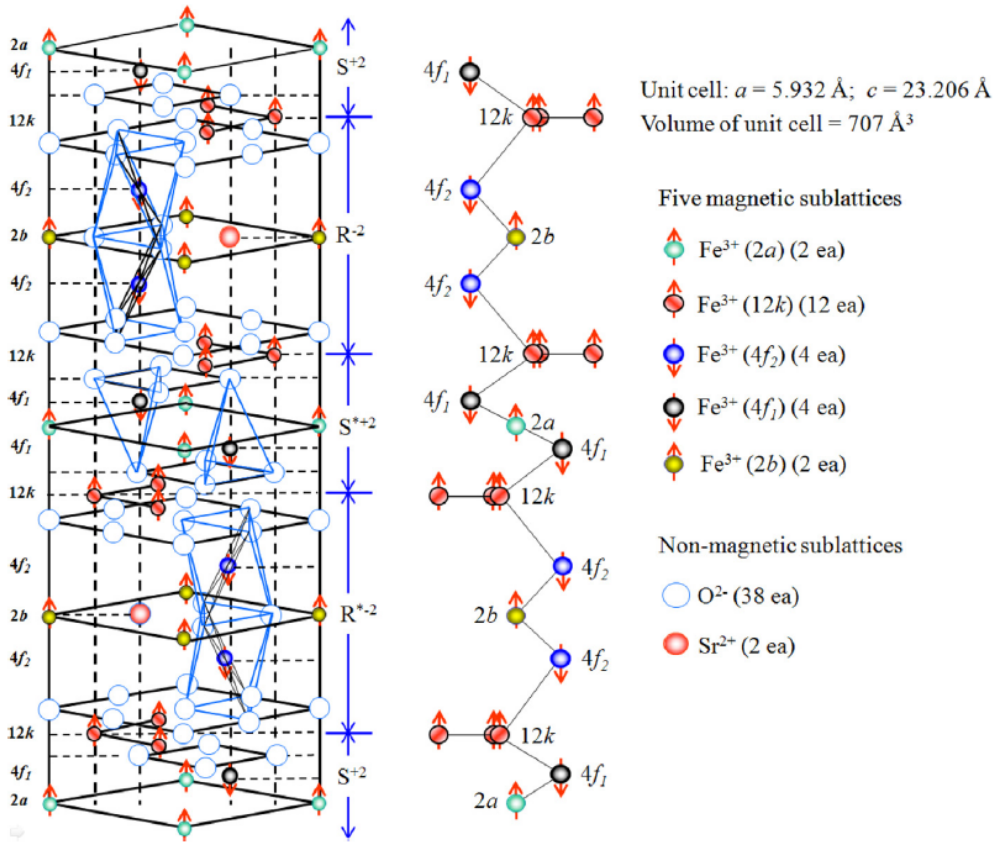

Figure 1.15: The unit cell (left), spin configurations of Fe^{3+} at each layer (middle), and lattice constants and number of Fe^{3+} at each sublattice (right) for $SrFe_{12}O_{19}$ [36].

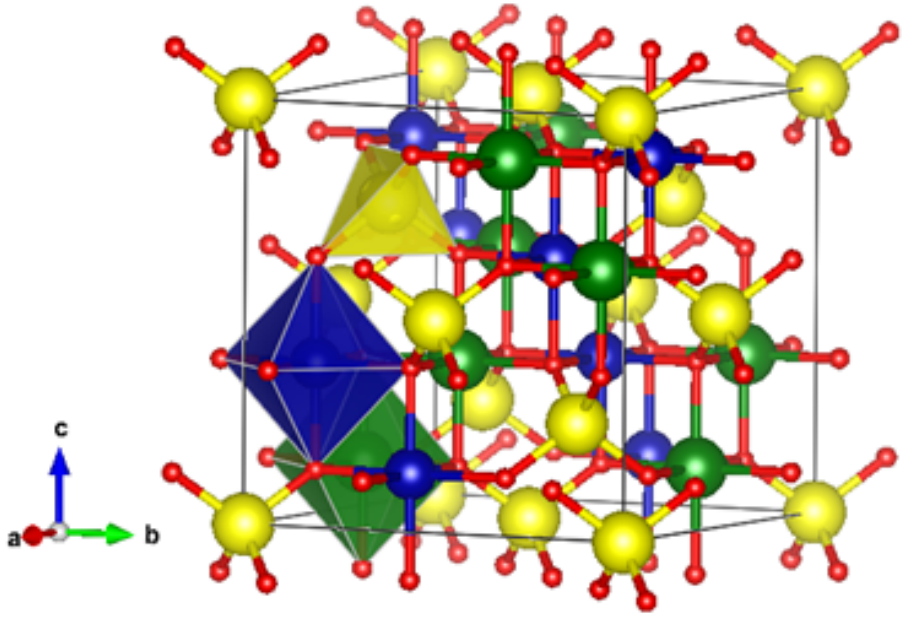

Figure 1.16: The unit cell of $CoFe_2O_4$ spinel ferrite. Colored spheres surrounded by Oxygen atoms forming tetrahedral sites (Yellow spheres represent Fe^{3+}) and octahedral sites (represented by Green and blue spheres for Fe^{3+} and Co^{2+} ions respectively) [92].

and octahedral sites, we distinguish between three categories of spinel ferrites (i.e. normal spinel ferrite, mixed spinel ferrites and inverse spinel ferrites), which largely changed the magnetic properties of the system [89–91].

Cobalt ferrite belongs to the spinel ferrite family, which crystallizes in the cubic structure with the $Fd\bar{3}m$ space group (N° 227) and lattice constant of about 8.40 Å. The optimized cationic distribution is found to be the inverse spinel structure, where the tetrahedral sites are mostly occupied by Fe^{3+} cations, while the octahedral sites are equally shared between Fe^{3+} and Co^{2+} as it is presented in figure 1.16 [92–94].

This material, as a category of ferrimagnetic ceramics, has been considered as a promising candidate for permanent magnet applications because of its interesting properties such as high coercivity, significant saturation magnetization, and easy synthesis route with low cost and good chemical stability that can be competitive to the M-type hexaferrites magnets.

In the present thesis work, we are interested to the hard ferrites family, especially M-type strontium hexaferrites and cobalt spinel ferrites for permanent magnets applications.

1.3.3 Applications of permanent magnets

As it is shown in figure 1.17, permanent magnet applications can be divided into four categories [95–97]:

Category 1: Applications that use the magnetic field of the permanent magnet to convert electrical energy to mechanical energy. Some of these applications are:

- Motors
- Meters
- Loudspeakers
- Relays
- Actuators, linear, and rotational

Category 2: Applications that use the magnetic field of the permanent magnet to convert mechanical energy to electrical energy. Some of these applications are:

- Magnetos
- Generators and alternators
- Eddy current brakes (used widely for watt-hour meter damping. This application could be listed under electrical to mechanical energy conversion; but as mechanical energy is used to create the eddy currents, it is often discussed with this group)

Category 3: Applications that use the magnetic field of the permanent magnet to direct, shape and control electron or ion beams. Some of these applications follow:

- Magnetic focused cathode-ray tubes
- Traveling Wave Tubes
- Ion Pumps
- Cyclotrons

Category 4: Applications that use the attractive and/or repelling force of the magnet, i.e., the attraction between a magnet and a soft magnetic material, such as a piece of iron or steel, or the attraction or repulsion between two magnets, is used to do mechanical

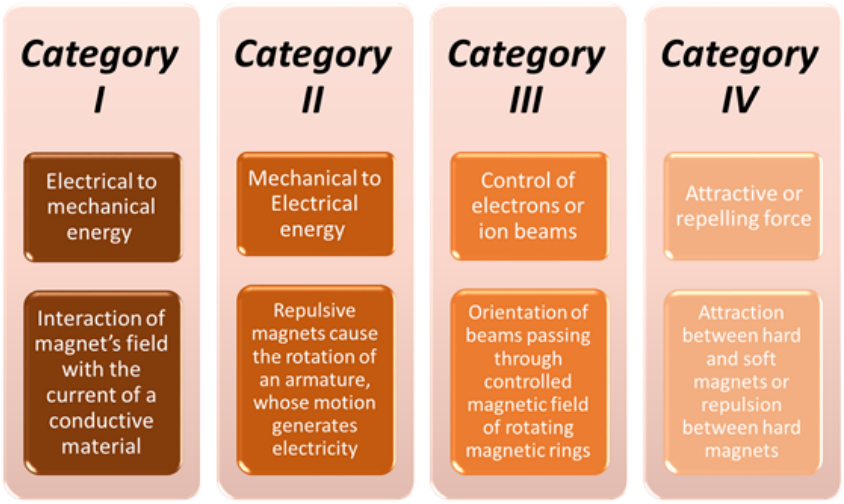

Figure 1.17: Categories and principal functions of permanent magnets.

work. The following applications are in this category:

- Magnetic separators, magnetic holding devices, such as magnetic latches.
- Magnetic torque drives
- Magnetic bearing devices

1.4 Conclusion

To conclude, permanent magnets have taken an important part in our daily life. They are found in everywhere in modern technologies. In this chapter, we presented the basic concepts needed to understand the characteristics of a permanent magnet, some of their current applications and the general and well commercialized families of permanent magnet materials.

Chapter 2

Computational methods and Experimental techniques

2.1 Introduction

In this chapter, we will present the computational methods and the experimental techniques used during this thesis work: Density Functional Theory, Monte Carlo Simulation, different synthesis methods and the characterization techniques.

The hard magnetic materials in which we are interested in this thesis are Cobalt spinel ferrites and M-type strontium hexaferrites. Density Functional Theory was used to determine the electronic and magnetic properties of the studied materials at 0K, especially the magnetic exchange interactions that are considered as the most important parameters to get the magnetic behavior of any materials.

The calculated exchange interactions are then used as input parameters in our Monte Carlo program, which consists of simulating the magnetic properties of materials at finite temperature. In this thesis work, we are interested, especially, in the magnetic hysteresis loop at room temperature to extract the maximum energy product, which is the key parameter to evaluate the performance of a permanent magnet.

To synthesize our simulated materials, we used the Solid-state reaction to prepare bulk material, and two synthesis methods to prepare nanoparticles, which are the coprecipita-

tion method and the sol-gel auto-combustion method.

The obtained materials are subjected to several characterization techniques to characterize their structural, microstructural and magnetic properties.

2.2 Density Functional Theory

2.2.1 Introduction to Density Functional Theory

Density functional theory (DFT) is one of the most commonly used quantum methods in the fields of solid-state physics and quantum chemistry for the determination of the physical and quantum quantities of a given system, in particular, systems containing a large number of electrons.

DFT was established on the basis of the theoretical formalism proposed by Pierre Hohenberg, Walter Kohn and Lu Sham in the mid-1960s [98–100]. This formalism is based on Quantum mechanics and involves only a limited number of input data. For a given multi-body system, it allows the Schrödinger equation to be solved dealing only with electron density instead of the all-electron wave function.

In this section, we will present the fundamentals and approximations of the density functional theory (DFT). First, it is necessary to define the equations involved in a system made of nuclei and electrons and leading to the development of the Kohn-Sham equation.

2.2.1.1 Schrödinger equation

Material is a set of atoms containing nuclei and electrons interacting with each other. To study all these interactions, Schrödinger proposed an equation describing a particle by its wave function $\psi(\vec{r}, t)$ [101, 102]:

$$\hat{H}\psi(\vec{r}, t) = -i\hbar\frac{\partial\psi(\vec{r}, t)}{\partial t} \tag{2.1}$$

Where $\hat{H}$ is the Hamiltonian of the system:

$$\hat{H} = -\frac{\hbar^2}{2m}\nabla^2 + \hat{V}(\vec{r}, t) \tag{2.2}$$

The first term corresponds to the kinetic energy, the second one to the potential.

In our case, we will use the stationary equation [103], which for a system with N-electrons and M nuclei, is written as follows:

$$\hat{H}\psi_i(\vec{r}_1, \vec{r}_2, ..., \vec{r}_N, \vec{R}_1, \vec{R}_2, ..., \vec{R}_M) = E\psi_i(\vec{r}_1, \vec{r}_2, ..., \vec{r}_N, \vec{R}_1, \vec{R}_2, ..., \vec{R}_M) \tag{2.3}$$

$\hat{H}$ is the Hamiltonian operator of the system. The coordinates $\vec{r}_i$ and $\vec{R}_k$ gather the space and spin variables of the electron i and nucleus k, respectively.

The Hamiltonian operator $\hat{H}$ can be decomposed as:

$$H_{total} = T_n + T_e + V_{nn} + V_{ne} + V_{ee} \tag{2.4}$$

Where T_n and T_e correspond to the kinetic energy of the nuclei and the electrons, respectively. V_{nn}, V_{ne} and V_{ee} represent the potential energy of the electrostatic energy between nucleus-nucleus, nucleus-electron and electron-electron, respectively.

Considering the high number of degrees of freedom (3N+3M) and interactions involved in three-dimensional multi-body problems, their exact processing proved to be an impossible task. In view of the impossibility of finding an exact solution to equation (2.4) in the case of N-body poly-electronic systems, it is necessary to use simplifying approaches.

2.2.1.2 Born-Oppenheimer approximation

Born-Oppenheimer approximation supposes that we can decouple the movement of electrons from that of nuclei, starting from the simple observation that electrons are much lighter and that their movement is much faster, and a first approximation takes into account an evolution of electrons in a potential created by fixed atoms [104, 105].

The nuclear wave function can be written as:

$$\psi(\vec{r}, \vec{R}) = \psi_n(\vec{R})\psi_e(\vec{r}, \vec{R}) \tag{2.5}$$

Which means that the Hamiltonian of the equation (2.4) can written as:

$$H_{total} = T_e + V_{ne} + V_{ee} \tag{2.6}$$

That allows the elimination of all Hamiltonian terms involving the nuclei. However, this approximation alone is not sufficient to solve the Schrödinger equation because of the complexity of the electron-electron interactions. This is why it is very often coupled with the Hartree approximation.

2.2.1.3 Hartree-Fock approximation

This approximation is frequently used as it is the basis of almost all ab initio methods. An exact solution of equation (2.3) is only possible in the case of the Hydrogen atom, due to the absence of the multiple Coulombic repulsion terms present in the polyelectronic system. In order to avoid this difficulty, a first approximation, Hartree approximation, considers the multi-electron wave function as the product of single-particle (single-electron) functions, designated by the term "orbital". The wave function of the system is written as:

$$\psi(r_1, r_2, r_3, ..., r_N) = \psi_1(r_1).\psi_2(r_2).\psi_3(r_3).....\psi_N(r_N) \tag{2.7}$$

The wave function ψ is called "Hartree Product". Coulombic repulsion is considered as an average effect and each electron is treated independently but in an effective potential determined by integration over the wave functions of the other electrons. Thus, the Hartree approximation is a mean-field approximation replacing the complicated many-body problem by simple problems in a mean-field potential [106].

However, as the electron is a fermion, the total wave function must be antisymmetric with respect to the exchange of any two particles, which is neglected by Hartree approximation.

To correct that, the Pauli Exclusion Principle is taken into consideration in the Hartree-Fock approximation [107–109]. In this approximation, the multi-electronic wave function is expressed as a Slater determinant constructed from N single-electronic wave functions ψ_i

$$\psi(x_1, x_2, x_3, ..., x_N) = \frac{1}{\sqrt{N!}} \begin{vmatrix} \psi_1(x_1) & \psi_2(x_1) & \dots & \psi_N(x_1) \\ \psi_1(x_2) & \psi_2(x_2) & \dots & \psi_N(x_2) \\ . & . & \dots & . \\ . & . & \dots & . \\ \psi_1(x_N) & \psi_2(x_N) & \dots & \psi_N(x_N)) \end{vmatrix} \tag{2.8}$$

$\frac{1}{\sqrt{N!}}$ is a constant of normalization.

This approximation leads to good results, especially, in molecular physics. So it can only deal with systems with few electrons such as small molecules [110]. It does not take into account the effects of electronic correlations, while the treatment of extended systems such as solids remains difficult to apply. Indeed, the fundamental state corresponds to a global minimum on a set of functions much more extended than the one covered by a Slater determinant. Nevertheless, it is shown that one gradually approaches the fundamental state by writing as a sum of Slater determinant. This would make that calculation very heavy from a numerical point of view. For this reason, Density Functional Theory, which simplifies the calculations, is often used.

2.2.2 Principle of Density Functional Theory

Solving the Schrödinger equation with N-electrons must use approximate methods that can most accurately reproduce the physical quantities containing the most possible of information. However, it is possible to reformulate the problem by using the appropriate theorems and approximations. Density Functional theory would have aroused little curiosity nowadays, except within the framework of the theorem established by Kohn-Sham, which made it useful through approximations on the functional of the ground state, in order to describe real multi-electron systems. The idea of this theory is originated in the work of Thomas and Fermi in 1927 [98, 111]. Although, their approximations are not

sufficiently appropriate for electronic structure calculations.

This approach elucidates how DFT works. In their earlier works, Thomas and Fermi ruled out electron interactions, considering the system as a homogeneous gas and its kinetic energy as a function of the local density. Both authors neglected the exchange-correlation effects that arise between electrons. However, this defect was corrected by Dirac in 1930 [112], who introduced the local exchange approximation. The main goal of DFT is determining the ground-state properties of a given system composed of a fixed number of electrons interacting with the nuclei using only information about the electronic density ρ. So, we must first define what is the electronic density of the system to determine its ground state properties.

2.2.2.1 Hohenberg-Kohn theorems

Unlike the Hartree-Fock approach where the energy of the system is a function of the wave function ψ, Density Functional Theory expresses energy as a function of the electronic density. This method allows great simplification of the solution of the Schrödinger equation. The development of the density functional theory dates back to 1964 and 1965 with the publications of Hohenberg and Kohn [113, 114]. The two theorems are as follows:

Theorem 1: *The total ground state energy of an interacting N-electron system in the presence of an external potential is a unique function of the electronic density ρ:*

$$E = E(\rho) \tag{2.9}$$

This theorem highlights a unique correspondence between the external potential and electronic density. Since the electronic density determines the number of electrons, it also uniquely determines the wave function and thus the electronic properties of the system.

Theorem 2: *The real ground state density is nothing else than the density that minimizes the energy of the system and all other properties are functional of the ground state*

density:

$$E(\rho_0) = min(E(\rho)) \tag{2.10}$$

The main advantage of this theorem is the enormous simplification of the solution of the Schrödinger equation, because of the problem with 3N variables is reduced to a problem of a scalar function in 3-dimensional space.

2.2.2.2 Kohn-Sham equations

Walter Kohn and Lu Sham had the idea in 1965 to consider a fictitious system of N-independent electrons ($V_{ee} = 0$ in equation 2.6) whose, fundamental state is the Slater determinant formed by N-orbitals ψ_i of the electrons and whose the electronic density is the same as that of the real system of interacting electrons. The Schrödinger equation is therefore reformulated in terms of the so-called Kohn-Sham equation, which is in fact a Schrödinger equation with an actual potential in which quasi-particle move [99, 115].

Walter Kohn and Lu Sham have shown that the true density is given by the self-consistent solution of the set of Schrödinger-type single-particle equations, called the Kohn-Sham equations:

$$\{-\frac{1}{2}\nabla^2 + V_{KS}(r)\}\varphi_i(r) = \varepsilon_i\varphi_i(r) \tag{2.11}$$

$$\rho(r) = \sum_{ioccup} |\rho_i(r)|^2 \tag{2.12}$$

$$V_{KS}(r) = V_{ext}(r) + V_{XC}(r) + V_H(r) \tag{2.13}$$

Where:

$V_{ext}(r)$ is the external potential created by the nuclei.

$V_{XC}(r)$ is the potential of the exchange-correlation energy, given as:

$$V_{XC}(r) = \frac{\partial E_{XC}[\rho(r)]}{\partial \rho(r)} \tag{2.14}$$

$V_H(r)$ is the classical Hartree potential given as:

$$V_H(r) = \int \rho(r) \frac{1}{|r - r'|} \cdot dr' \tag{2.15}$$

The total energy of the system is obtained by solving the Kohn-Sham equations with the following equation:

$$E(r) = \sum_{ioccup} \varepsilon_i - \int \frac{\rho(r) \cdot \rho(r')}{|r - r'|} \cdot dr \cdot dr' + E_{XC}(\rho) \cdot \int V_{XC}(r)\rho(r) \cdot dr \tag{2.16}$$

Note that equation (2.11) is similar to the Schrödinger equation but it is only an equivalence, because in particular, the eigenvalues of the Kohn-Sham equation are pure vibrational parameters and therefore do not strongly represent the eigenenergies of the system and the eigenvectors are not the functions of real electronic waves.

2.2.2.3 Exchange-correlation approximation

The only ambiguity in the Kohn-Sham approach is the term of the exchange-correlation. The formal complexity of this term makes the resolution of the Kohn-Sham equations difficult, nevertheless this functional can be subjected to local or near-local approximations of the density. The most basic types of the exchange-correlation approximation are:

Local Density Approximation (LDA): The Local Density Approximation (known as LDA) allows transforming the DFT, an exact N-body theory, into an approximated but very useful and much-used theory. In the Local Density Approximation (LDA), it is assumed that the electronic density can be processed locally as a uniform gas [116]. In other words, this approach consists in carrying out the two following hypotheses:

- The exchange-correlation effects are dominated by the density at the point $\vec{r}$.
- The density $\rho(\vec{r})$ is a slowly varying function with respect to $\vec{r}$.

Thus, the fundamental assumption contained in the formalism of the LDA consists in considering that the contribution of $E_{XC}[\rho(\vec{r})]$ to the total energy of the system can be added cumulatively from each portion of the non-uniform gas as if it were locally uniform.

The LDA approximation assumes that the exchange-correlation term of the total energy of the ground state can be written according to the expression:

$$E_{XC}^{LDA}(\rho) = \int \rho(r) \cdot \varepsilon_{XC}^{hom}(\rho = \rho(r)) \cdot dr \tag{2.17}$$

Where $\varepsilon_{XC}^{hom}(\rho)$ is the exchange-correlation energy for a uniform density of an electron gas.

There is also a version of the LDA that allows electronic spin to be taken into account; it is the Local Spin Density Approximation (LSDA). The exchange-correlation energy E_{XC}^{LDA} become a function of the two spins (Up and down) densities and equation (2.17) becomes:

$$E_{XC}^{LSDA}(\rho\uparrow, \rho\downarrow) = \int \rho(r) \cdot \varepsilon_{XC}^{hom}(\rho\uparrow(r), \rho\downarrow(r)) \cdot dr \tag{2.18}$$

Generalized Gradient Approximation (GGA): A first step to improve the processing of the exchange-correlation energy is to make the $E_{XC}[\rho(\vec{r})]$ function dependent not only on the electronic density $\rho(\vec{r})$ but also on its gradient $[\nabla\rho(\vec{r})]$. Thanks to this modification, the $E_{XC}[\rho(\vec{r})]$ takes into account the non-uniformity of the electron gas [117, 118].

In the GGA formalism, the contribution of the $E_{XC}[\rho(\vec{r})]$ to the total energy of the system can be added cumulatively from each non-uniform portion of the gas as if it were locally non-uniform. This definition of the GGA implies that $E_{XC}[\rho(\vec{r})]$ is of the form:

$$E_{XC}^{GGA}[\rho(\vec{r})] = \int \rho(\vec{r}) \cdot \varepsilon_{XC}[\rho(\vec{r}), |\nabla\rho(\vec{r})|] \cdot d\vec{r} \tag{2.19}$$

In which $\varepsilon_{XC}[\rho(\vec{r}), |\nabla\rho(\vec{r})|]$ represents the exchange-correlation energy dependent on the electronic density and its gradient.

The introduction of these GGA-type functionalities led to the widespread use of DFT within the chemical community in the 1990s. The use of GGA-type functionals significantly increases the accuracy of the calculations compared to the description provided by the LDA, particularly, for the binding energy of the molecules. GGA-type functionals also

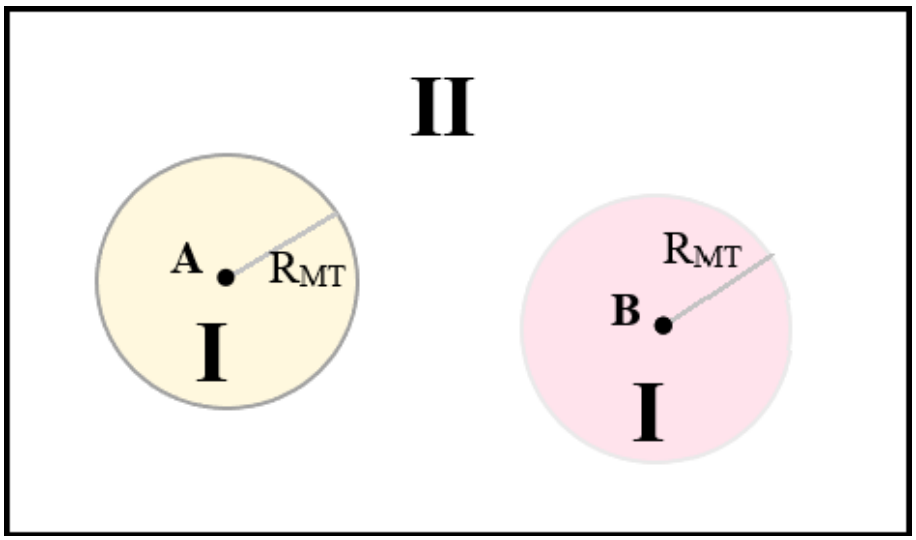

Figure 2.1: Schematic illustration of two atomic spheres A and B with radius R_{MT} (region I) and the interstitial region between the spheres (region II).

provide a better description of the equilibrium volumes, moduli of elasticity and magnetic properties of the compounds compared to the LDA.

2.2.2.4 Solving Kohn-Sham equations

Various methods can be used to solve the Kohn-Sham equations. In this section, we will discuss the most popular methods to solve the Kohn-Sham equations, which are The Full-Potential Linearized Augmented Plane Wave (FP-LAPW) and the Pseudopotential methods.

Full-Potential Linearized Augmented Plane Wave (FP-LAPW):

The Full-Potential Linearized Augmented Plane Wave (FP-LAPW) method developed by Andersen is an improvement of the Augmented Plane Wave (APW) method developed by Slater [119–122]. This method is based on the self-coherent solution of the Kohn-Sham equations in two arbitrarily defined regions of the elementary mesh (see figure 2.1).

- *Region I:* Corresponds to non-overlapping atomic spheres (A and B) of radius R_{MT} (MT=Muffin Tin), where a series of linear combinations of radial and angular functions are used.

- *Region II:* The interstitial region between the spheres, which can be described by plane wave expansions.

The convergence of this base is controlled by cut-off parameter "$R_{MT} \times K_{max}$", which is the product of the radius of the smallest Muffin-Tin sphere and the cut-off energy of the wave plane base.

This method allows the consideration of a realistic potential (FP $\equiv$ Full-Potential), which is not restricted to the spherical component. In contrast to methods using pseudopotentials, the core electrons are included in the calculations. This gives a correct description of the wave functions near the nucleus. This is the most precise method, but it is heavy in computing time.

All works presented in this thesis was done using WIEN2K package developed by Blaha and Schwarz in 1990 and based on the Full-Potential Linearized Augmented PLane Wave method [123, 124].

The method of pseudo-potentials (Plane Wave):

A plane wave base requires a very large number of waves to describe the system. One way to reduce the base is to remove the waves whose kinetic energy is greater in absolute value than a certain energy, which is called "$E_{cut-off}$". This base, although reduced, is however not well adapted because a very large number of plane waves are still needed to correctly describe the strongly bound orbitals of the core electrons.

Elements with few electrons with require few plane waves, while heavy elements or transition metals will require extremely powerful computing resources. However, in most cases, valence electrons are the only one involved in chemical bonds. Core electrons therefore be grouped with nuclei: this approximation is called frozen core approximation, a pseudopotential is then introduced [125].

Phillips and Kleiman set up the first pseudopotentials in 1958. The pseudopotentials currently used are determined from "all electron" calculations, which make the method more accurate [126, 127]. The pseudopotentials associated with high cut-off energies are called "Hard" compared to those called "Soft". Vanderbilt has developed a smaller waveform base than these traditional pseudopotentials, with even lower cut-off energies, called "ultra-soft". This has made it possible to consider systems that are more complex [128].

2.3 Monte Carlo simulation

2.3.1 Introduction

Condensed matter systems are well known to be treated in the context of statistical physics, which was designed primarily to study their properties. This branch of physics is based on a concept that considers that the microscopic quantities of a system closely reflect the observed macroscopic phenomena in that system. The main constraint is the large number of particles in a condensed matter system, which involves many difficult problems related to the structure and type of interactions that occur in the system, making it difficult to find exact solutions to all the questions under consideration. Thus, it is evident that the solutions provided by the analytical methods are only approximate solutions. Therefore, techniques of simulation such as Monte Carlo are now widely used as an important complementary method for developing the understanding of complex physical systems and phenomena.

Monte Carlo simulation is fundamentally defined as a problem-solving technique that admits probabilistic interpretation [129]. It is part of a package of computational algorithms based on repeated random sampling to obtain equilibrium numerical results. This type of simulation has proven its usefulness in the study of systems with many coupled degrees of freedom, such as strongly coupled solids, fluids and disordered materials. It is interesting to note that Monte Carlo simulations are commonly used in other fields than physics such economics, medicine, and others [130–132].

The main goal of Monte Carlo simulation is to track the evolution of a model as a function of time, this time dependence is directly related to the Monte Carlo step, which forms the basis of the process in which the model evaluates to the equilibrium state according to a sequence of random numbers generated during the simulation. Monte Carlo simulation is based on the numerical resolution of systems by using a stochastic process, and is therefore, the most important class of numerical techniques used to solve problems in statistical physics in either equilibrium or out-of-equilibrium cases.

The principle of Monte Carlo simulation is based on some basic concepts, which are

described in the next section.

2.3.2 Basic concepts of Monte Carlo simulation

Monte Carlo simulation allows the estimation of the average of a physical quantity $\langle Q \rangle$, which can be given in the canonical system as:

$$\langle Q \rangle = \frac{\sum_i Q_i \exp(-\beta E_i)}{\sum_i \exp(-\beta E_i)} \tag{2.20}$$

Where $\exp(-\beta E_i)$ is the Boltzmann factor, that is, the probability density of the canonical ensemble.

$\beta = \frac{1}{K_B T}$ with K_B is the Boltzmann constant, T is the temperature of the system and E_i is the potential energy.

The principle of Monte Carlo simulation is based on the following basic ideas [133]:

The choice of the sample:

The average values of the quantities recovered by Monte Carlo simulation are calculated based on the states that the system assumes over time. The system does not necessarily assume all possible states during measurements. Real systems behave as a kind of Monte Carlo simulation during their evolution to define their properties. The sample states are not equiprobable, but are distributed according to the Boltzmann distribution. This distribution is mainly used to improve the mean value estimation. Therefore, the concept of a large sample is to create an appropriate Markov chain in which the configurations are chosen according to their weight, according to the Boltzmann probability.

The Markov chain:

Typically, Monte Carlo simulation uses the Markov chain to generate randomly the configurations of the studied system. The transition to a configuration denoted "b" depends only on the previous configuration denoted "a", but not an all configurations in the space of the state. This means that the transition, which can follow the probability $W(a \rightarrow b)$, in a Markov chain is almost local in time.

In a Monte Carlo simulation, we use a Markov process several times to generate a

Markov chain. Starting with the configuration "a" to a new configuration "b", then we feed this configuration into a process to generate another configuration "c", and so on. The Markov process is specially chosen because, when it runs long enough from any state in the system, it will eventually produce a succession of states that appear with probabilities given by the Boltzmann distribution. For that, we put two other conditions on our Markov process; the ergodicity and the detailed balance.

The ergodicity:

The ergodicity condition is that the system can assume any possible state from a given one after a sufficiently long time during the Markov process. The ergodicity condition is not satisfied if all transition probabilities of a given state are zero.

The detailed balance:

The detailed balance condition ensures that the future balance is only a Boltzmann distribution and not another distribution. If the system is in equilibrium, the probabilities of transition from one state to the same state are equal, which can be described by the following transition:

$$\sum_a P_a \times W(a \to b) = \sum_b P_b \times W(b \to a) \tag{2.21}$$

As W(a $\to$ b) = 1, equation (2.21) will be written as:

$$\sum_a P_a \times W(a \to b) = P_a = \sum_b P_b \times W(b \to a) \tag{2.22}$$

For any set of transition probabilities that satisfies equation (2.22), the distribution will be the equilibrium distribution implied by the dynamics of Markov processes. This equation does not guarantee the distribution of the state of the system. To demonstrate this, let us consider that the transition probabilities W(a $\to$ b) are the elements of the Markov matrix:

$$q_b(t+1) = \sum_a W(b \to a) \times q_b(t) \tag{2.23}$$

In a matrix form:

$$Q(t+1) = M \times Q(t) \tag{2.24}$$

Equation (2.22), therefore, does not guarantee the equilibrium defined by the distribution. To overcome this difficulty, the detailed balance condition is given by:

$$P_a \times W(a \to b) = P_b \times W(b \to a) \tag{2.25}$$

As it is well known, real systems satisfy the condition of detailed balance. For a balanced Boltzmann distribution, an additional condition is derived from equation (2.25). We can write:

$$\frac{P_b}{P_a} = \frac{W(a \to b)}{W(b \to a)} = \exp(-\beta(E_b - E_a)) \tag{2.26}$$

The main objective is to create a program that builds the Markov chain according to the transition probabilities.

The Acceptance:

A given algorithm does not necessarily define the exact set of transition probabilities. Therefore, the acceptance probability allows finding the right transition probabilities of any Markov process. In this case, the condition W(a $\to$ b) $\neq$ 0 is allowed and always meets the detailed balance. Thus, the transition probability can be given by:

$$W(a \to b) = g(a \to b) \times A(a \to b) \tag{2.27}$$

Where:

- g(a $\to$ b) is the probability of selection. It represents the probability to obtain new state "b" from the old state "a" by the algorithm.
- A(a $\to$ b) is the acceptance probability, which corresponds to the probability of accepting the transition from the old state "a" to the new state "b".

The value of the acceptance probability (or acceptance), is random between 0 and 1. Equation (2.26) becomes:

$$\frac{P_b}{P_a} = \frac{W(a \to b)}{W(b \to a)} = \frac{g(a \to b) \times A(a \to b)}{g(b \to a) \times A(b \to a)} \tag{2.28}$$

In order to avoid that the algorithm is slow, we generally admit acceptance close to

one. The best algorithm is therefore the one that adds the selection probability g(a → b) and takes A(a → b) ≃ 0.

2.3.3 Implementation of the Metropolis Algorithm

The Metropolis algorithm is known for its ability to be applied in wide range of areas [134]. The application of this algorithm on the Ising model, consists in making a single flip attempt at each Monte Carlo step [135, 136]. In this case, all selection probabilities are equals and are given by:

$$g(a \to b) = \frac{1}{N} \tag{2.29}$$

Where N is the number of spins in the system.

The detailed balance equation (2.28) can therefore be written as follows:

$$\frac{P_b}{P_a} = \frac{W(a \to b)}{W(b \to a)} = \frac{g(a \to b) \times A(a \to b)}{g(b \to a) \times A(b \to a)} = \exp(-\beta(E_b - E_a)) \tag{2.30}$$

The Metropolis algorithm is closely related to the choice of the acceptance A(a → b) and can be defined as follows:

$$A(a \to b) = \begin{cases} \exp(-\beta(E_b - E_a)) & if(E_b - E_a > 0) \\ 1 & elsewhere \end{cases} \tag{2.31}$$

The transition probability W(a → b) assumes the same form as acceptance, with this choice of transition probabilities the system tends towards a stable configuration, in which the system looks for the equilibrium state.

In summary, the implementation of Metropolis algorithm can be presented in the following steps:

- From an initial configuration “a” of energy ”E_a”, a new configuration “b” of energy ”E_b” is selected randomly.

- Each new configuration is tested to see if it should be accepted or rejected by calculating the variation of energy $\triangle E = E_b - E_a$

** If $\triangle E < 0$, the new configuration “b” is accepted.

** If $\triangle E > 0$, we generate a number randomly, r, between 0 and 1. If $r < \exp(-\beta \triangle E)$, the new configuration "b" is accepted. Otherwise, the new configuration "b" is rejected. - The process is repeated until a new configuration is obtained.

2.4 Synthesis methods

2.4.1 Introduction

The suitability of a magnetic material for specific applications is mainly determined by the requirements of these applications. For example, a permanent magnet material should have high coercivity and high saturation magnetization. The scenarios for tailoring magnetic materials for specific applications included the adoption of different synthesis methods to control the structural, microstructural and the magnetic properties of the produced ceramics. Some synthesis methods used in our work are addressed briefly in this section.

2.4.2 Solid-State Reaction

Solid State reaction, often called "the conventional ceramic method", is a simple method, which involves the mixing and sintering of appropriate molar ratios of metal oxides and/or carbonates precursors [137, 138]. Ball milling of the starting powders provides smaller particles size and better homogeneity of the resulting ferrite precursor powder, allowing for better crystallization of the ferrite even at low sintering temperatures [139, 140].

After making the choice of the appropriate molar ratios of the starting precursors, which can be, generally, metal oxides and/or carbonates. The solid-state reaction process can be presented in the following four steps:

Mixing and Milling

This is one of the essential phases in the manufacturing process of a ferrite material. During this operation, a uniform distribution of the starting precursors is obtained.

Calcination

Materials are subjected to a thermal cycle, possibly in a controlled atmosphere, during which, they will react and form the desired phase by solid-phase diffusion phenomena. During this reaction, Carbon dioxide and possibly some water vapor are released.

Re-grinding

After a heat treatment, the powder is re-grinded to reduce grain size, homogenize it and increase its reactivity. The powder is then subjected to another heat treatment to achieve the crystallinity.

Sintering

This step is of primary importance because it allows the densification of the material as well as the adjustment of the chemical composition. It is necessary to bring it to a higher temperature compared to the calcination step.

2.4.3 Coprecipitation method

Coprecipitation method allows precursor products to be obtained by simultaneous precipitation of two cations M and M', where M being and alkali or an alkaline earth and M' is a transition metal [141–144].

Generally, after mixing the two solutions containing the metal cations, the pH measurement is necessary to be able to follow the evolution of the precipitation. After dissolution of the appropriate masses of metal oxides, the solutions are mixed progressively, and then diluted. Heat activates Coprecipitation and the pH of the reaction environment is of a great importance for the majority of Coprecipitation reactions since it determines the nature and stoichiometry of the precipitate (figure 2.2). This dependence of the reaction mechanism on pH makes it very difficult to obtain a given stoichiometry and it is a major disadvantage during the synthesis process.

The Coprecipitation method has shown some limitations in its use. The major constraint of the method is the conservation of the M'/M ratio of the stoichiometry.

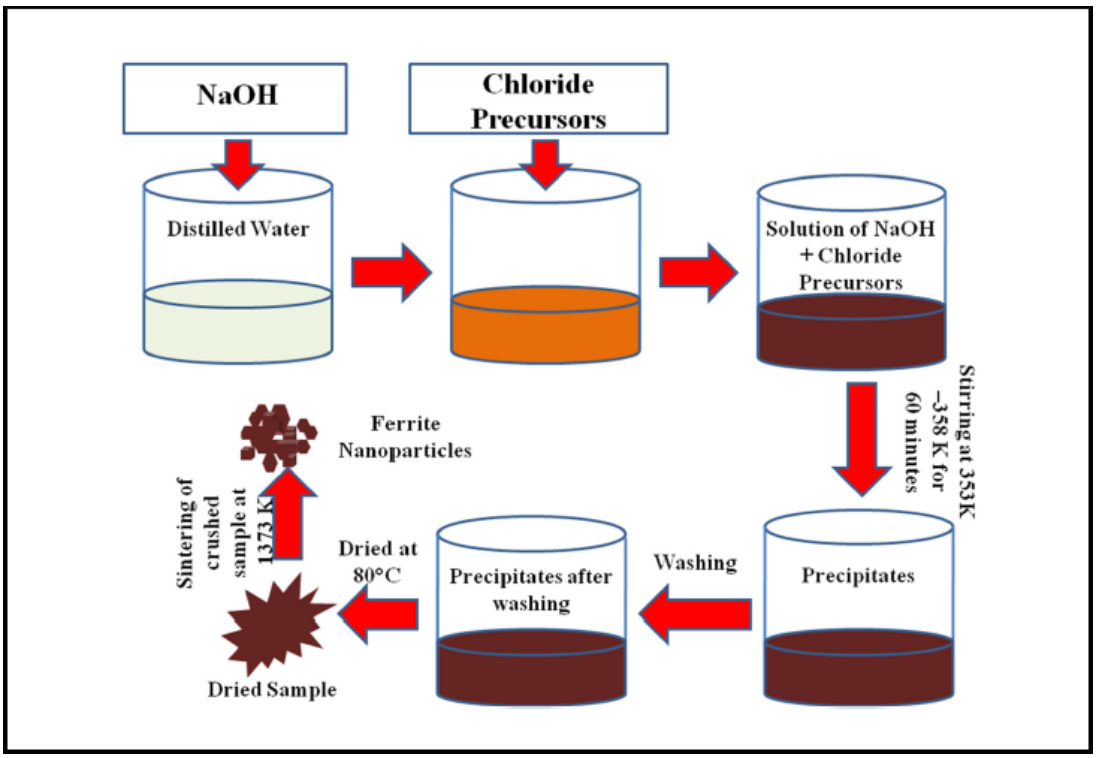

Figure 2.2: Schematic illustration of the Coprecipitation method; example of ferrite nanoparticles [145]

2.4.4 Sol-gel Auto-combustion method

The sol-gel auto-combustion technique has emerged as an attractive method for the production of high purity, homogeneous, and crystalline oxide powders using inexpensive raw materials [81, 146–148].

This technique proceeds via a combination of chemical sol-gel and subsequent combustion processes. An aqueous solution containing the desired metal salts and organic fuels from a gel through a sol-gel process. Thereafter, the gel is ignited to combust, yielding a voluminous and fluffy product with large surface area. In this process, citric acid is used as a complexant to form a homogeneous precursor xerogel (figure 2.3).

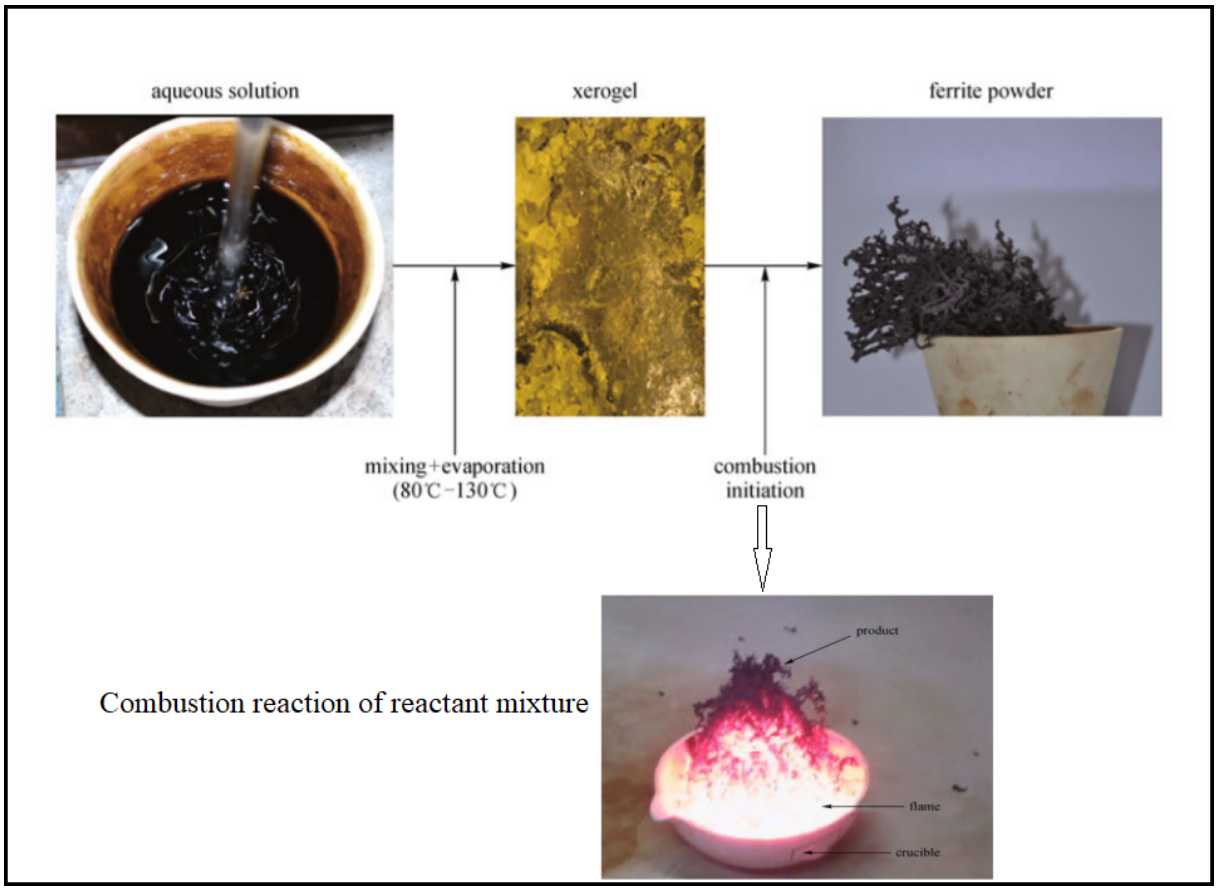

Figure 2.3: Schematic illustration of the sol-gel auto-combustion method; example of ferrite powder [149]

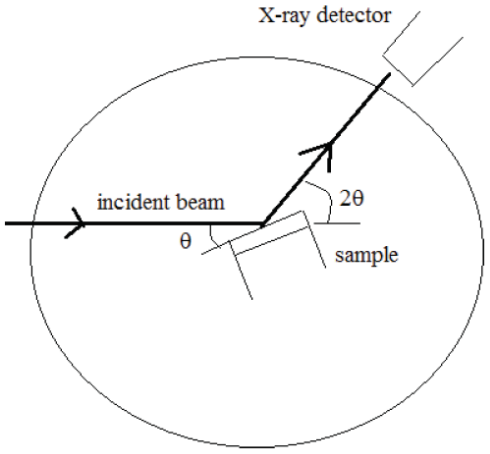

Figure 2.4: Schematic diagram of diffractometer [154]

2.5 Characterization techniques

2.5.1 X-ray diffraction (XRD)

X-ray diffractometry is an analytical technique based on the interaction of the X rays with the electron cloud of atoms in a material. It makes it possible to study crystallized materials and to obtain informations on the organization of matter, such as the crystal structure and the possible of existing parasitic phases. It also allows the measurement of lattice parameters, stresses, micro-stresses and the crystallite size [150–152].

The first person who used x-rays as a tool for crystallography was William Bragg, who was conducting his studies about x-rays that they were electromagnetic waves. He found that the wavelength of these rays is comparable to the atomic dimensions, and he proved that this wavelength is the ley to look inside of the material and determine their crystalline structure, which is not possible with the visible light [153].

As it is illustrated in figure 2.4, when X-rays arrive at the materials, they cause a displacement of the electronic cloud with respect to the nucleus of the atom. These induced oscillations cause a re-emission of electromagnetic waves in all directions of space, keeping the same energy and wavelength, this phenomenon is called “Rayleigh scattering”.

From Bragg’s law, a diffraction peak is obtained only when the distance travelled by the rays after reflection from successive crystal planes differs by an integral multiple of

Figure 2.5: Bruker D8 X-ray diffractometer.

wavelengths, in accordance with Bragg's equation [153]:

$$\lambda = 2d_{hkl} \sin\theta \tag{2.32}$$

d_{hkl} is the distance between two crystallographic planes, called "interreticular distance". θ is the incident angle. λ is the x-ray wavelength.

In this work, the x-ray diffraction patterns were collected using an x-ray diffractometer in the 2Tetha range from 5 to 100 using Bruker D8 60-powder diffractometer with Cu-K_α ($\lambda_{Cu} = 1.5407\ \mathring{A}$) with Bragg-Brentano configuration at room temperature (figure 2.5).

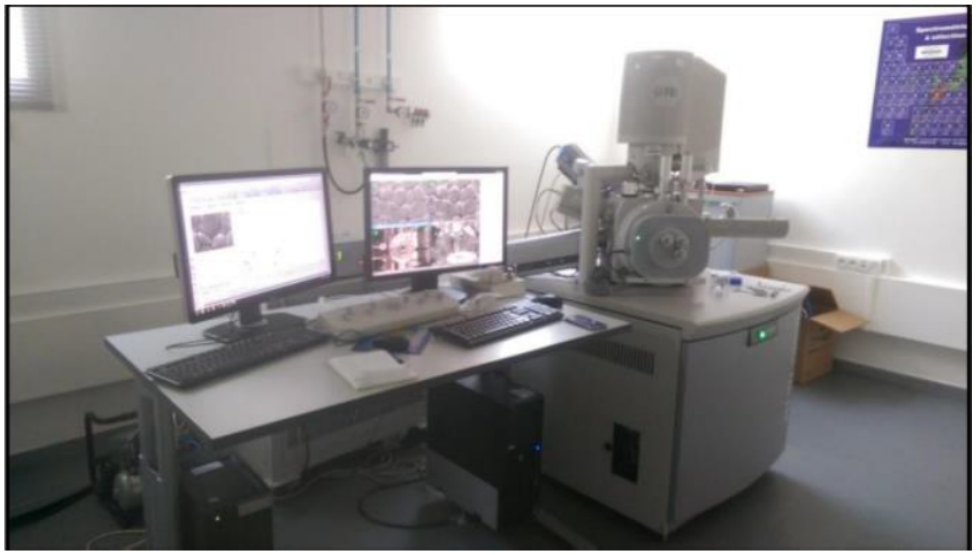

Figure 2.6: FEI Scanning Electron Microscope, Quanta FEG 450.

2.5.2 Scanning Electron Microscopy (SEM)

The scanning electron microscopy has been used to observe the surface and morphology of materials, capable of producing high-resolution images of the surface of samples down to a few nanometers. The principle of this technique consists of a finely focused electron beam deflected through electromagnetic lenses that scans the surface of a sample. The electron-matter interaction gives rise to the following emissions at any point on the scanned surface: secondary electrons (SE), backscattered electrons (BSE), light photons and X-rays. The exploitation of these emissions allows the observation of the morphology, topography and microstructure of the analyzed material, in addition to the qualitative and quantitative detection of the atomic elements present in the structure [155, 156].

The SEM used in our work is an "FEI, Quanta FEG 450" electron microscope with an EDX detector. It is equipped with a column-integrated (In-lens) secondary electron (SE) detector for a clear topographic imaging and a backscattered electron (BSE) detector for compositional contract imaging, which allow simultaneous real-time imaging and mixing both signals (figure 2.6).

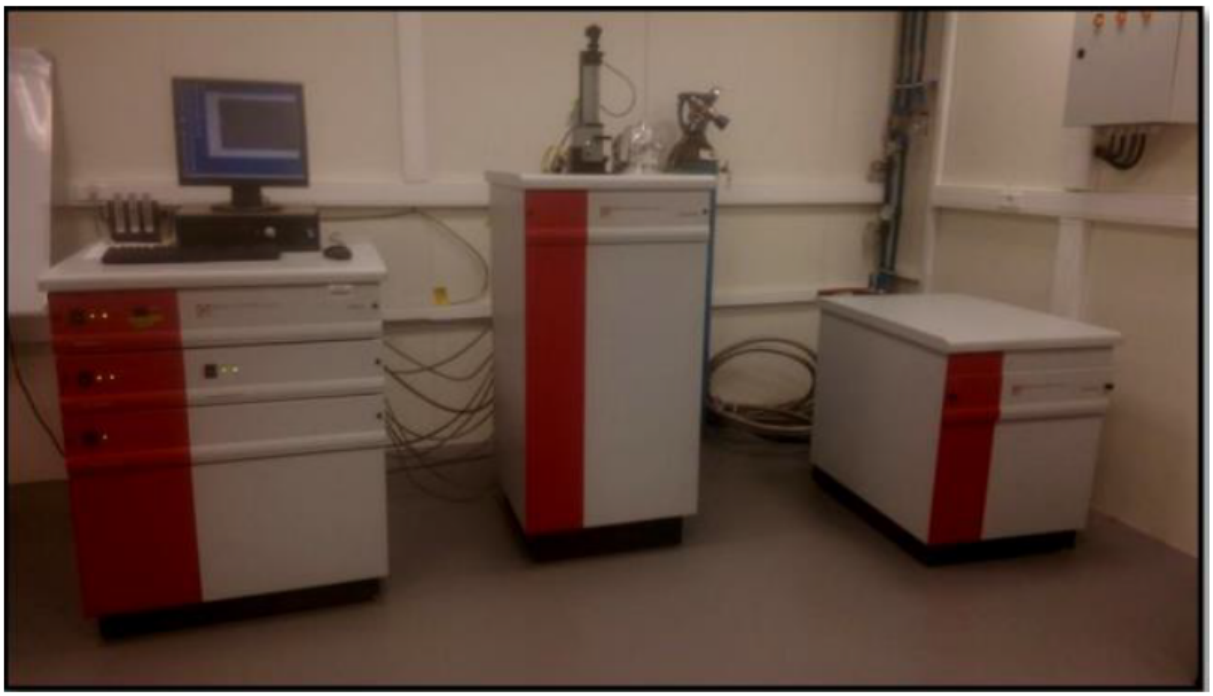

Figure 2.7: MPMS-XL7 magnetometer.

2.5.3 SQUID Magnetometer

As part of this thesis, we were interested in determining the magnetic properties of the prepared samples recommended for the permanent magnet applications, in particular, the hysteresis loop measurements at room temperature. For this reason, we used the MPMS-XL7 magnetometer with SQUID (Superconducting Quantum Interference Device) from the company "Quantum Design" (figure 2.7).

The main components of this magnetometer are:

- A superconducting solenoid to generate an intense magnetic field.
- A superconducting magnetic induction detection coil is located inside and in the center of the magnet.
- A SQUID connected to the sensing coil (for magnetization measurement).
- A temperature control system.

The sample is moved inside the sensing coil by a vertical back and forth movement. The flow variations generated by the sample induce a current in the sensing coil which is transmitted to the SQUID. This equipment can be considered as a current-to-voltage converter and the voltage variations are then directly proportional to the magnetic flux.

2.6 Conclusion

To conclude, the different theoretical and experimental methods to determine the physical properties of spinel ferrites and hexaferrites for their application as permanent magnets were described in this chapter. In particular, ab initio methods, Monte Carlo simulation with the different approximations that we used in this thesis. In addition to all the experimental techniques that allow the elaboration of these materials and the main characteristic measurements.

Part II

Contribution and results

Chapter 3

Tuning the magnetic properties of Cobalt spinel ferrites

3.1 Introduction

Cobalt ferrite is considered as one of the most studied materials in the spinel ferrite family because of its interesting properties such as: chemical and mechanical stability, easy synthesis route with cost, high coercivity, significant saturation magnetization and high cubic magnetocrystalline anisotropy, which make it a promising candidate in permanent magnet applications [81, 157–159]. Nowadays, several studies have been published on the structural, electronic and magnetic properties of $CoFe_2O_4$ using both experimental techniques of preparation such as co-precipitation, thermal decomposition, sol–gel, solid-state reaction, and others as well as theoretical tools such as Density Functional Theory and Monte Carlo simulation [160–168].

In this chapter, We will present a combined study based on the synthesis, characterization, Density Functional Theory and Monte Carlo simulation. The first part of the chapter will be consecrated to bulk $CoFe_2O_4$ material. For that, we used the solid state reaction to prepare the sample and then some characterization techniques, in particular, the X-ray diffraction (XRD), the scanning electron microscopy (SEM) and the SQUID magnetometer for the structural, microstructural and magnetic characterization, respec-

tively. Density Functional Theory is used to study and discuss the electronic structure, the exchange coupling interactions and the magnetocrystalline anisotropy. To calculate the magnetic hysteresis loop the maximum energy product of bulk $CoFe_2O_4$, Monte Carlo simulation is used with periodic boundary conditions and a large enough size of the system.

In the last decade, a great interest has been given to nano-sized magnetic materials because of the high demand for miniaturized technological devices. Understanding the magnetic properties at the nanoscale is a crucial issue to enhance the performance of permanent magnet material. As it is well known, the magnetic properties of nanoparticles depend strongly on their shape and size, surface effects, magnetic anisotropy, etc. As the particle size decreases, a reduction of the saturation magnetization (Ms) is observed due to the existence of a disordered spin configuration at the surface compared to the core configuration. The surface effects become predominant as the size of the particles decreases which makes the surface and the finite-size effects commonly correlated [169].

We will present in the second part of this chapter a Monte Carlo simulation of cubic shaped single particles of $CoFe_2O_4$ that aims to study the size effect on the magnetic properties and take out the theoretical limits of the maximum energy product of cobalt ferrite.

3.2 Study of the magnetic properties of bulk $CoFe_2O_4$

3.2.1 Sample preparation: Solid-State Reaction

The cobalt ferrite particles were prepared according to the solid-state reaction. Iron oxide (Fe_2O_3, 95 % from Sigma Aldrich) and Cobalt oxide (CoO, 99 % from Sigma Aldrich) were used as starting precursors. Stoichiometric amounts of metal oxides were mixed in an agate mortar for 1 hour followed by a preheating at 800 °C for 6 hours. The obtained powder was ground for half-hour and calcined at 1200 °C for 6 hours under air.

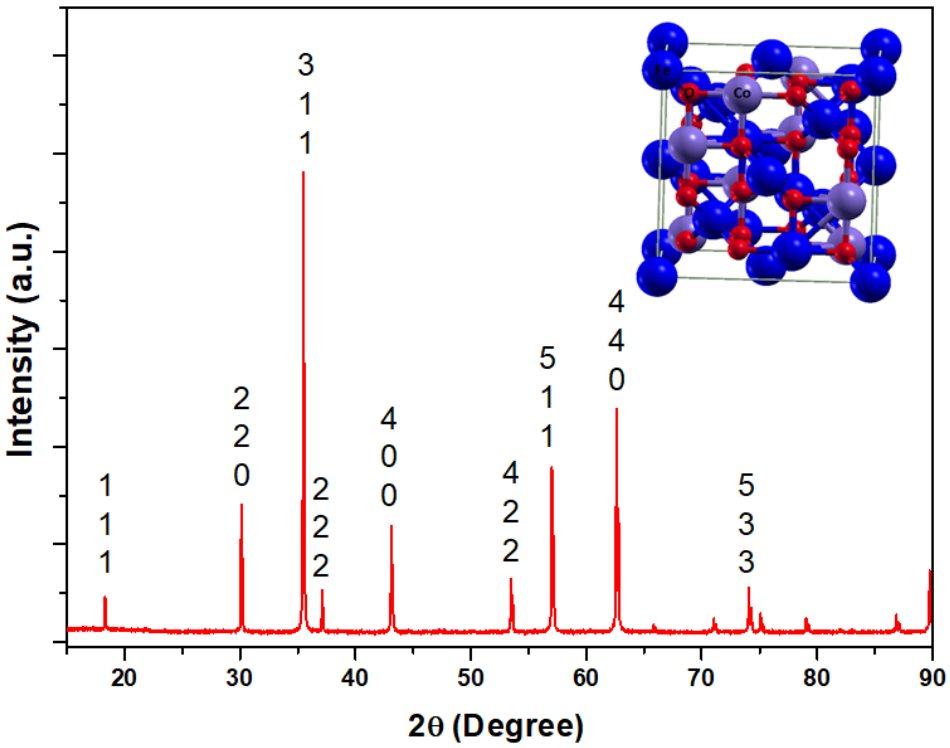

Figure 3.1: X-ray diffraction pattern and the crystalline structure of $CoFe_2O_4$ [170]

3.2.2 Structural and microstructural analysis

The obtained sample was subjected to some techniques to characterize the structural and microstructural properties. The structural phase is verified using the X-ray diffractometer with Cu-K_α radiation ($\lambda = 1.54\ \mathring{A}$). Scanning Electron Microscope (FEI Quanta 450 FEG) is used to perform the microstructural properties.

3.2.2.1 X-Ray Diffraction (XRD)

Figure 3.1 shows the x-ray diffraction pattern of the prepared cobalt ferrite. All detectable peaks are in good correspondence to the face-centered cubic system of the spinel ferrite with space group Fd-3m (JPCDS N° 00-022-1086). No impurities or secondary phases were detected, which proves the successful synthesis of the cobalt spine ferrite using the Solid-state reaction.

By considering the most intense peak (3 1 1), lattice parameters and cell volume were calculated using the Bragg's Low (a = 8.3654 $\mathring{A}$ and V = 589.6355 $\mathring{A}^3$).

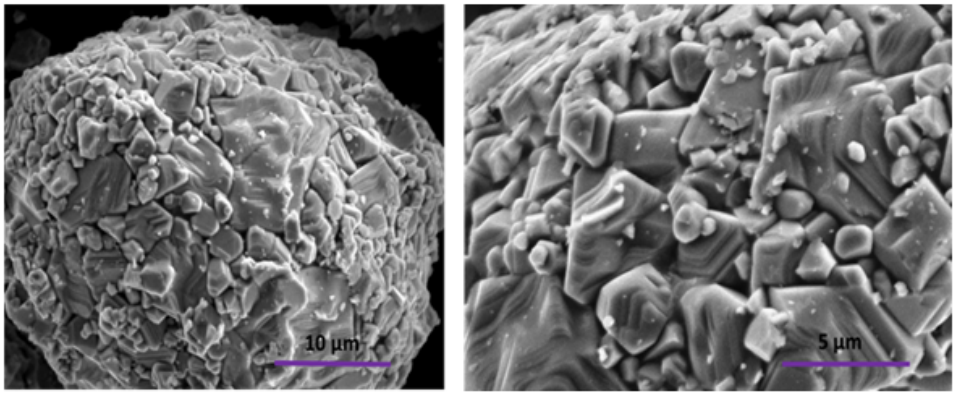

Figure 3.2: SEM images of bulk $CoFe_2O_4$ [170]

The crystallite size was calculated using the Debye-Scherrer formula:

$$D_{X-ray} = \frac{0.9\lambda}{\beta \cos(\theta)} \tag{3.1}$$

Where λ is the wavelength (Cu-K_α), β is the full width to half maximum (FWHM) of the most intense peak (3 1 1) and θ is the Bragg angle of diffraction for the same peak. It was found that the prepared sample has an average crystallite size of about 2.42 μm.

3.2.2.2 Scanning Electron Microscopy (SEM)

To better illustrate the morphology and the size of the obtained particles, Scanning Electron Microscopy (SEM) was used. As it is shown in figure 3.2, $CoFe_2O_4$ sintered at 1200 °C has an inhomogeneous distribution of grains in size and morphology. From the SEM images, it can be seen that the synthesized particles are mostly between 2 μm and 5 μm. Some agglomerated particles with a size of about 40 μm were also observed in the sample. This agglomeration can be explained by the high temperature and large time of the calcination leading to the connection of particles [164].

3.2.3 Exchange coupling interactions and magnetocrystalline anisotropy: Density Functional Theory

Before calculating the exchange interactions and the magnetocrystalline anisotropy of a given magnetic material, some preliminary calculations should be done. For this reason,

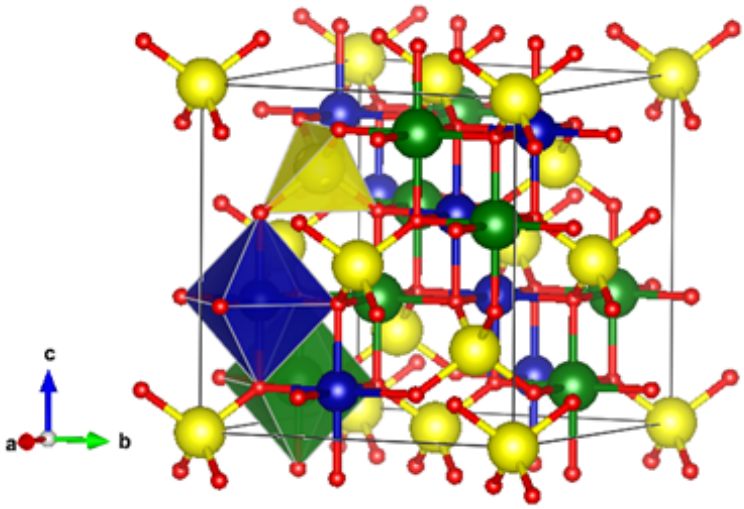

Figure 3.3: The unit cell of $CoFe_2O_4$ spinel ferrite. Colored spheres surrounded by Oxygen atoms forming tetrahedral sites (Yellow spheres represent Fe^{3+}) and octahedral sites (represented by Green and blue spheres for Fe^{3+} and Co^{2+} ions respectively) [92]

we used density functional theory to calculate and present, in this part, the crystalline structure of the $CoFe_2O_4$ compound, its electronic properties that allow us to describe the magnetic structure within a magnetic Hamiltonian. Then, the results of the exchange couplings and the magnetocrystalline anisotropy will be given and discussed.

3.2.3.1 Crystalline Structure of $CoFe_2O_4$

Conforming to the obtained results experimentally and with the available results in the literature, $CoFe_2O_4$ crystallizes in the face-centered cubic system with an experimental lattice parameter of about 8.3654 $\mathring{A}$ [170–172]. The optimized cationic distribution of the cationic ions is the inverse spinel structure in which the tetrahedral sites are mostly occupied by Fe^{3+} with the 8a special Wyckoff position (0, 0, 0), while the octahedral sites are equally shared between Fe^{3+} and Co^{2+} with the 16d special Wyckoff position (0.625, 0.625, 0.625). The Oxygen ions O^{2-} occupied the 32e special Wyckoff position (0.39, 0.39, 0.39) as it is represented in figure 3.3 [92].

Partial Magnetic Moment				Total Magnetic Moment
Fe_(Tetra)	Co_(Octa)	Fe_(Octa)	O	
-3.2336	2.4724	3.5115	0.0739	$2.82 \approx 3$

Table 3.1: Total and partial magnetic moments in μ_B of $CoFe_2O_4$ material.

3.2.3.2 Electronic properties of $CoFe_2O_4$: Density of States

We used density functional theory within the full-potential linearized augmented plane wave (FP-LAPW) as implemented in the Wien2k package [173, 174]. The Generalized Gradient Approximation proposed by Perdew, Burke, and Ernzerhof (GGA-PBE) was used to evaluate the exchange-correlation energy [175]. The self-consistency was obtained for a number of 500 k-points in full Brillouin zone (Bz) which is equivalent to 172 k-points of $7 \times 7 \times 7$ meshes in the irreducible symmetry wedge of the first Brillouin zone. The iteration process is repeated until the calculated total energy of the crystal converges to less than 10^{-5} Ry.

The total and partial densities of states of the Co-spinel ferrite are presented in Figure 3.4. Half-metallic behavior is shown with a polarization of 100 % at the Fermi level. The partial densities of states (PDOS) show a negligible contribution of the Fe^{3+} ions in the octahedral sites removed by the antiparallel spins of Fe^{3+} ions in the tetrahedral sites. Furthermore, the major contribution to the magnetic moment comes from the Co^{2+} cations in the octahedral sites leading to a total magnetic moment of about 3 μ_B per unit formula as it is listed in table 3.1.

3.2.3.3 Magnetic Hamiltonian

O. Iglesias and A. Labarta have postulated a simple but successful Ising model to study the finite size and surface effects on the magnetic properties of maghemite single spherical particles [176]. As the maghemite has the same spinel structure of $CoFe_2O_4$, we used the Ising model to describe the magnetic structure of $CoFe_2O_4$. To avoid any ambiguity in our simulation, the octahedral Fe^{3+} and Co^{2+} ions will be referred as B_1 and B_2, respectively. Our Hamiltonian takes into interest the magnetic exchange couplings

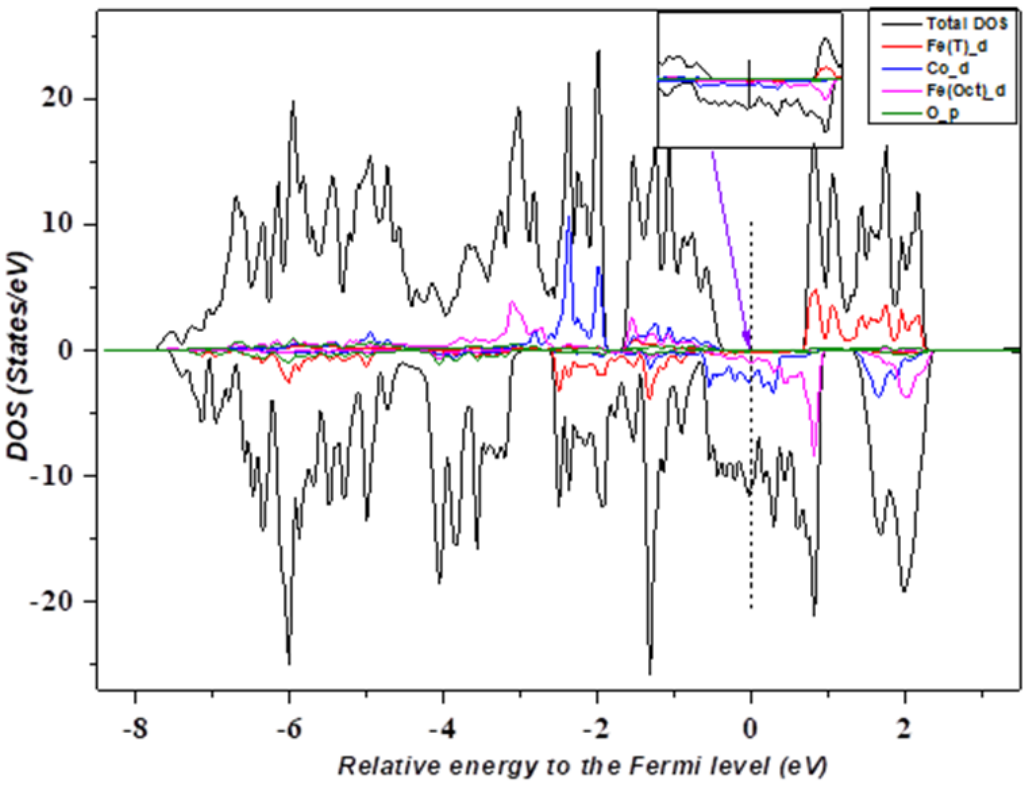

Figure 3.4: Total and partial densities of states of $CoFe_2O_4$ spinel ferrite material.

between nearest neighbors and an external magnetic field as follow:

$$H = -\sum_{\alpha,\beta=A,B_1,B_2}\sum_{i=1}^{N_\alpha}\sum_{j=1}^{N_{\alpha\beta}} J_{\alpha\beta}S_i^\alpha S_{i+j}^\beta - \sum_{\alpha,\beta=A,B_1,B_2}\sum_{i=1}^{N_\alpha} K_{i\alpha}(S_i^\alpha)^2 - h\sum_{\alpha,\beta=A,B_1,B_2}\sum_{i=1}^{N_\alpha}(S_i^\alpha) \tag{3.2}$$

Where $S^{\alpha=A} = S^{\alpha=B_1} = \pm\frac{5}{2}, \pm\frac{3}{2}, \pm\frac{1}{2}$ and $S^{\alpha=B_2} = \pm\frac{3}{2}, \pm\frac{1}{2}$ are the spin variables of the Fe_{3+} ions in tetrahedral sites, Fe_{3+} ions in octahedral sites and the Co_{2+} ions in octahedral sites, respectively.

$J_{\alpha\beta}$ represent the exchange interactions of the spins with nearest neighbors, K_α is the magnetocrystalline anisotropy and h is the applied magnetic field.

3.2.3.4 Exchange coupling interactions

The exchange couplings in spinel ferrites occur indirectly through oxygen ions (super-exchange interaction) with the predominance of the inter-sublattice interactions [177, 178]. To calculate the super-exchange interactions between nearest neighbors in $CoFe_2O_4$ compound, we used density functional theory within the full-potential linearized augmented

	A-A	A-B_1	A-B_2	B_1-B_1	B_1-B_2	B_2-B_2	Total energy (Ry)
FM	$\uparrow-\uparrow$	$\uparrow-\uparrow$	$\uparrow-\uparrow$	$\uparrow-\uparrow$	$\uparrow-\uparrow$	$\uparrow-\uparrow$	-16021.23983
AFM1	$\uparrow-\uparrow$	$\uparrow-\downarrow$	$\uparrow-\downarrow$	$\uparrow-\uparrow$	$\uparrow-\uparrow$	$\uparrow-\uparrow$	-16021.39135
AFM2	$\uparrow-\uparrow$	$\uparrow-\uparrow$	$\uparrow-\downarrow$	$\uparrow-\uparrow$	$\uparrow-\downarrow$	$\uparrow-\uparrow$	-16021.30891
AFM3	$\uparrow-\downarrow$	$\uparrow-\downarrow$	$\uparrow-\downarrow$	$\uparrow-\downarrow$	$\uparrow-\downarrow$	$\uparrow-\downarrow$	-16021.34982
AFM4	$\uparrow-\uparrow$	$\uparrow-\downarrow$	$\uparrow-\uparrow$	$\uparrow-\uparrow$	$\uparrow-\downarrow$	$\uparrow-\uparrow$	-16021.25302
AFM5	$\uparrow-\uparrow$	$\uparrow-\downarrow$	$\uparrow-\uparrow$	$\uparrow-\uparrow$	$\uparrow-\downarrow$	$\uparrow-\uparrow$	-16021.29510

Table 3.2: Magnetic configurations and total energy of each magnetic configuration.

$J^{A-A}(K)$	$J^{A-B_1}(K)$	$J^{A-B_2}(K)$	$J^{B_1-B_1}(K)$	$J^{B_1-B_2}(K)$	$J^{B_2-B_2}(K)$
0.5	-47.7	-26.3	5.9	11.3	2.8

Table 3.3: The Calculated exchange interactions between first nearest neighbors.

plane wave (FP-LAPW) as implemented in the Wien2k package [173, 174]. The exchange-correlation energy was evaluated by the Generalized Gradient Approximation proposed by Perdew, Burke, and Ernzerhof (GGA-PBE) [175]. The self-consistency was obtained for a number of k-points of 500 in full Brillouin zone (Bz) which is equivalent to 172 k-points of 7 × 7 × 7 meshes in the irreducible symmetry wedge of the first Brillouin zone. The iteration process is repeated until the calculated total energy of the crystal converges to less than 10^{-5} Ry.

According to the three-sublattice model, different magnetic configurations have been considered. However, only six magnetic configurations that show lower energies (FM, AFM1, AFM2, AFM3, AFM4, AFM5) were taken into consideration to calculate the exchange interactions in $CoFe_2O_4$ as it is presented in table 3.2.

Table 3.3 presents the calculated exchange couplings between first nearest neighbors. We found a strong inter-sublattice interaction J^{A-B_1} and J^{A-B_2}, while the intra-sublattice interaction J^{A-A} between Fe^{3+} ions in the tetrahedral sites was the weaker interaction in $CoFe_2O_4$ material. Thus, weak ferromagnetic exchange interactions were found for ions in octahedral sites.

Our three-sublattice model shows a good agreement with the super-exchange and Néel theory of ferrimagnetic material that predict successfully the qualitative results of the magnetic properties of ferrites [178, 179].

3.2.3.5 Magnetocrystalline anisotropy

The magnetocrystalline anisotropy energy (MAE) is a very important parameter to generate large coercivity in magnetic materials. It presents the required energy to reorient the magnetization from a preferred direction to another spatial direction. Herein, spin-orbit coupling (SOC) was included in the ab initio calculations of the total energies for spin oriented along easy-axis magnetization (E_a) and hard-axis (H_a) magnetization within a second variational approach. The magnetocrystalline anisotropy energy was calculated as the subtraction of the total energies MAE $\approx$ E(E_a) - E(H_a). It was found that this material possesses a high magnetocrystalline anisotropy of about 2.03 MJ/m^3. Our obtained value is in good agreement with the experimental results of Kumar et al., [180].

3.2.4 Monte Carlo Simulation and Experimental measurements of the magnetic properties of bulk $CoFe_2O_4$

The magnetic properties of bulk $CoFe_2O_4$ were calculated using Monte Carlo simulation based on the Metropolis Algorithm with periodic boundary conditions to neglect the surface effect and guarantee the same number of neighbors of each element. In all our calculations, a large size of the system was used with N = 32 for 4 × 4 × 4 lattice units. Higher Monte Carlo steps up to 2×10^6 were chosen, where the equilibrium was reached after 2×10^5 steps.

In this work, we used the following equations to calculate the magnetization and the susceptibility [181]:

$$m = \frac{1}{N}(\sum_{i}^{N_1} S_i^a + \sum_{i}^{N_2} S_i^b + \sum_{i}^{N_3} \sigma_i) \tag{3.3}$$

$$\chi = \frac{N}{K_B T}(< m^2 > - < m >^2) \tag{3.4}$$

Where N_1, N_2 and N_3 are the total number of spin of Fe in tetrahedral sites, Fe in octahedral sites and Co in octahedral sites. $N = N_1 + N_2 + N_3$ presents the total number of spin in the system.

Figure 3.5 presents the magnetization and susceptibility as function of temperature.

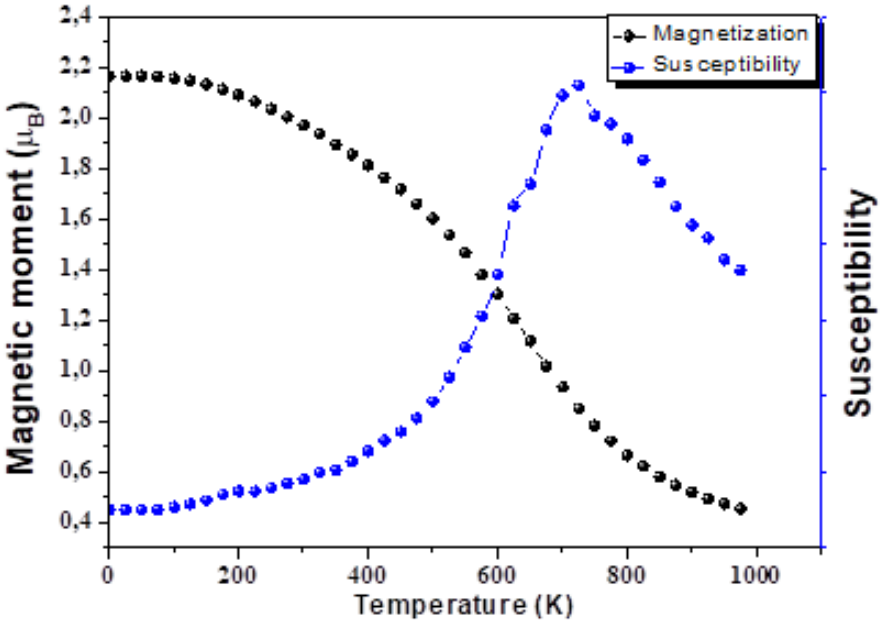

Figure 3.5: Magnetic moment and susceptibility as a function of temperature [170]

The magnetization decreases with the increase of temperature, while the magnetic susceptibility increases in the range of 1-720K and decreases after 725 K. A second-order magnetic transition to the paramagnetic phase is observed around 725 K, which agrees with experimental value. For practical applications, an easy material to be prepared with low cost and strong ferromagnetic behavior at room temperature is highly recommended [182].

To compare the simulated magnetic properties of the cobalt spinel ferrite under the effects of the external magnetic field with the measured magnetic hysteresis loop, a conversion of the magnetic moment (μ_B) to the magnetization (emu/g) was done as follow:

$$M(emu/g) = \frac{5585}{MW} \times m(\mu_B) \tag{3.5}$$

Where m is the obtained total magnetic moment, and M is the Molecular Weight of $CoFe_2O_4$ (MW=234.62 g/mol).

Figure 3.6 shows the experimental (referred as Exp) and simulated (referred as MCS) magnetic hysteresis loop of $CoFe_2O_4$ at room temperature. It can be seen from figure 3.6 and table 3.4 that $CoFe_2O_4$ particles have a theoretical magnetization saturation of about 99.13 emu/g. A decrease in the magnetization is shown experimentally (Ms = 87.89

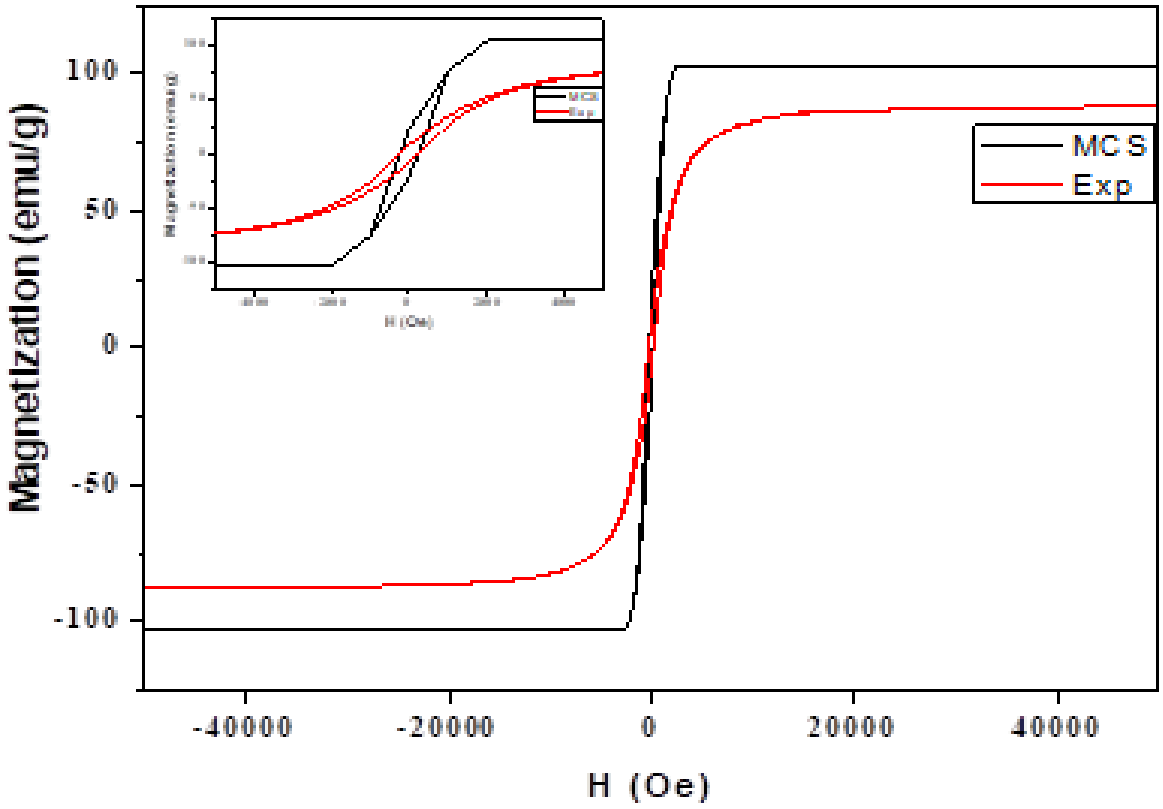

Figure 3.6: Theoretical (MCS) and experimental (Exp) magnetic hysteresis loop of $CoFe_2O_4$ at room temperature [170]

emu/g) compared to theoretical value because of the distribution of Co^{2+} and Fe^{3+} cations in the tetrahedral and octahedral sites, which is not obvious to control experimentally. Slight difference between the experimental and the theoretical coercive fields, which were found to be 229.50 Oe and 227.30 Oe, respectively. Our results present a good agreement with the obtained coercivity of $CoFe_2O_4$ synthesized by Solid-state reaction calcined at 1200 °C for 12h [164].

The obtained hysteresis loops M-H were converted to B-H by calculating the magnetic

	$Ms(emu/g)$	$Mr(emu/g)$	$Br(G)$	$H_{ci}(Oe)$	$H_{cb}(Oe)$	$(BH)_{max}(MG.Oe)$
MCS	99.13	22.18	1476.79	227.30	159.39	0.07
Exp	87.89	8.35	556.06	229.50	164.15	0.02
Exp [164]	81	7	—	219	—	—

Table 3.4: Magnetic parameters of $CoFe_2O_4$ at 300K obtained theoretically (MCS) and experimentally (Exp).

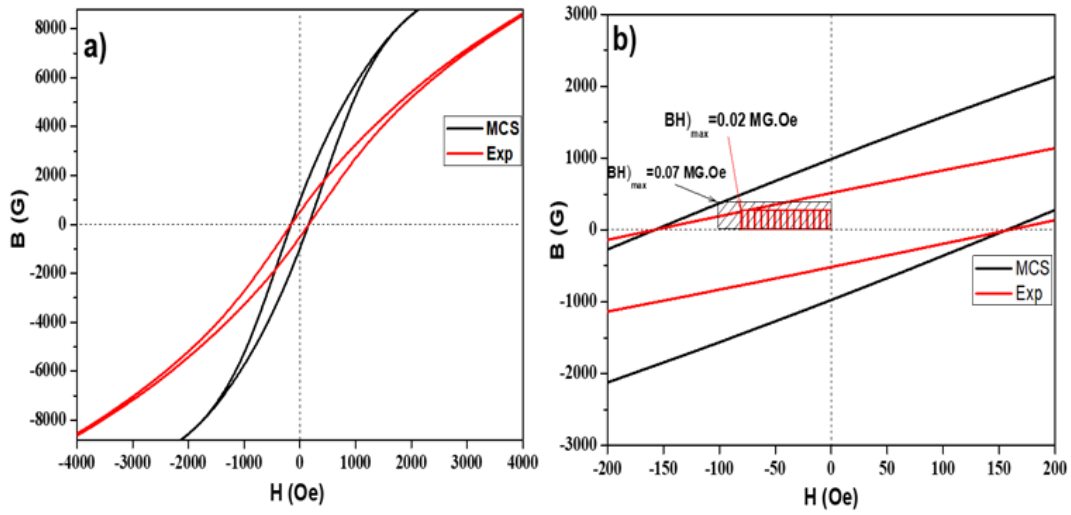

Figure 3.7: a) Magnetic flux density of $CoFe_2O_4$ as function of the magnetic field, b) maximum energy product calculated from the second quadrant of B-H hysteresis loop [170]

induction B using the following equation in the CGS:

$$B = H + 4\pi \times M \tag{3.6}$$

We present in figure 3.7-a) the B-H hysteresis loop at 300K. From which we calculated the energy density that is the largest rectangle inscribed under the second quadrant of the B-H curve (figure 3.7-b) [2]. It is found that the bulk cobalt spinel ferrite exhibits a maximum energy product of 0.02 MG.Oe at room temperature. Monte Carlo simulation showed a maximum energy product of about 0.07 MG.Oe. Up to our knowledge, no experimental works have been done to perform the maximum energy product of bulk $CoFe_2O_4$.

N	8	10	14	18	21	25	30	35
L (nm)	6.72	8.4	11.76	15.12	17.64	21	25.2	29.4

Table 3.5: Number of the unit cell of $CoFe_2O_4$ (N) and the corresponding real particle size L (nm).

3.3 Size effects on the magnetic properties of $CoFe_2O_4$ nanoparticles

3.3.1 Model and computational details

To simulate the effects of the external magnetic field on the magnetic properties of $CoFe_2O_4$ single nanoparticles, a classical Monte Carlo simulation based on the Metropolis algorithm was used within Ising Model (Hamiltonian described in equation III.2) with free boundaries conditions. To describe the real particle sizes (L), we considered the product of the number of unit cells N and the lattice constant a (a = 8.40 $\mathring{A}$ for $CoFe_2O_4$ compound). A range from N = 8 to 35 of unit cells, corresponding to real particle sizes from L = 6.72 nm to 29.4 nm (see table 3.5) were chosen to study the size effects on the magnetic properties of $CoFe_2O_4$ single nanoparticles. High Monte Carlo steps up to 10^5 were chosen, where the equilibrium was reached after 10^4 steps.

3.3.2 Magnetic properties

To study the finite size-effects on the magnetic properties of $CoFe_2O_4$ single nanoparticles, the magnetic hysteresis loops at Room temperature for different size of nanoparticles was computed. Figure 3.8 shows the magnetic moment as a function of the applied magnetic field. We observe that in the absence of an external magnetic field, $CoFe_2O_4$ has a total magnetic moment of about 1.60 μ_B at room temperature for a size around 21 nm and a slight decrease is shown with the decrease of particle size.

To compare our results with those obtained experimentally, a unit conversion of the magnetic moment (μ_B) to the magnetization (emu/g) was done within the formula (3.5).

The Magnetization in (emu/g) as a function of the magnetic field is presented in figure 3.9. The remanent magnetization remains a large fraction of the saturation magneti-

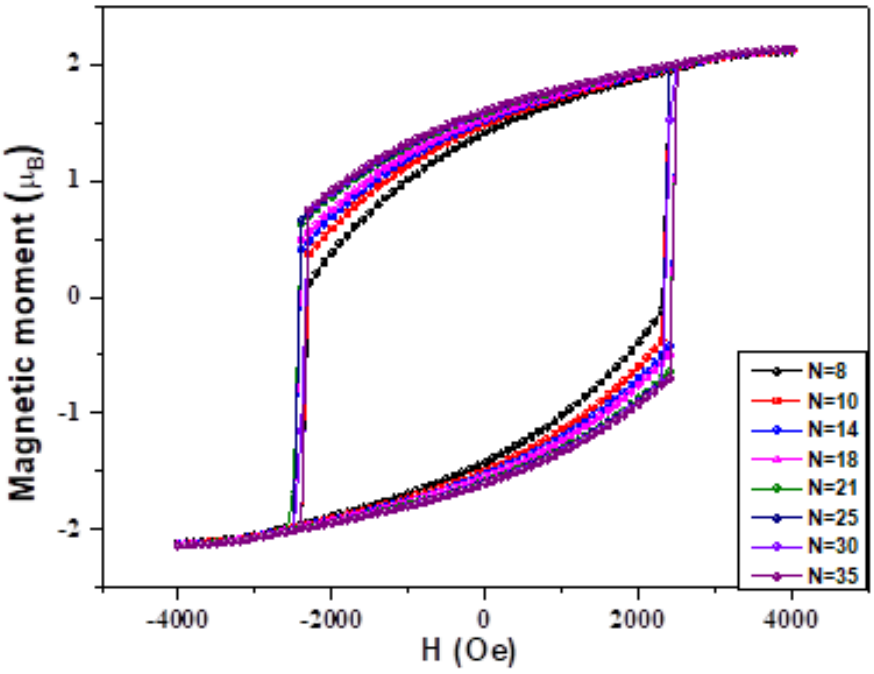

Figure 3.8: Magnetic moment as a function of the external magnetic field [92].

zation leading to a rectangular-like hysteresis with a small difference in the remanent magnetization with the increase of the particles size.

To better describe the finite size effects, we plot the saturation magnetization (Ms), the squareness ratio (Mr/Ms) and the coercive field of $CoFe_2O_4$ calculated at room temperature as a function of the size of particles, respectively.

It is found from figure 3.10 that the saturation magnetization (Ms) increases as the size of particles increased. This increase in Ms is generally due to the distribution of Co^{2+} and Fe^{3+} cations in the tetrahedral and octahedral sites, which is not obvious to control experimentally. Thus, the increase of the particles size gives rise to enhance the contribution of the core on the magnetic properties instead of the surface contribution. Experimentally, the highest values of Ms were obtained for $CoFe_2O_4$ nanoparticles synthesized by the Thermal decomposition method. Y. Kumar et al. have found a high saturation magnetization of 83.12 emu/g for an average particles size of 35 nm which is explained by the localized spin canting [183]. Liu et al. have used the mechanical milling to enhance the magnetic properties of $CoFe_2O_4$ and it was found that the saturation magnetization decreases slightly after a short milling time [184]. The evolution of the magnetic properties of Cobalt ferrite nanoparticles as a function of the particles size and

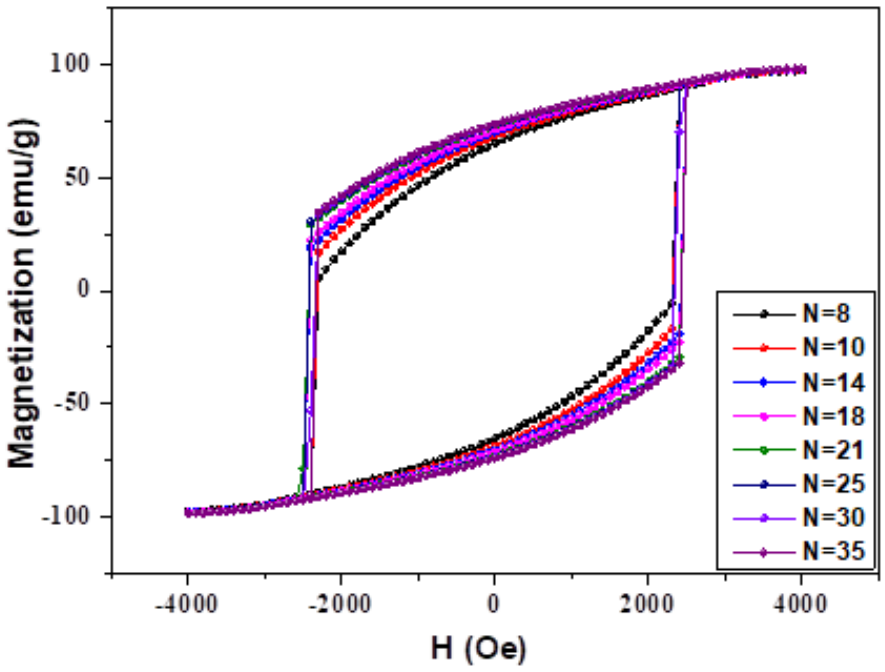

Figure 3.9: Magnetic hysteresis loop of $CoFe_2O_4$ nanoparticles at room temperature [92].

shape was done by Ortega et al. and it was found that the saturation magnetization increases with particle size to 20 nm and remains approximately around 80-90 emu/g [185].

Figure 3.11 displayed the squareness ratio (Mr/Ms) as a function of the particles size. The squareness ratio (Mr/Ms) as a function of the particles size shows an increase of the ratio towards high value (0.75 for 21 nm). Our results accord with the Stoner-Wohlfarth model which predicts high values of the squareness ratio of non-interacting single-domain particles with a cubic anisotropy (0.832 if $K_1 > 0$ or 0.87 if $K_1 < 0$) [21].

As it is presented in figure 3.12, the coercive field (Hc) as a function of the particles size shows an increase of the coercive field as the particles size increased and reaches a maximum at 21 nm. Afterwards, the coercive field decreases. The single-domain size limit is found to be about 21 nm which indicates the transition from magnetic single-domain (where Hc is due essentially to the rotation of all spins) to the magnetic multi-domain (characterized by the influence of the domain walls instead of the rotation of spins) [186].

Thereafter, the M-H hysteresis loop has been converted to B-H hysteresis in order to calculate the maximum energy product using the formula (3.6). The calculated magnetic

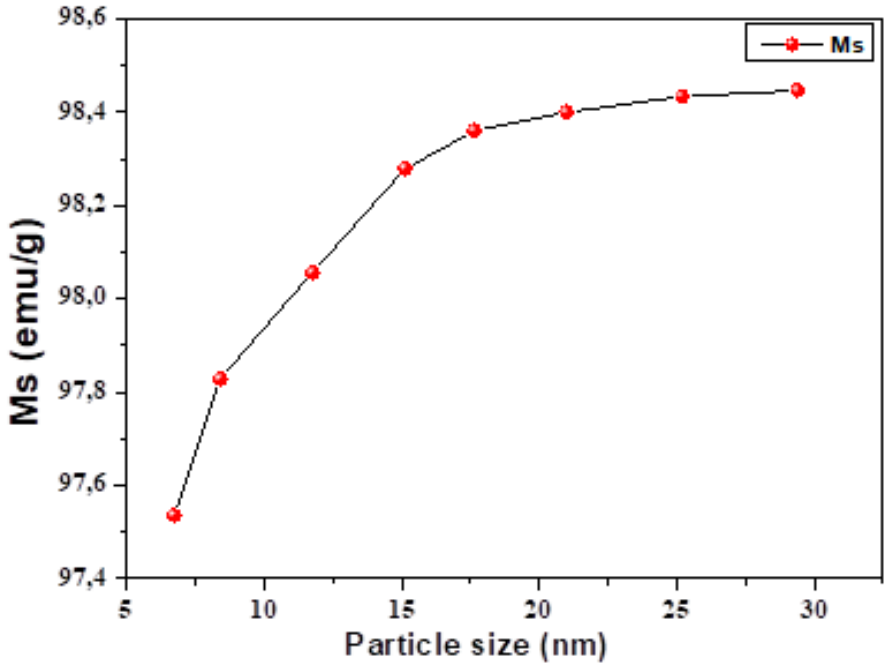

Figure 3.10: Particles size dependence of the saturation magnetization Ms [92].

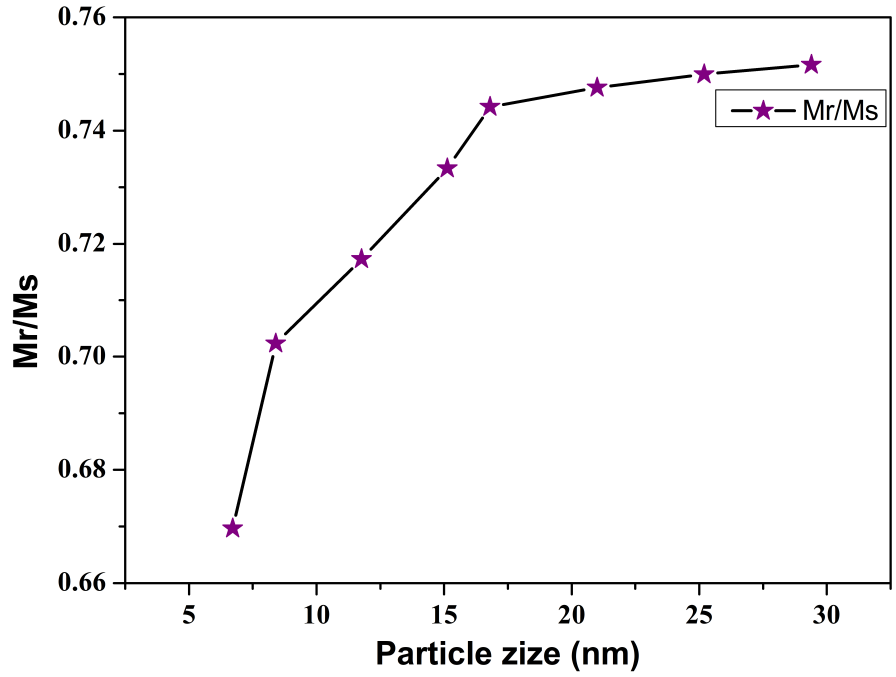

Figure 3.11: Particles size dependence of the squareness ratio (Mr/Ms) [92].

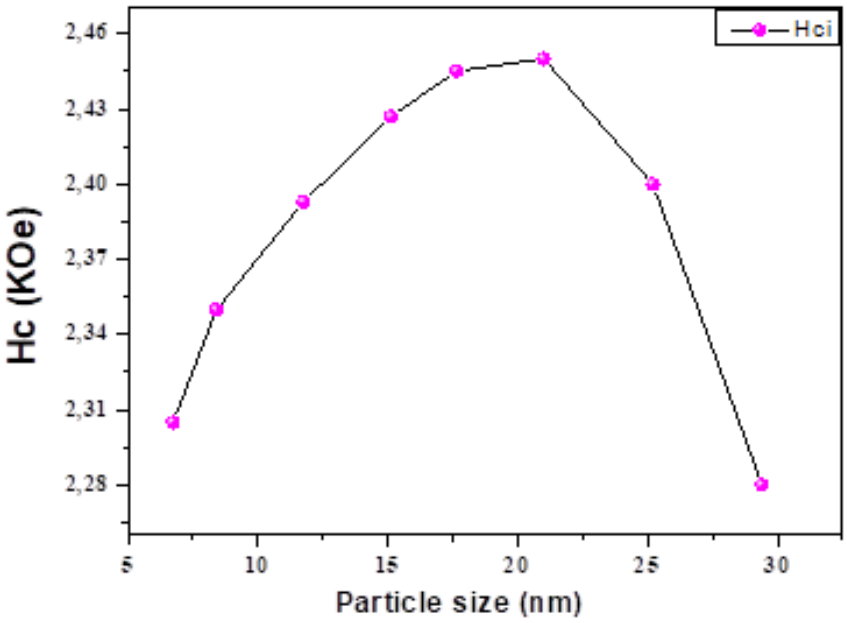

Figure 3.12: Particles size dependence of the coercive field (Hc) [92].

induction B as a function of the magnetic field (figure 3.13) shows a large hysteresis area with high residual magnetism (Br = 4.9 KG for 21 nm) which defines the hard magnetic materials.

To evaluate the potential of $CoFe_2O_4$ nanoparticles in permanent magnet applications, we extract the energy density (called also the maximum energy product) from the second quadrant of the B-H hysteresis curve [2]. Figure 3.14 displays the maximum energy product as a function of the particles size. The obtained $(BH)_{max}$ increases with the increase of the particle size in the single-domain region and decreases with any further increase of the particle size. The obtained maximum value of the $(BH)_{max}$ was found about 2.83 MG.Oe for an average particle size of 21 nm while it increased to 2.45 MG.Oe for a particle size of about 29.4 nm. As shown in table 3.6, The highest experimental value of $(BH)_{max}$ reported in the literature for cubic shaped $CoFe_2O_4$ nanoparticles (synthesized by thermal decomposition technique with particles size of about 35 nm) is about 2.41 MG.Oe [183].

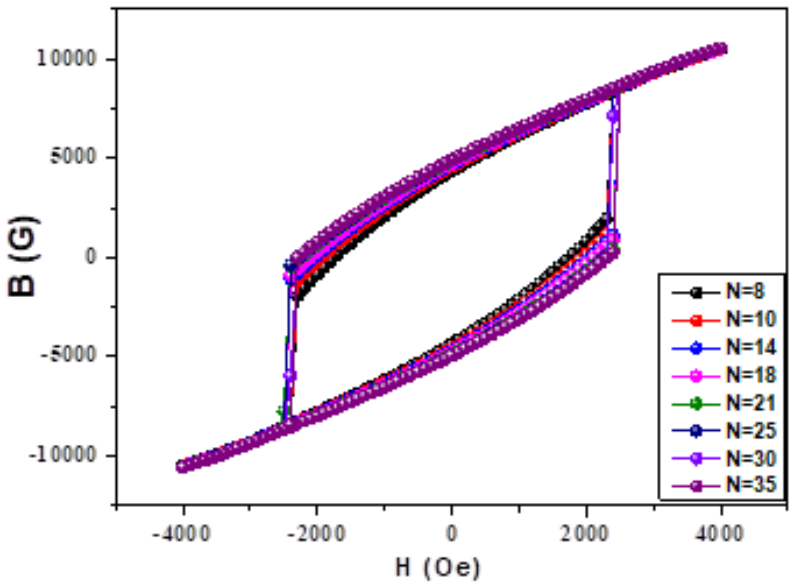

Figure 3.13: B-H hysteresis loop of $CoFe_2O_4$ at Room temperature [92].

3.4 Conclusion

In this chapter, we have presented a combined experimental and theoretical investigation of the magnetic properties of bulk $CoFe_2O_4$ and cubic-shaped $CoFe_2O_4$ nanoparticles.

The first part of this chapter was devoted to the study of the magnetic properties of bulk $CoFe_2O_4$ using both experimental and theoretical investigations. The Solid-state reaction was used to synthesize pure bulk cobalt spinel ferrite. The prepared sample has been subjected to some techniques to prove its structural purity and to analyze its structural and microstructural properties. The obtained experimental structural results have been used within Density Functional theory in order to study the electronic properties of $CoFe_2O_4$ and to calculate the exchange coupling interactions and the magnetocrystalline anisotropy. The magnetic properties of bulk $CoFe_2O_4$ have been studied and analyzed experimentally and theoretically using Monte Carlo simulation with periodic boundaries conditions. It was found that the prepared $CoFe_2O_4$ material presents a low maximum energy product of about 0.02 MG.Oe and 0.07 MG.Oe from experimental measurements and Monte Carlo simulation, respectively. Our results demonstrate that bulk $CoFe_2O_4$ exhibits low performance. However, it can be used as permanent magnet material.

Furthermore, we have reported in the second part of this chapter the size-effects on

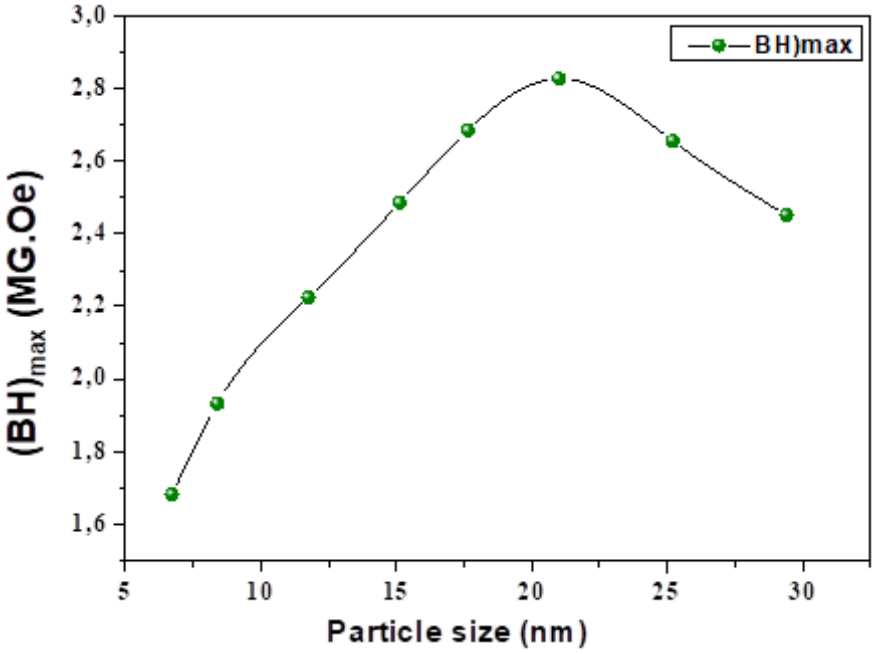

Figure 3.14: Particles size dependence of the maximum energy product $(BH)_{max}$ [92].

Work	Particle size (nm)	Ms (emu/g)	Mr/Ms	Hc (KOe)	$(BH)_{max}(MG.Oe)$
Liu et al. [184]	> 100	70	0.6	5.1	2.0
Ortega et al. [185]	44	77.8	0.71	3.0	2.3
Kumar et al. [183]	35	83.12	0.74	3.2	2.41
Lamouri et al.	21	98.4	0.75	2.45	2.83
	29.4	98.45	0.75	2.28	2.45

Table 3.6: The Magnetic parameters of $CoFe_2O_4$ nanoparticles at 300K obtained in this study and from other works.

the magnetic properties of $CoFe_2O_4$ spinel ferrite single nanoparticles using Monte Carlo simulation within the Ising model. Free boundaries conditions were used to simulate the cubic nanoparticles with different sizes. It was shown that saturation and remanent magnetization increased with the increase of the particles size. Rise of the squareness ratio (Mr/Ms) towards high values is observed. Furthermore, the single-domain size limit is shown for the size of 21 nm. Besides, we evaluated the performance of the cubic-shaped $CoFe_2O_4$ permanent magnet in terms of the maximum energy product. A high value of the $(BH)_{max}$ of about 2.83 MG.Oe at room temperature was achieved for an average size of particles of 21 nm. The obtained results allowed us to estimate the theoretical limits of the magnetic properties of the cubic shaped $CoFe_2O_4$ nanoparticles and pave the way for the development of $CoFe_2O_4$ spinel ferrites for permanent magnet applications. For instance, some other parameters such as the inter-particles interactions and the orientation of the nanoparticles are introduced in our current work to clarify their influence on the magnetic properties of such materials.

Chapter 4

Enhancement of the magnetic properties of $SrFe_{12}O_{19}$ hexaferrites

4.1 Introduction

Since their discovery in the 1950s by Philips [187], M-type hexagonal ferrite materials have attracted great attention of researchers worldwide because of their good chemical stability, low synthesis cost, high resistivity to corrosion, high saturation magnetization, moderate coercivity and others [188–190]. Nowadays, the basic structural, electrical and magnetic properties of the M-type hexagonal ferrite play a crucial role in the determination of the most suitable application in the modern industrial technology in active use such as magnetic recording media, microwave absorption devices, biosensors and permanent magnet applications [191–193].

M-type hexagonal ferrites (known as hexaferrites) with the general formula $MFe_{12}O_{19}$ (M=Sr, Pb, Ba...) crystallize in the magnetoplumbite-type crystal having the hexagonal structure with space group P63/mmc (194). This structure is composed of ten closed-packed layers of oxygen ions along the c-axis, forming RSR^*S^* blocks sequence. R block refers to the hexagonal structure of three oxygen layers containing the divalent M^{2+} cation in the middle layer. S block describes the spinel structure with two oxygen layers . R^* and S^* represent the corresponding R and S blocks with a rotation of 180° around the

c-axis. Fe^{3+} ions occupy five crystallographic sites as three octahedral sites (2a, $4f_2$, 12k), one tetrahedral site ($4f_1$) and one trigonal bipyramidal site (2b). The bonding length between oxygen and iron in the five sites lead to a super-exchange interaction that split the magnetic structure of the M-type hexaferrites to spin-up and spin-down sublattices with a collinear ferrimagnetic order [36, 194].

Significant enhancement of the magnetic properties of M-type Strontium hexaferrite has been achieved by using various synthesis methods with controlled conditions. For instance, the conventional ceramic method has been widely used as a simple method to prepare and produce ferrite magnetic materials. However, this method has shown a weakness regarding the control of the morphology and the particles size and improved intrinsic coercivity of materials [8, 170]. Synthesis techniques based on chemical routes have taken the interest of experimentalists from different disciplines because of the high quality and homogeneous powders [195–198]. Although, several parameters should be taken into consideration to optimize the synthesis process of nanoferrites such as the choice of the starting precursors and their stoichiometry, pH value of the solution, heat treatment and others. Zi et al., have studied the structural and magnetic properties of M-type strontium hexaferrite particles prepared by a modified chemical coprecipitation route [194]. A comparison between the conventional sol-gel and modified sol-gel synthesis routes were performed by Eikeland et al., to enhance the magnetic properties of $SrFe_{12}O_{19}$ through morphology controlling of the nanocrystallites [199]. Jing et al. have synthesized $SrFe_{12}O_{19}$ nanoribbons via polyvinylpyrrolidone (PVP) sol-gel assisted electrospinning method followed by heat treatment in the air [200]. Urbano-Pena et al., have used the polymeric complex (Pechini) method to synthesize $SrFe_{12}O_{19}$ powders with various calcination temperatures. However, a secondary phase of hematite was found in all prepared samples, which affects the structural and magnetic properties of $SrFe_{12}O_{19}$ [201]. Liu et al., used oily Cold Mill Sludge by the Citrate Precursor method to prepare nano-$SrFe_{12}O_{19}$ with controlled composition and enhanced magnetic properties [202]. Even though a large number of studies have performed the magnetic properties of $SrFe_{12}O_{19}$ nanoparticles using different synthesis methods and conditions, not many attempts have been devoted to

compare the structural and magnetic properties of M-type Strontium hexaferrite through changing the synthesis methods with some common conditions.

This chapter will present our contribution to a possible improvement of the magnetic properties of M-type Strontium hexaferrites. In the first part, we studied the effect of the synthesis route on the magnetic properties by using two simple, easy and low cost synthesis methods to prepare $SrFe_{12}O_{19}$ nanoparticles viz. Sol-gel auto-combustion and co-precipitation methods with some common conditions. The second part will be focused on the substitution effects on the electronic and magnetic properties of $SrFe_{12}O_{19}$ by using Density Functional Theory.

4.2 Effect of the synthesis route on the magnetic properties of $SrFe_{12}O_{19}$ nanoparticles

4.2.1 Sample preparation

Coprecipitation and sol-gel auto-combustion methods were adopted in this work as simple chemical routes to synthesize M-type Strontium hexaferrite powders with good magnetic properties.

4.2.1.1 Co-precipitation method

Stoichiometric amount of $SrCl_2$ (sigma Aldrich, 99.99 %) and $FeCl_3.6H_2O$ (Sigma Aldrich, 97 %), were dissolved in 30ml of deionized water and stirred at 80 °C for 30min. An aqueous solution of NaOH was added drop by drop to the solution containing the started materials until $pH \approx 11$. The basic solution is stirred then at 80°C for 1h30" and washed several times to remove the excess of water-soluble salts and dried at 80 °C overnight. Calcination at 1000 °C for 6 hours was done to obtain a black powder of $SrFe_{12}O_{19}$ nanoparticles.

4.2.1.2 Sol-gel Auto-combustion method

To prepare $SrFe_{12}O_{19}$ nanoparticles, we used $Sr(NO_3)_2$ (sigma Aldrich, 99.99 %) and $Fe(NO_3)_3.9H_2O$ (sigma Aldrich, 99.99 %) as started materials with a molar ratio of 11.5 of Fe^{3+} : Sr^{2+} to avoid the formation of $\alpha - Fe_2O_3$. The precursors were dissolved in 25ml of distilled water with magnetic stirring at Room Temperature. An aqueous solution of citric acid with a molar ratio of 1 to metal cations was added to the solution containing started precursors and stirred at room temperature for 45min. We added NH_4OH drop wise to the solution to adjust pH = 7. The neutralized solution was stirred magnetically at 120 °C for 2 hours to form of a viscous gel after the evaporation of all water molecules from the mixture. The gel was heated at 200 °C until the apparition of a grey powder that was calcined at 1000 °C for 6 hours to obtain $SrFe_{12}O_{19}$ nanoparticles.

The obtained samples have been referenced as SFO_CP and SFO_SG/AC for the prepared samples using Co-precipitation and Sol-gel Auto-combustion methods, respectively. The structural phase was verified using the X-ray diffractometer with Cu-K_α radiation ($\lambda = 1.5407$ $\mathring{A}$). Scanning Electron Microscope (FEI Quanta 450 FEG) was used to perform the microstructural properties of the prepared samples and the magnetic properties were performed using a Magnetic Property Measurement System (MPMS) from Quantum Design.

4.2.2 Structural and microstructural analysis

4.2.2.1 X-Ray Diffraction (XRD)

The X-ray diffraction patterns of $SrFe_{12}O_{19}$ nanoparticles synthesized using Coprecipitation (SFO_CP) and sol-gel auto-combustion (SFO_SG/AC) methods are shown in figure 4.1. We show the identification of a single-phase $SrFe_{12}O_{19}$, which crystallizes in the hexagonal structure (space group P63/mmc N° 194) according to the Joint Committee Powder Diffraction Standards (JCPDS file: 01-084-1531). No obvious impurities were detected for both samples, indicating the purity of the prepared samples.

The lattice parameters and volume of SFO_CP and SFO_SG/AC samples were calcu-

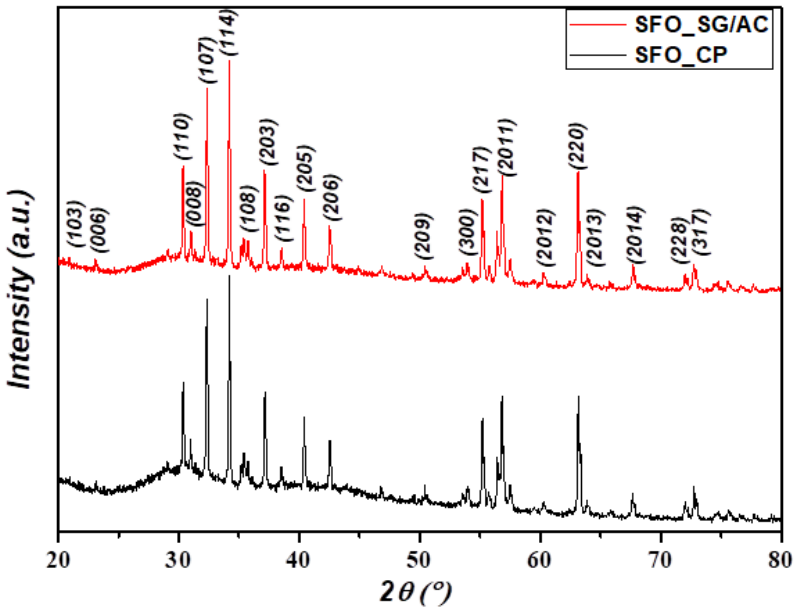

Figure 4.1: XRD spectra of $SrFe_{12}O_{19}$ synthesized by Coprecipitation (SFO_CP) and Sol-gel auto-combustion (SFO_SG/AC) methods.

lated using the following formula for the hexagonal structure:

$$\sin^2\theta = \frac{\lambda^2}{4}\left[\frac{4}{3}\frac{(h^2+hk+k^2)}{a^2} + \frac{l^2}{c^2}\right] \tag{4.1}$$

$$V = \frac{\sqrt{3}}{2}a^2c \tag{4.2}$$

Where λ is the X-ray wavelength ($\lambda = 1.5407$ $\mathring{A}$), h, k, l are the Miler indexes and θ is the diffraction angle.

The calculated parameters listed in table 4.1 are similar to those obtained by Jing et al., using electrospinning technique [200].

Debye-Scherrer formula was used to calculate the crystallite size of the prepared nanoparticles. The average crystallite size was found about 37.8 nm and 85.4 nm for SFO_CP and SFO_SG/AC, respectively.

4.2.2.2 Scanning Electron Microscopy (SEM)

Figure 4.2 shows the scanning electron microscopy (SEM) micrographs of SrFe12O19 nanoparticles synthesized by coprecipitation (SFO_CP) and Sol-gel auto-combustion (SFO_SG/AC).

Code	Lattice parameters (Å)		c/a	Volume (Å^3)	Crystallite size (nm)
	a (Å)	c (Å)			
SFO_SG/AC	5.8870	23.0634	3.9177	692.2103	85.4
SFO_CP	5.8838	23.0887	3.9241	692.2343	37.8
Jing et al. [200]	5.872	23.036	3.9171	687.80	46.3

Table 4.1: Lattice parameters, c/a ratio, unit cell volume and the average crystallite size of $SrFe_{12}O_{19}$ for the XRD spectra.

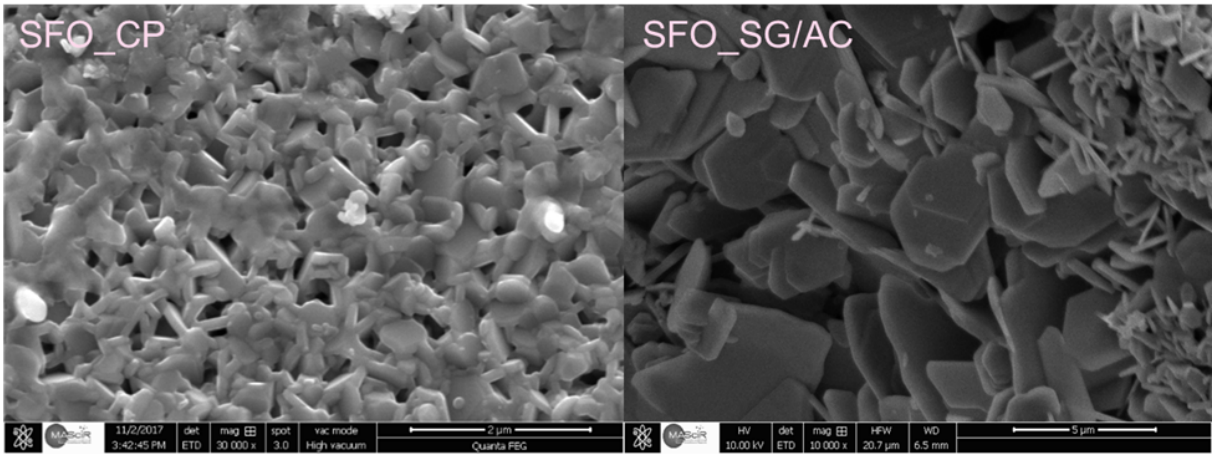

Figure 4.2: SEM images of $SrFe_{12}O_{19}$ synthesized by Coprecipitation (SFO_CP) and Sol-gel auto-combustion (SFO_SG/AC) methods.

The SEM images show that the majority of the grains are well-defined as hexagonal platelets-like morphology, which is very reproducible in these materials as reported in several studies [203–205]. As we can see clearly from figure 4.2, the obtained grains within the sol-gel auto-combustion (SFO_SG/AC) method are larger with an average size of about 1 μm compared to the obtained grain using the coprecipitation (SFO_CP) method with a grain size around 0.5 μm. Furthermore, agglomerated nanoparticles were observed in the SFO_CP samples, which could be related the synthesis conditions of the coprecipitation counter to the sol-gel auto-combustion method in which the citric acid inhibit the agglomeration and affect the size of the particles.

4.2.3 Magnetic characterization

The magnetic hysteresis loops of the prepared samples are illustrated in figure 4.3. From the (M-H) hysteresis loop, we can see that the prepared sample using the sol-gel auto-

Code	Ms (emu/g)	Mr (emu/g)	Mr/Ms	Hci (KOe)	Br (KG)	Hcb (KOe)	(BH)max (MG.Oe)	
							Experimental	Theoretical
SFO_SG/AC	95.11	46.39	0.49	5.20	2.82	1.95	1.36	1.99
SFO_CP	80.63	39.74	0.49	5.28	2.42	1.89	1.13	1.45

Table 4.2: Magnetic parameters of $SrFe_{12}O_{19}$ nanoparticles at room temperature

combustion method (SFO_SG/AC) exhibits high saturation magnetization and remanent magnetization of about 95.11 emu/g and 46.39 emu/g, respectively. Thus, the prepared sample using Coprecipitation method (SFO_CP) exhibits a saturation magnetization of about 80.63 emu/g and remanent magnetization of about 39.74 emu/g. This difference of the saturation magnetization can be explained by the difference of the crystallite size. Considering that the surface of the particle has an insignificant net moment compared to the inner layer, the contribution to the total magnetic moment comes essentially from the core of the particles. As the particles size increases, the ratio of the surface layer to the core decreases leading to the increase of the saturation magnetization [92].

Al-Garalleh et al., have studied the effects of the synthesis route on the structural and magnetic properties of rare-earth-doped M-type Strontium hexaferrite using high-energy ball-milling and sol-gel auto-combustion methods [206]. It was found that, for the prepared samples by the sol-gel auto-combustion method, the saturation magnetization and the remanent magnetization increase with the increase of the sintering temperature. They obtained high saturation magnetization and remanent magnetization of about 66.3 emu/g and 31.5 emu/g, respectively. As it is shown in the figure 4.4 and table 4.2, a comparable intrinsic coercivity of about 5.20 KOe and 5.28 KOe were obtained for the samples prepared by sol-gel auto-combustion and Coprecipitation methods, respectively.

The magnetic induction has been calculated from the Magnetization using the following formula for the CGS system of units:

$$B = H + 4\pi \times M \tag{4.3}$$

As presented in the B-H hysteresis loop (figure 4.5) and table 4.2, the prepared sample using the sol-gel auto-combustion method (SFO_SG/AC) has a higher residual magnetic

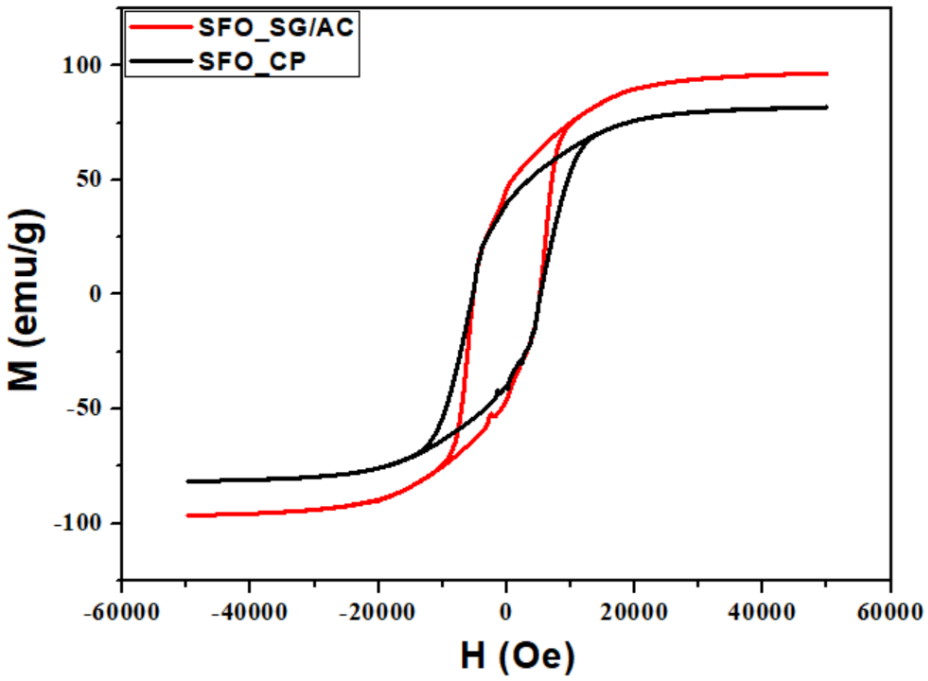

Figure 4.3: Magnetic hysteresis loop M-H at room temperature of $SrFe_{12}O_{19}$ synthesized by Coprecipitation (SFO_CP) and Sol-gel auto-combustion (SFO_SG/AC) methods.

flux density of about 2819.93 G compared to the prepared sample with the coprecipitation method which has a residual magnetic flux density of about 2415.56 G. This parameters is considered as an important parameter for permanent magnet applications.

To evaluate the strength of the prepared materials for permanent magnet applications, it is necessary to determine the maximum energy product $(BH)_{max}$ which is related to the magnetic field (H) and the flux density (B). Experimentally, this measure is extracted from the second quadrant of the B-H hysteresis loop. Figure 4.5 presents the energy product of $SrFe_{12}O_{19}$ synthesized by coprecipitation (SFO_CP) and sol-gel auto-combustion (SFO_SG/AC) methods as a function of the applied magnetic field. Theoretically, the maximum energy product of hard magnetic materials can be calculated using the following formula:

$$(BH)_{max} = \frac{\mu_0 Mr^2}{4} \tag{4.4}$$

Where μ_0 is the vacuum permeability ($\mu_0 = 1$ in the CGS system of units) and Mr is the remanent magnetization.

As it is presented in figure 4.6 and table 4.2, the maximum energy product of $SrFe_{12}O_{19}$

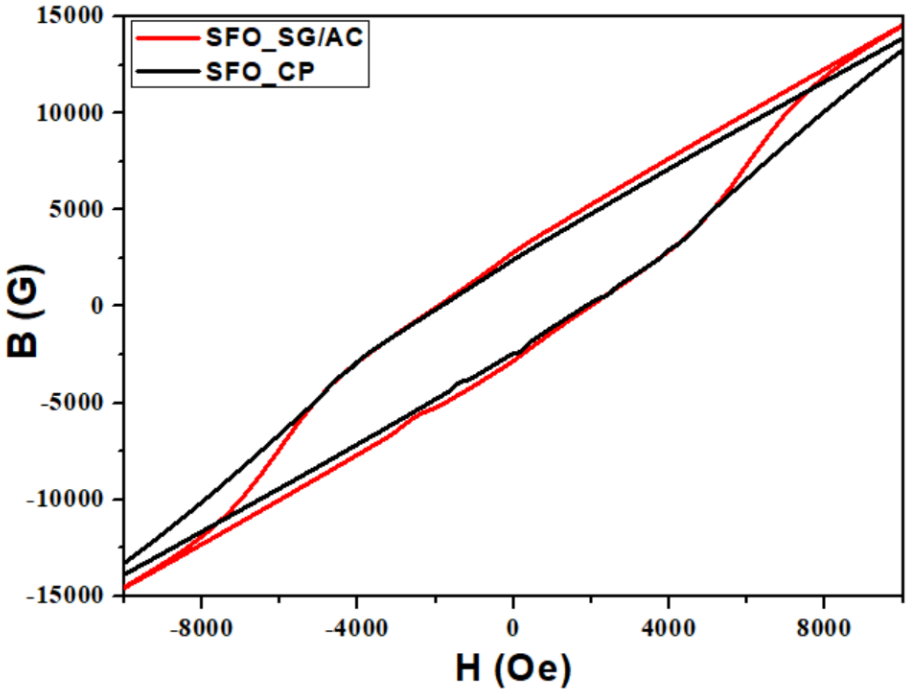

Figure 4.4: B(H) hysteresis at room temperature of $SrFe_{12}O_{19}$ synthesized by Coprecipitation (SFO_CP) and Sol-gel auto-combustion (SFO_SG/AC) methods.

nanoparticles prepared by the sol-gel auto-combustion method (1.36 MG.Oe) is greater than the obtained value for $SrFe_{12}O_{19}$ nanoparticles prepared by the coprecipitation method (1.13 MG.Oe). The calculated theoretical values of the maximum energy product of $SrFe_{12}O_{19}$ are always higher than the experimental values for both synthesis routes which can be explained by the imperfect magnetic orientation of the samples [36].

4.3 Substitution effects on the electronic and magnetic properties of $SrFe_{12}O_{19}$

4.3.1 Computational details

In this work, DFT calculations were performed with the full-potential linearized augmented plane wave (FP-LAPW) as implemented in the Wien2k package [173, 174]. Spin polarized calculations were done according to the ground state ferrimagnetic ordering of Fe spins. Exchange correlation effect was described using the Perdew-Burke-Ernzerhof Generalized Gradient approximation (PBE-GGA) [175]. A cut-off parameter $R_{MT} \times K_{max} =$

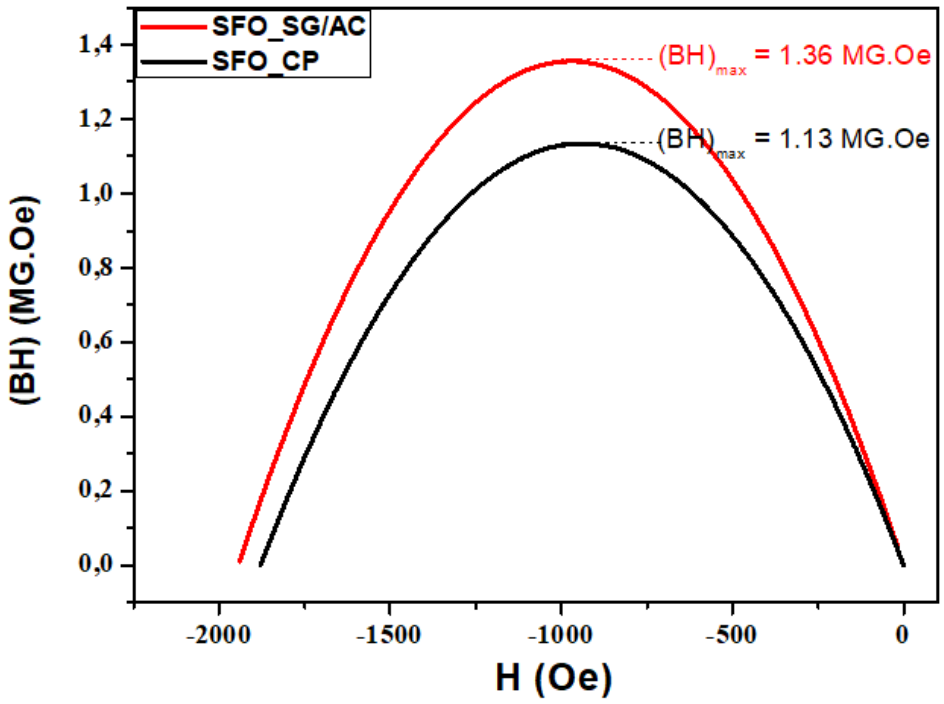

Figure 4.5: Energy product of $SrFe_{12}O_{19}$ synthesized by Coprecipitation (SFO_CP) and Sol-gel auto-combustion (SFO_SG/AC) methods.

7 was used to ensure the convergence, where R_{MT} and K_{max} represent the Muffin tin-radii and the largest K-vector for the basic functions in the reciprocal space, respectively. The self-consistency is obtained by 300 K-points in the irreducible symmetry wedge of the first Brillouin zone. The iteration process is repeated until the calculated total energy of the crystal converges to less than 10^{-5} Ry.

4.3.2 Structural stability

There has been several experimental investigations on substituted strontium hexaferrite to further improve its magnetic properties. However, limited theoretical studies on substituted M-type hexaferrite have been carried out compared to experimental studies. Dixit et al., have studied the site preferences and the magnetic properties of Ga/In and Al-substituted Strontium hexaferrite using ab initio calculations [207]. The possibility of substitution of various ions at the Fe^{3+} sites and its effects on magnetic properties of strontium hexaferrite have been investigated by Dixit et al., using a total of 21 elements M (M ≡ Sc, Al, Ti, P, Ga, Sn, In, Co, Ni, As, Bi, Sb, Ag, Cu, Ir, Pb, Au, Pt, Pd, Tl,

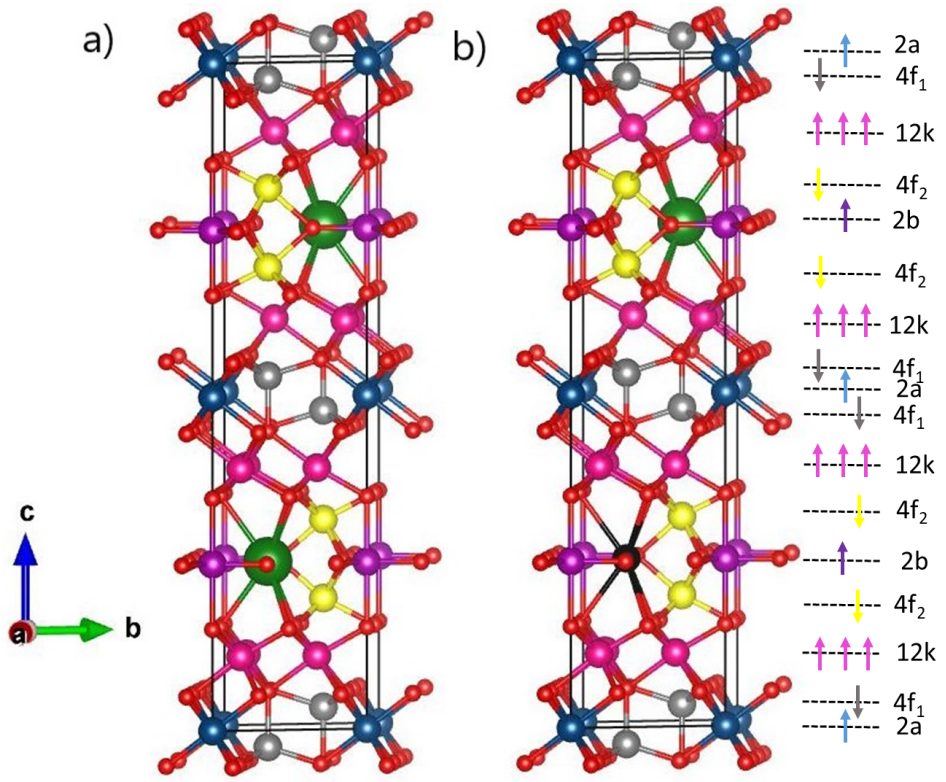

Figure 4.6: Schematic representation of the unit cell of : a) $SrFe_{12}O_{19}$ and b) Co-$SrFe_{12}O_{19}$.

and Br) [208]. As it has been proved in their work, each substitution of impurity atoms at the Fe sites is unique and modifies the magnetic properties in a distinct manner.

In this part of our thesis project, we are more interested in studying the effect of the substitution of Strontium element ($Sr_{0.5}Co_{0.5}Fe_{12}O_{19}$) instead of Fe sites on the electronic and magnetic properties of $SrFe_{12}O_{19}$.

Figure 4.6(a) shows the unit cell of $SrFe_{12}O_{19}$ compound. Two large green spheres represent Sr atoms, while small red spheres represent O atoms. Fe atoms in each sites are presented by different colors: 2a (blue), $4f_1$ (grey), 12k (pink), $4f_2$ (yellow), and 2b (purple). Figure 4.6(b) shows the Co-substituted $SrFe_{12}O_{19}$, where one of Sr atoms is replaced by Cobalt atom (black sphere).

To study the effect of Cobalt substitution on the electronic and magnetic properties of M-type Strontium hexaferrite, we first studied the possibility of such substitution and the structural stability of the substituted Strontium hexaferrites. The substitution energy

was then calculated using the following equation [208]:

$$E_{sub} = E(Sr_{0.5}Co_{0.5}Fe_{12}O_{19}) - [E(SrFe_{12}O_{19}) - E(Sr) + E(Co)] \quad (4.5)$$

Where E($Sr_{0.5}Co_{0.5}Fe_{12}O_{19}$) is the total energy per unit cell of Co-substituted $SrFe_{12}O_{19}$, E($SrFe_{12}O_{19}$) is the total energy per unit cell of $SrFe_{12}O_{19}$. E(Sr) and E(Co) represent the cohesive energy of Sr and Co elements in their ground state structures, respectively.

A negative value of E_{sub} was found (E_{sub} = -3.101 eV), which indicates that the unit cell of $Sr_{0.5}Co_{0.5}Fe_{12}O_{19}$ has lower energy than the pure $SrFe_{12}O_{19}$ and therefore such substitution is thermodynamically favorable.

Before studying the electronic properties of $SrFe_{12}O_{19}$ and $Sr_{0.5}Co_{0.5}Fe_{12}O_{19}$, an optimization of the lattice parameters of both compounds was done by calculating the total energy of the system as a function of the lattice volume. It was found that the optimized lattice parameters of $SrFe_{12}O_{19}$ are a = 5.912 $\AA$ and c = 23.071$\AA$, while the lattice parameters of the Co-substituted M-type Strontium hexaferrite were found to be a = 5.892 $\AA$ and c = 23.078 $\AA$.

4.3.3 Electronic and magnetic properties

To study the electronic and magnetic properties of $SrFe_{12}O_{19}$ and $Sr_{0.5}Co_{0.5}Fe_{12}O_{19}$ compounds, the total and the partial densities of states have been plotted. Figure 4.8 presents the total and the partial densities of states (DOS) of pure $SrFe_{12}O_{19}$ hexaferrite.

As it is shown from figure 4.7, the valence band with a total width of 7.0 eV can be divided into two regions. The upper part (from the Fermi level to -1.5 eV) mainly dominated by Fe-3d orbitals hybridized with O-p states, while in the lower part (from -1.5 eV to -7.0 eV) we can see clearly the contribution of Sr element. Moreover, it is shown from figure 4.7 a clear crystal field splitting of Fe ions at the octahedral 2a, $4f_2$ and 12k, as well as Fe ions at the tetrahedral $4f_1$ sites. However, a complicated crystal field splitting is observed for Fe ions at the trigonal bipyramidal 2b sites, which can be

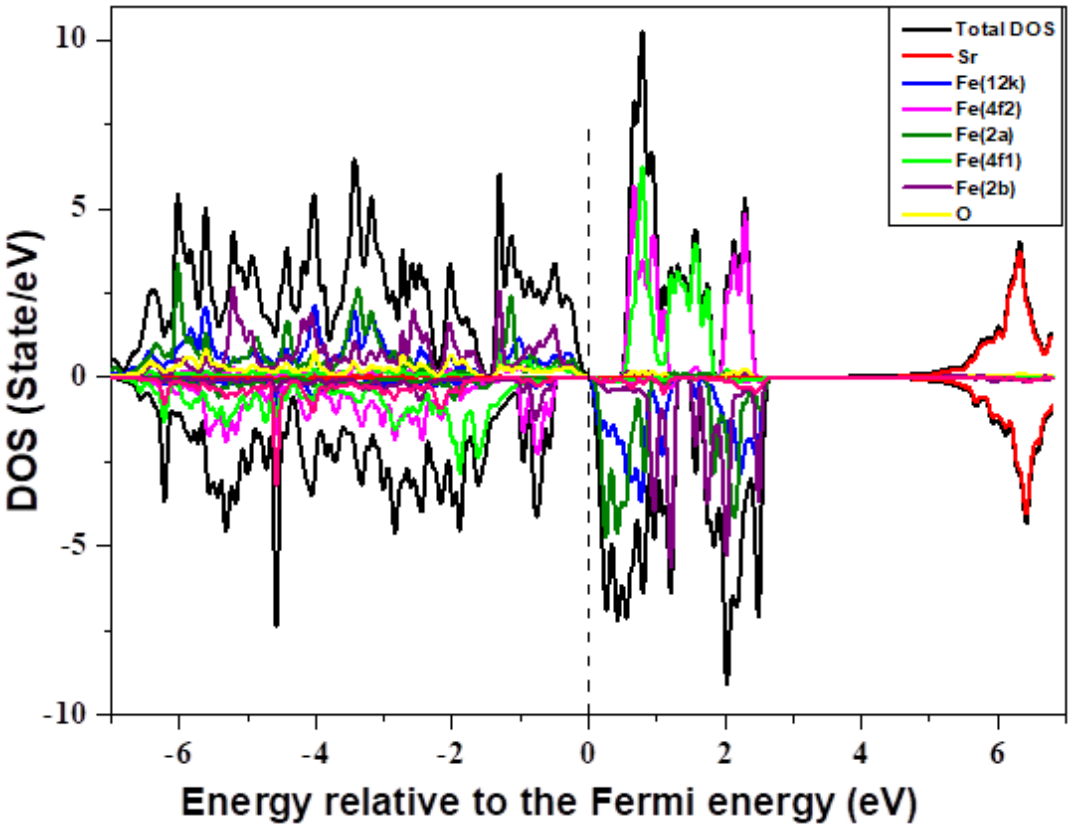

Figure 4.7: Total and Partial DOS of pure $SrFe_{12}O_{19}$ hexaferrite.

explained by the coordination in such type of sites.

Figure 4.8 presents the partial and the total DOS of both pure and substituted $SrFe_{12}O_{19}$ compounds. A clear change of the magnetic behavior is observed, where the co-substituted M-type hexaferrite $Sr_{0.5}Co_{0.5}Fe_{12}O_{19}$ shows a polarization at Fermi level which characterize the half-metallic materials.

To better illustrate this change of the electronic behavior, we plotted in figure 4.9, the total and the partial densities of states (DOS) of $Sr_{0.5}Co_{0.5}Fe_{12}O_{19}$ compound.

As it is presented in figure 4.9, the observed change in the densities of states between the pure and substituted M-type Strontium hexaferrite is mainly due to the insertion of the Cobalt element in 2d sites of Strontium.

The calculated magnetic moments for all inequivalent atoms in the unit cell of $SrFe_{12}O_{19}$ and $Sr_{0.5}Co_{0.5}Fe_{12}O_{19}$ compounds are listed in table 4.3. It was found that pure $SrFe_{12}O_{19}$ has a total magnetic moment of about 40.03 μ_B. The insertion of Cobalt ions in the M-type Strontium structure allow the increase of the total magnetic moment of $SrFe_{12}O_{19}$

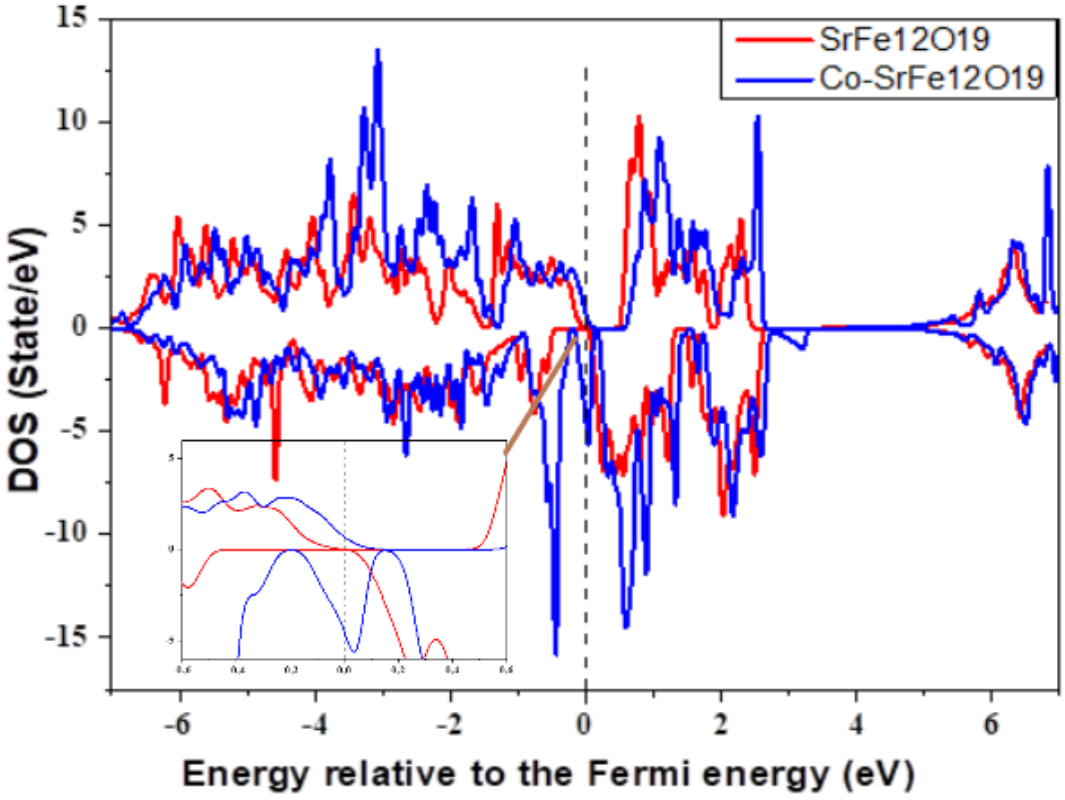

Figure 4.8: Total DOS of pure and substituted $SrFe_{12}O_{19}$ hexaferrite.

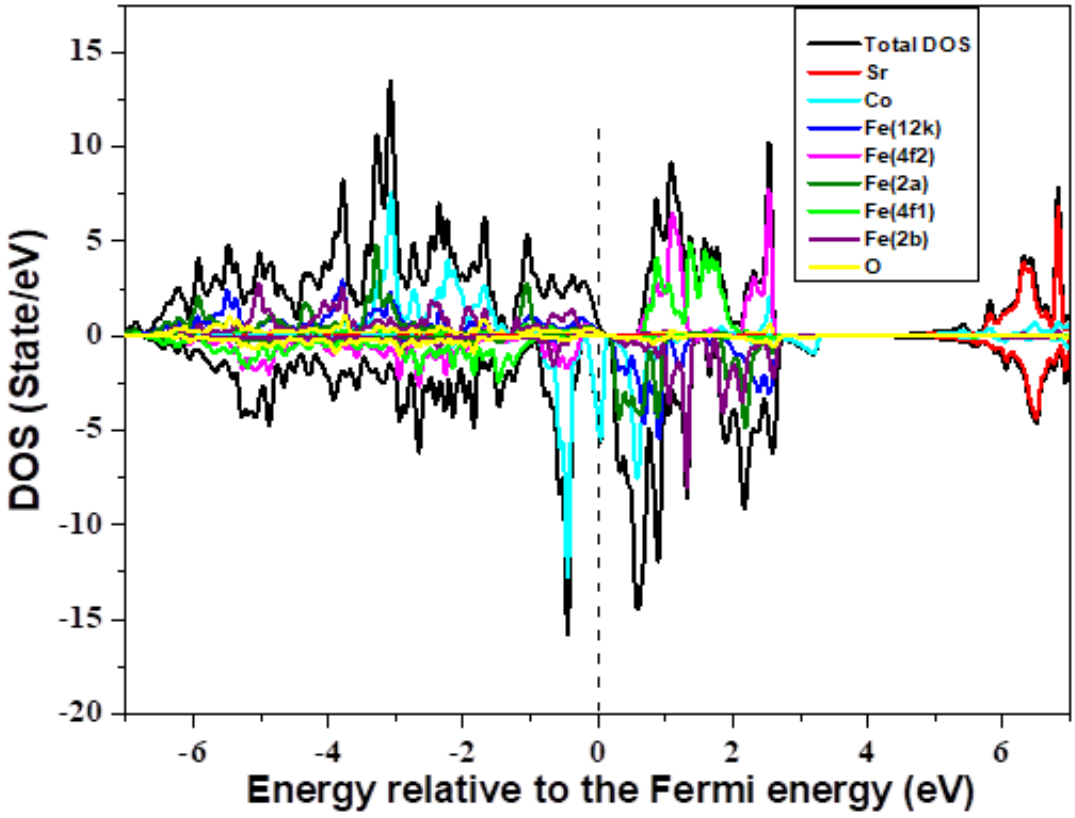

Figure 4.9: Total and Partial DOS of $Sr_{0.5}Co_{0.5}Fe_{12}O_{19}$ hexaferrite.

Wyckoff position	$SrFe_{12}O_{19}$		$Sr_{0.5}Co_{0.5}Fe_{12}O_{19}$	
	atom	Magnetic Moment	atom	Magnetic Moment
2d	Sr	-0.00136	Sr	-0.00127
			Co	2.48543
2a	Fe	3.69721	Fe	3.6868
2b	Fe	3.50097	Fe	3.49817
$4f_1$	Fe	-3.44371	Fe	-3.41603
$4f_2$	Fe	-3.41285	Fe	-3.38948
12k	Fe	3.68863	Fe	3.68868
–	Total moment	40.02642	Total moment	42.23587

Table 4.3: Local and total magnetic moments (μ_B) of ions in different Wyckoff sites of $SrFe_{12}O_{19}$ and $Sr_{0.5}Co_{0.5}Fe_{12}O_{19}$ compounds.

to 42.24 μ_B. As it is already proved by Dixit et al., the insertion of Co element in Fe ion sites allows the improvement of the coercive field instead of the saturation magnetization [208].

4.4 Conclusion

This chapter was devoted to study the possibility of improving the magnetic properties of M-type Strontium hexaferrites by using two different ways.

The first part concerned the effects of the synthesis method on the structural and magnetic properties of $SrFe_{12}O_{19}$ by using two simple, easy and low cost methods with the same conditions of calcination ; Co-precipitation and Sol-gel Auto-combustion methods.

The crystallization and purity of the prepared samples using both methods has been confirmed by the X-ray diffraction. High saturation magnetization and remanent magnetization of about 95.11 emu/g and 46.39 emu/g, respectively were obtained for the prepared nanoparticles using the sol-gel auto-combustion method. It was found that $SrFe_{12}O_{19}$ nanoparticles prepared by sol-gel auto-combustion exhibit a maximum energy product $(BH)_{max}$ of about 1.36 MG.Oe compared to the sample prepared by the co-precipitation method.

The second part concerned the substitution effects on the electronic and magnetic properties of $SrFe_{12}O_{19}$ by using Density Functional Theory. It was found that the insertion of the Cobalt element in Sr sites leads to the improvement of the magnetic moment of the

Strontium hexaferrites from 40.03 μ_B to 42.24 μ_B with a clear change of the electronic behavior to half-metallic character.

Chapter 5

Improved magnetic properties of $SrFe_{12}O_{19}/CoFe_2O_4$ nanocomposites

5.1 Introduction

Nanocomposite materials with exchange-coupling behavior have taken a great interest in permanent magnet application thanks to their improved energy product [209, 210]. In this type of magnet, a combination of the high saturation magnetization of the soft magnetic material and the large coercivity of the hard magnetic material is a key parameter to determine the magnetic properties of the composite [51, 211]. Nowadays, rare-earth based permanent magnets are well known as the strongest type of magnets. Skomski et al. predicted high magnetic energy product of such materials with exchange-spring behavior (120 MG.Oe) [37]. However, it has been a challenge to synthesize an exchange-coupled magnet with enhanced magnetic energy product.

Nanocomposite of hard $BaFe_{12}O_{19}$ and soft ferrite $Ni_{0.8}Zn_{0.2}Fe_2O_4$ have been prepared by Roy et al. by mixing the individual materials in various weight ratio and subsequent heat treatment [212]. It is shown that the energy product of ferrites magnets can be developed using the exchange spring mechanism. $BaFe_{12}O_{19}/CoFe_2O_4$ hard/soft magnetic nanocomposites were synthesized by Miao Liu et al., using one-step sol-gel method [213]. An enhancement of the $(BH)_{max}$ and the remanence were achieved in comparison to the

pure $BaFe_{12}O_{19}$ hard ferrite.

Exchange coupled nanocrystalline $Ni_{0.8}Zn_{0.2}Fe_2O_4/SrFe_{12}O_{19}$ composite fibers were synthesized by Meng et al., using the sol-gel spinning technique followed by annealing process [214]. It was found that for the annealing temperature of 900 °C, the hysteresis loop of the composite showed a single-phase-like magnetic characteristic indicating the exchange coupling between the soft and the hard phases. Hilczer et al., have prepared $SrFe_{12}O_{19}/CoFe_2O_4$ composites with a simple solid state reaction [215]. $CoFe_2O_4$ was considered as the soft magnetic phase in the composite and it was found that the composite exhibits a single-phase magnetic hysteresis for a weight ratio 4:1. Nanocomposites of $CoFe_2O_4/SrFe_{12}O_{19}$ have been synthesized by Pan et al., using the electrospinning and calcination process where the cobalt powder was used to replace traditional cobalt salt in the precursor sol-gel for the electrospinning [216]. Pang et al,. have prepared the $SrFe_{12}O_{19}$/FeCo composite through a cryogenic ball milling process with different ratio of $SrFe_{12}O_{19}$ to FeCo [217]. It was found that an effective magnetic exchange coupling between $SrFe_{12}O_{19}$ and FeCo particles could be obtained when the mass percentage of FeCo is less than 15 %. One-pot sol-gel auto-combustion and physical mixing methods were used by Tavakolinia et al. to prepare $SrFe_{12}O_{19}/Zn_{0.4}Co_{0.2}Ni_{0.4}Fe_2O_4$ hard/soft ferrite composite particles with 20, 40, 60 and 80 $wt.\%$ of soft phase [218]. The one-pot sol-gel auto-combustion method demonstrates good magnetic properties compared to the conventional physical mixing method. However, both methods exhibit the exchange coupling interaction. Almessiere et al. have evaluated the $Sr_{0.3}Ba_{0.4}Pb_{0.3}Fe_{12}O_{19}/(CuFe_2O_4)_x$ nanocomposites for permanent magnet application via one-pot citrate sol-gel synthesis route [219].

In this chapter, we report the possibility of the exchange-coupling mechanism in hard/soft $(SrFe_{12}O_{19})_{1-X}/(CoFe_2O_4)_X$ nanocomposite with small content of the soft phase that leads to the improvement of the energy product by $\approx 26\%$ compared to the parent M-type Strontium hexaferrite.

5.2 Experiments

5.2.1 Materials

$SrCl_2$ (sigma Aldrich, 99.99 %), $FeCl_3.6H_2O$ (Sigma Aldrich, 97 %), $CoCl_2.6H_2O$ (Sigma Aldrich, 97 %) and NaOH (Sigma Aldrich, 99.99 %) were used as started materials as received.

5.2.2 Preparation of $(SrFe_{12}O_{19})_{1-X}/(CoFe_2O_4)_X$ nanocomposites

$(SrFe_{12}O_{19})_{1-X}/(CoFe_2O_4)_X$ nanocomposites with different molar ratio (x=0, 0.05, 0.1, 0.2, 1) were synthesized using the standard co-precipitation route followed by physical mixing as it is described in Figure 5.1. The same synthesis protocol was used to prepare the parent $SrFe_{12}O_{19}$ and $CoFe_2O_4$ materials. Firstly, the stoichiometric amounts of metal chlorides were dissolved in 30 ml of deionized water separately to form homogeneous solutions, which were mixed and stirred at 80 °C for 30 min. Then, 1.5M of NaOH was added drop by drop until pH ≈ (11-12). Subsequently, stirring at 80°C for 1h30min was done to guarantee the homogeneity of the solutions and to mix the reagents. The precipitated was separated magnetically and washed several times with water to remove the execs of salts and dried at 80 °C overnight. The powders were calcined at 1000 °C for 6h and 800 °C for 4h under air to obtain SrFe12O19 and CoFe2O4 nanoparticles, respectively.

The synthesized M-type Strontium hexaferrites and Cobalt spinel ferrites nanoparticles were mixed physically in an agate mortar for 1h with an amplitude of 1.5. Then, calcined at 1000 °C for 3h to achieve the $(SrFe_{12}O_{19})_{1-X}/(CoFe_2O_4)_X$ nanocomposites with x=0, 0.05, 0.1, 0.2, 1 referred as SFO, CF5, CS10, CS20, CFO, respectively.

5.2.3 Characterization

The obtained samples have been studied by combining different characterization techniques to investigate their structural, microstructural and magnetic properties. X-ray

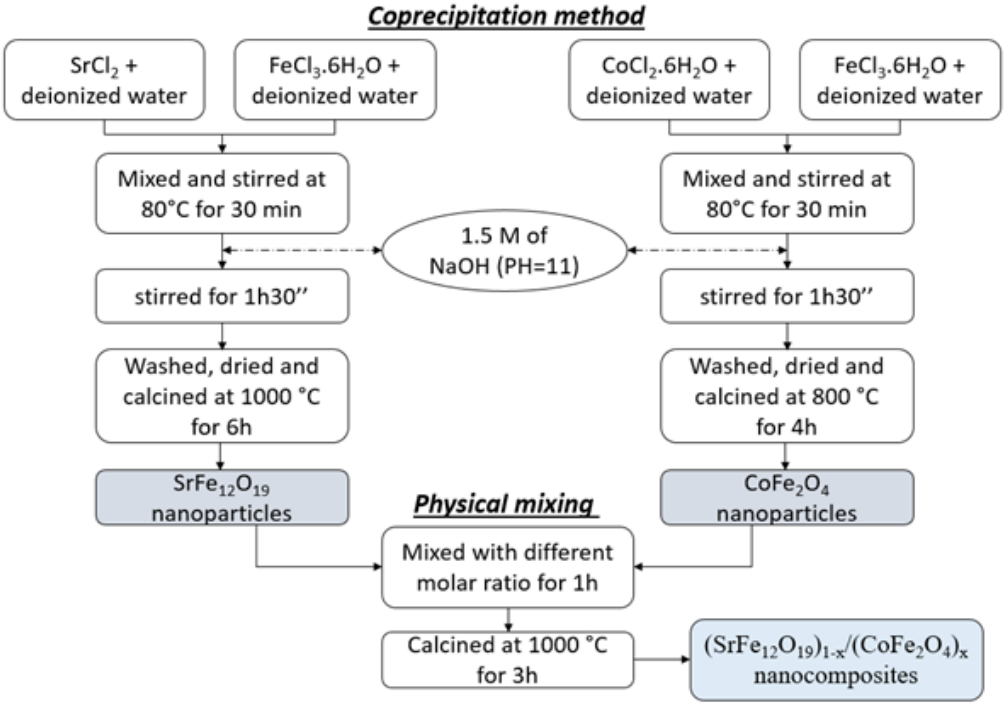

Figure 5.1: Flowchart of the synthesis process of $(SrFe_{12}O_{19})_{1-X}/(CoFe_2O_4)_X$ nanocomposites.

diffraction (XRD) was carried out to identify the prepared phases over the 2θ range from 20° to 80° with a Bruker D8 Twin-Twin powder diffractometer using Cu-K_α radiation (λ = 1.5406 $\AA$). The microstructural analysis was performed using the scanning electron microscope (FEI Quanta 450 FEG) equipped with the EDX analyzer. A Magnetic Property Measurement System (MPMS) from Quantum Design was used to assess and evaluate the magnetic properties of the prepared samples.

5.3 Results and discussion

5.3.1 Structural and microstructural analysis

5.3.1.1 X-Ray Diffraction (XRD)

The X-RD patterns of the calcined powders of the parents soft $CoFe_2O_4$ (CFO), hard $SrFe_{12}O_{19}$ (SFO) phases and the $(SrFe_{12}O_{19})_{1-X}/(CoFe_2O_4)_X$ nanocomposites (referred as CS5, CS10 and CS20 for x=0.05, 0.1, 0.2 respectively) are presented in Figure 5.2. The prepared materials exhibits sharp and well-defined peaks, indicating a high degree of

Code	Average crystallite size (nm)		Lattice parameters (Å)		
	Hard	Soft	Hard		Soft
			a=b	**c**	**a=b=c**
SFO	37.81 ± 0.15	—	5.883 ± 0.105	23.088 ± 0.218	—
CS5	39.17 ± 0.27	30.02 ± 0.23	5.884 ± 0.127	23.091 ± 0.230	8.469 ± 0.087
CS10	41.62 ± 0.21	31.87 ± 0.05	5.885 ± 0.108	23.096 ± 0.112	8.472 ± 0.106
CS20	42.27 ± 0.13	34.37 ± 0.29	5.888 ± 0.117	23.10 ± 0.098	8.481 ± 0.091
CFO	—	28.32 ± 0.09	—	—	8.46 ± 0.213

Table 5.1: The calculated average crystallite size and lattice parameters of each phase based on XRD patterns.

crystallinity of the prepared materials. The soft material (CFO) crystallizes in the face-centered cubic structure with space group N° 227 (Fd-3m) [JCPDS card N° 00-022-1086] and the (SFO) crystallizes in the hexagonal structure [JCPDS card N° 01-084-1531]. The X-ray diffraction patterns of the nanocomposites show the presence of both $CoFe_2O_4$ and $SrFe_{12}O_{19}$ phases with no peaks of any secondary phase, confirming the high purity of the prepared composites. Table 5.1 represents the calculated average crystallite size and the lattice parameters of the prepared nanoparticles from the intensities of the majority peaks of each composition. The prepared $SrFe_{12}O_{19}$ (SFO) nanoparticles have a bigger crystallite size of about 37.81 ± 0.15 nm compared to the average crystallite size of the $CoFe_2O_4$ (CFO) nanoparticles, corresponding 28.32 ± 0.09 nm. The physical mixing and the calcination at high temperature of the prepared SFO and CFO phases allowed the development of the nanocomposites without changing or affecting the structure of the parent phases but with higher crystallite size compared to the pure phases.

5.3.1.2 Scanning Electron Microscopy (SEM)

SEM images of the samples prepared in the present work are illustrated in Figure 5.3. As observed in the SEM micrographs, the host hard ferrite (SFO) shows hexagonal platelet-like morphology. It can be seen from the SEM micrographs of CS5, CS10 and CS20 nanocomposites that bigger and smaller particles are present in the nanocomposites, which could be attributed to the coexistence of both $CoFe_2O_4$ and $SrFe_{12}O_{19}$ phases, which is in good agreement with the XRD results. From the EDX analysis, no elements other than Co, Sr, Fe and O have been detected which shows that our samples have not been

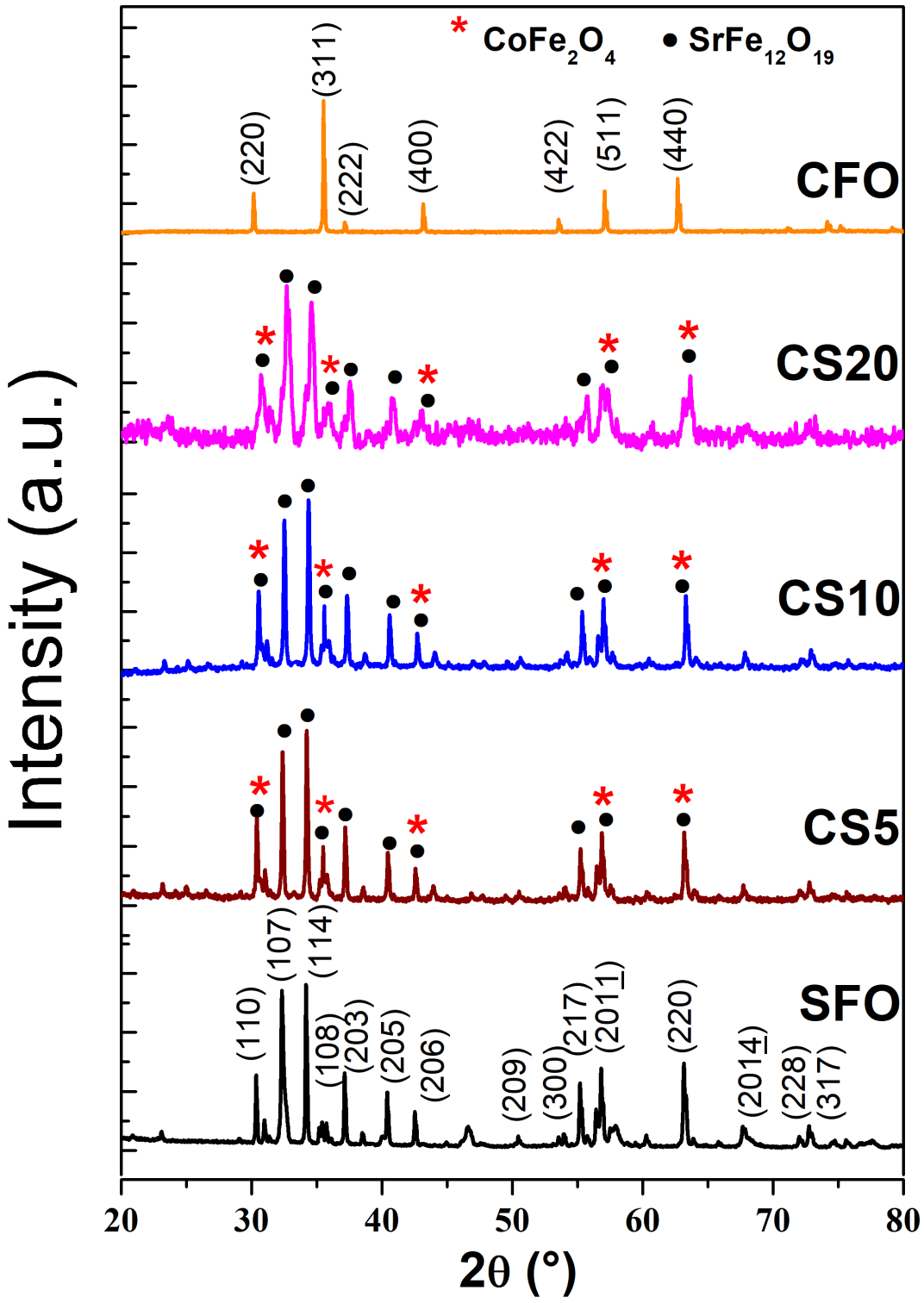

Figure 5.2: XRD patterns of $(SrFe_{12}O_{19})_{1-X}/(CoFe_2O_4)_X$ nanocomposites (referred as SFO, CS5, CS10, CS20 and CFO for x=0.0, 0.05, 0.1, 0.2, 1.0 respectively).

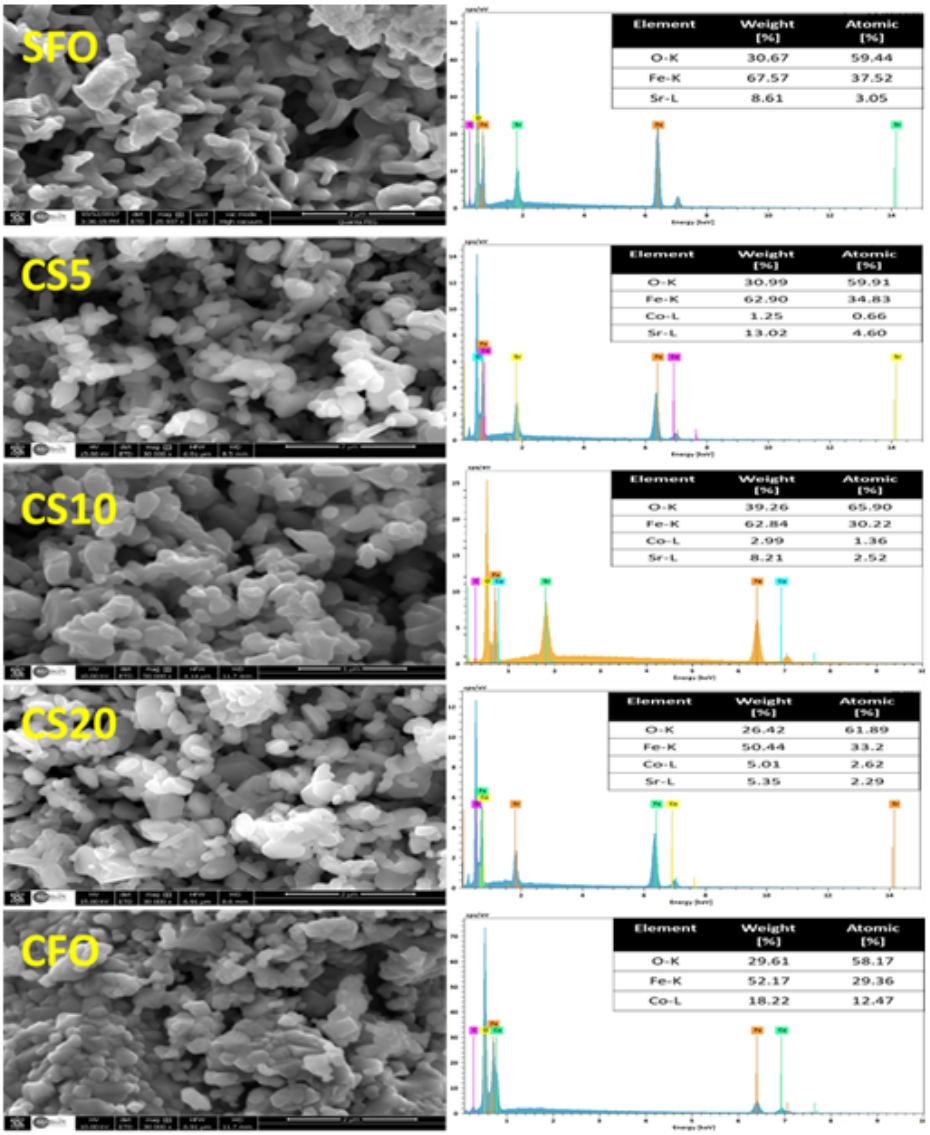

Figure 5.3: SEM and EDS analysis of $(SrFe_{12}O_{19})_{1-X}/(CoFe_2O_4)_X$ nanocomposites (referred as SFO, CS5, CS10, CS20 and CFO for x=0.0, 0.05, 0.1, 0.2, 1.0 respectively).

contaminated. The obtained atomic fractions of all elements in the samples show a good agreement with the theoretical values of the targeted chemical stoichiometry. However, a small amount of the Carbon element is detected, which corresponds to the substrate glue used during the preparation of the samples for SEM analysis.

5.3.2 Magnetic characterization

The magnetic hysteresis loops at room temperature (RT) of $SrFe_{12}O_{19}$ (SFO) and $CoFe_2O_4$ (CFO) hard/soft phases are presented in figure 5.4. As it is shown in figure 5.4

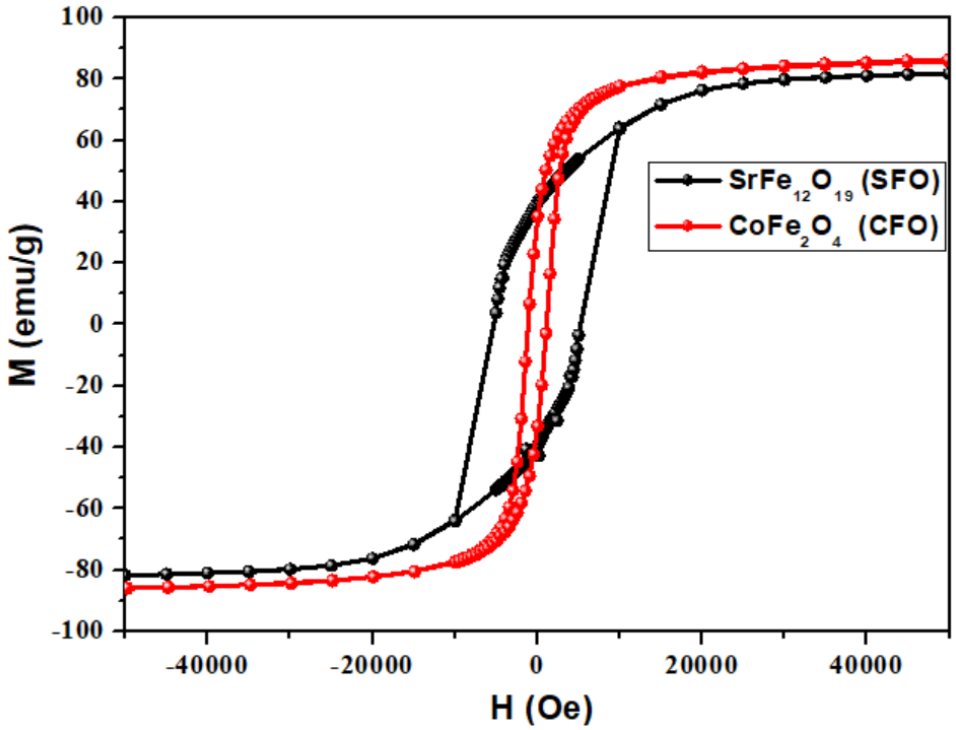

Figure 5.4: M-H hysteresis loop at 300 K of $CoFe_2O_4$ (CFO) and $SrFe_{12}O_{19}$ (SFO).

Code	$Ms(emu/g)$	$Mr(emu/g)$	$Hc(KOe)$	$(BH)_{max}(MG.Oe)$
SFO	81.79	39.74	5.37	1.13
CS5	93.77	45.34	5.50	1.43
CS10	84.71	40.95	5.40	1.2
CS20	72.96	34.91	5.43	0.89
CFO	86.26	33.25	1.21	0.45

Table 5.2: Magnetic parameters at Room temperature of $(SrFe_{12}O_{19})_{1-X}/(CoFe_2O_4)_X$ nanocomposites with x=0.0, 0.05, 0.1, 0.2, 1.

and table 5.2, the hard magnetic phase $SrFe_{12}O_{19}$ (SFO) has high coercivity, saturation and remanent magnetization of about 5.37 kOe, 81.79 emu/g and 39.74 emu/g, respectively. Abraime et al., have studied the magnetic properties of $SrFe_{12}O_{19}$ nano-powder synthetized using sol-gel auto combustion with different temperature of calcination [220]. It was found that the hard magnetic material annealed at 1000 °C have a saturation magnetization of 73.54 emu/g, remanent magnetization of 36.289 emu/g and a coercivity of about 5 kOe. $SrFe_{12}O_{19}$ Nanocrystallites have been synthesized by Eikeland et al., using a conventional sol-gel (CSG) and a modified sol-gel (MSG) synthesis route. An enhancement of the magnetic properties was obtained using a modified sol-gel process [199].

The synthesized $CoFe_2O_4$ (CFO) soft magnetic phase exhibits a small coercivity of about 1.08 kOe and high saturation magnetization of about 86.26 emu/g compared to the strontium hexaferrites nanoparticles. A slight increase of the magnetic properties compared to our previous synthetized $CoFe_2O_4$ nanoparticles with a low annealing temperature [144]. The size effects on the magnetic properties of $CoFe_2O_4$ nanoparticles have been studied theoretically using a combined density functional theory and Monte Carlo simulation in our previous work, it was found that cobalt spinel ferrites exhibits a large saturation magnetization around 98 emu/g for particle size of about 29 nm. This difference between the theoretical and experimental results can be explained by the homogenous of the cations distribution, which can not be controlled by the coprecipitation synthesis route [92].

The magnetic hysteresis loops at room temperature of $(SrFe_{12}O_{19})_{1-X}/(CoFe_2O_4)_X$ with x=0.05, 0.1, 0.2 are presented in figure 5.5. In general, the magnetic properties of hard/soft composite material are governed by the exchange-coupling interaction between soft/hard phases and the dipolar interaction between soft/soft phases and hard/hard phases.

According to previous studies [221, 222], the dipolar interaction is a long range phenomenon. Thus, it can be dominated by the exchange-coupling interaction for lower content of the soft phase. However, the influence of the dipolar interaction should be considered with any further increase of the soft phase in the composite which lead to decrease the magnetic properties. If the dipolar interaction is neglected, the exchange-coupling interaction takes place for the determination of the magnetic properties of composite materials [223]. Figure 5.5 shows a good single magnetic phase behavior for all synthesized nanocomposites indicating that the reversal magnetization was achieved in one step and suggesting the presence of the exchange-coupling interaction between the soft and hard magnetic phases.

To better illustrate the magnetic single-phase, we plotted in figure 5.6 the (dM/dH) as a function of the applied magnetic field which shows single peaks for all nanocomposites. Generally, a single peak of the dM/dH versus the applied magnetic field can be consid-

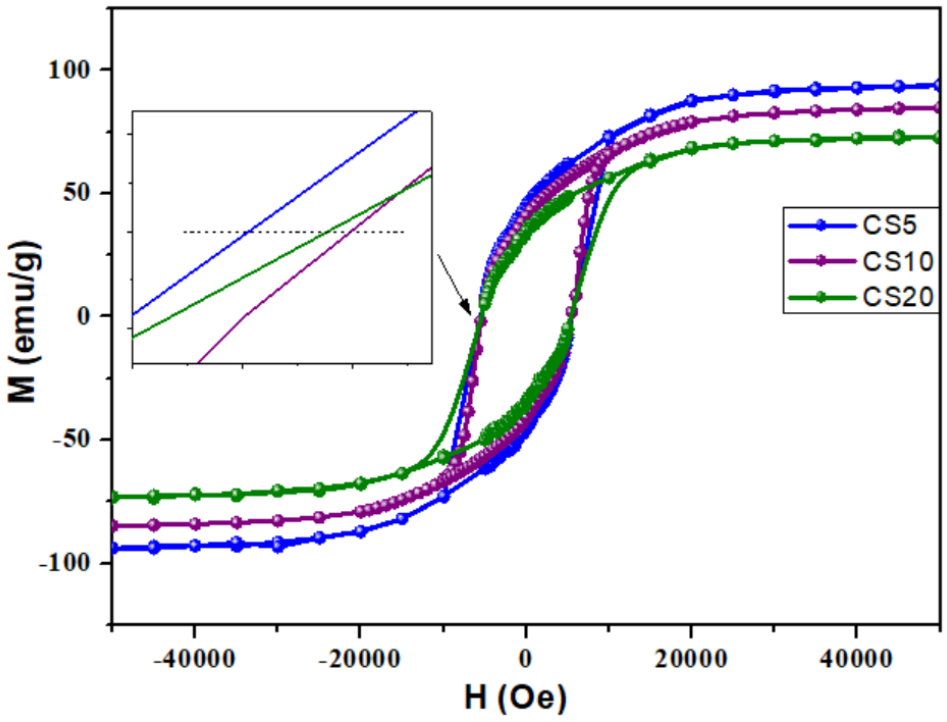

Figure 5.5: M-H hysteresis loop at 300 K of $(SrFe_{12}O_{19})_{1-X}/(CoFe_2O_4)_X$ nanocomposites with x= 0.05, 0.1, 0.2.

ered as an important indicator of the presence of the exchange coupling phenomena in nanocomposite magnets [224].

Figure 5.7 presents the dependence of the saturation magnetization (Ms) and coercivity (Hc) to the content of the $CoFe_2O_4$ soft phase in the prepared composite extracted from the magnetic hysteresis loops (M-H) at room temperature . We observed from figure 5.7 and table 5.2 a slight increase of the coercivity (Hc) from 5.37 kOe for the parent hard ferrite $SrFe_{12}O_{19}$ to 5.5 kOe for $(SrFe_{12}O_{19})_{0.95}/(CoFe_2O_4)_{0.05}$ nanocomposite.

The saturation magnetization (Ms) for composite material without exchange-coupling behavior can be calculated within the following formula [225]:

$$Ms = x \times M_{soft} + (1 - x) \times M_{hard} \tag{5.1}$$

Where M_{soft}, M_{hard} and x correspond to the saturation magnetization of soft and hard phases and the content of the soft phase in the composite, respectively.

According to formula (5.1), the calculated Ms were found to be 82.03 emu/g, 82.24 emu/g and 82.68 emu/g for CS5, CS10 and CS20, respectively. The measured values of

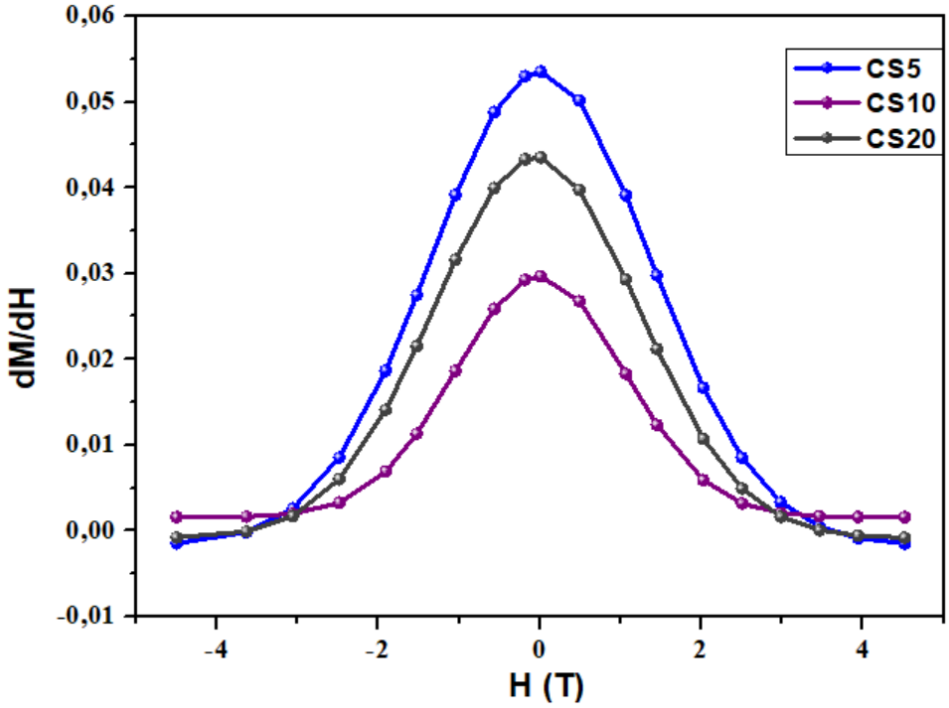

Figure 5.6: dM/dH plot as a function of the applied magnetic field.

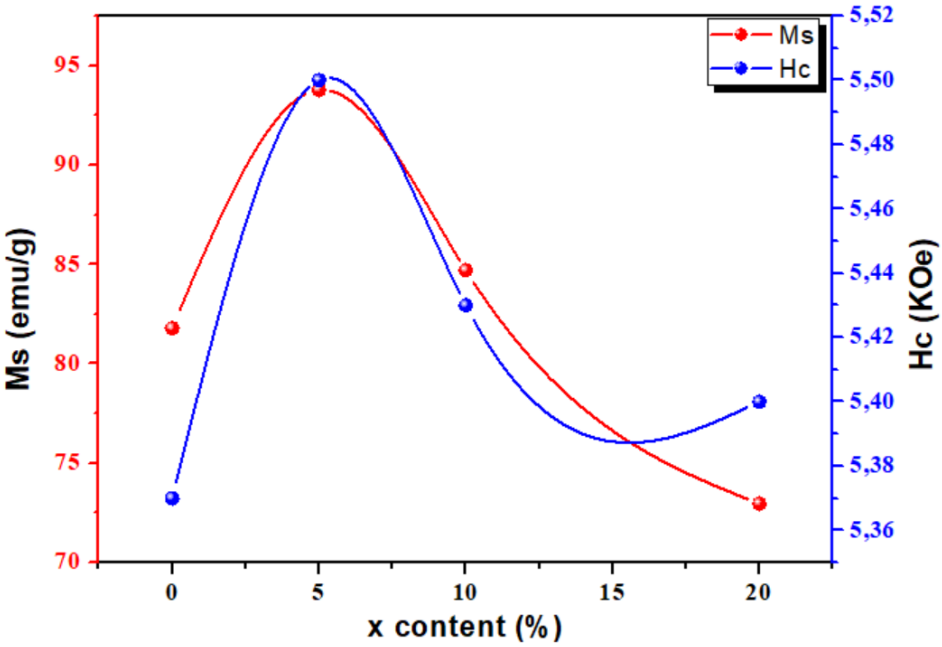

Figure 5.7: Dependence of the Saturation magnetization (Ms) and coercivity (Hc) with the x content of the $CoFe_2O_4$ phase.

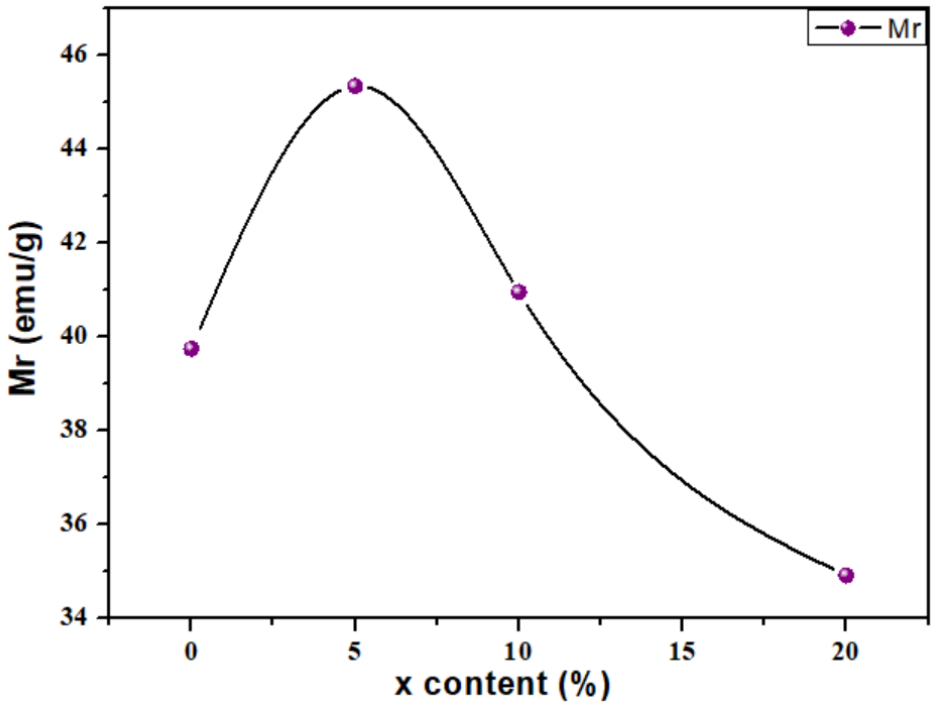

Figure 5.8: Dependence of the Remanent magnetization (Mr) with the x content of the $CoFe_2O_4$ phase.

the saturation magnetization of the synthesized nanocomposites are listed in table 5.2. The obtained values of the samples corresponding to CS5 and CS10 are much higher than the calculated ones from formula (5.1), which can be explained by the dominance of the exchange-coupling interaction between the soft and the hard magnetic phases. As the content of the soft magnetic phase increases, the magnetic parameters show a decrease due to the enhancement of the dipolar interaction between the soft/soft magnetic phases.

The evolution of the remanent magnetization as a function of the x content of the $CoFe_2O_4$ phase is presented in figure 5.8. A similar trend to the saturation magnetization was observed for the remanent magnetization indicating an improvement is shown from 39.74 emu/g for the parent $SrFe_{12}O_{19}$ compound to 45.34 emu/g for $(SrFe_{12}O_{19})_{0.95}/(CoFe_2O_4)_{0.05}$ nanocomposite.

To figure out the efficiency of the synthesized materials for permanent magnet applications, the magnetic energy product is calculated from the second quadrant of the B-H hysteresis loop [2]. The maximum value of the magnetic energy product $(BH)_{max}$ as a function of the soft phase content is presented in figure 5.9. It can be seen from the figure and table 5.2 that the $(BH)_{max}$ of $(SrFe_{12}O_{19})_{0.95}/(CoFe_2O_4)_{0.05}$ nanocomposite

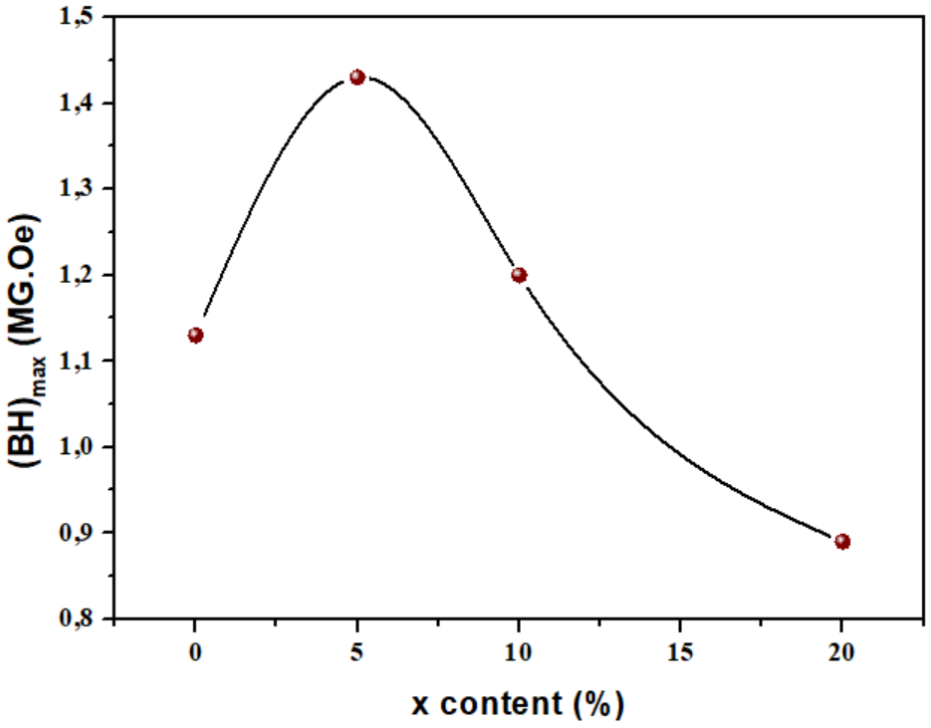

Figure 5.9: Calculated maximum energy product $(BH)_{max}$ as a function of the x content of the soft phase.

shows an improvement of about 26.5 % compared to the parent $SrFe_{12}O_{19}$ hexaferrite nanoparticles. Haibo Yang et al., synthesized $BaFe_{12}O_{19}/CoFe_2O_4$ nanocomposites using the microwave sintering method and found an improvement of 32.20 % with 20 $wt.\%$ of $CoFe_2O_4$ [226]. An enhancement of the maximum energy product of 10.5 % was shown for $SrFe_{10}Al_2O_{19}/Co_{0.8}Ni_{0.2}Fe_2O_4$ nanocomposite with 15 $wt.\%$ of the soft phase prepared by one pot sol-gel auto-combustion method [227].

5.4 Conclusion

To summarize, this chapter was devoted to the preparation of $(SrFe_{12}O_{19})_{1-X}/(CoFe_2O_4)_X$ Nanocomposites of hard/soft phases with different molar ratio (x= 0.05, 0.10, 0.20) using standard co-precipitation method followed by a physical mixing. $CoFe_2O_4$ material was used as a soft magnetic material when the effects of its concentration on the structural, microstructural and the magnetic properties of the obtained nanocomposites were performed through different characterization techniques. The X-ray diffraction (XRD) showed the

existence of mixed phases of the spinel ferrite and the M-type hexaferrite. The Scanning Electron Microscopy (SEM) was used to perform the microstructural characterization. The superconducting quantum interference device magnetometer (SQUID) was used to investigate the magnetic properties of nanocomposites. The magnetic hysteresis loops of all samples showed a good single-phase magnetic behaviour, which proves the exchange-spring interaction between soft magnetic phase $CoFe_2O_4$ and the hard magnetic phase $SrFe_{12}O_{19}$. Moreover, The $(SrFe_{12}O_{19})_{0.95}/(CoFe_2O_4)_{0.05}$ nanocomposite showed the highest values of the saturation magnetization, remanent magnetization and coercivity. An enhancement of the maximum energy product is observed for $(SrFe_{12}O_{19})_{0.95}/(CoFe_2O_4)_{0.05}$ by $\approx 26.5\%$ compared to the $SrFe_{12}O_{19}$ hexaferrite.

General conclusion

Cobalt spinel ferrites "$CoFe_2O_4$" and M-type Strontium hexaferrites "$SrFe_{12}O_{19}$" have been considered as promising candidates to replace rare-earth-based magnets and intermetallic alloys magnets in low-energy permanent magnets applications. These materials, as hard magnetic materials, have been the subject of numerous studies in physics and materials science. The challenge for ferrites magnets is that they do not simultaneously exhibit high magnetization and high coercivity. High coercivity can be achieved by either the materials intrinsic high magneto-crystalline anisotropy or fine particle/grain size. While high remanent magnetization requires high saturation magnetization and a high degree of alignment of the grains along the magnetic easy axis.

The main objective of this thesis was the combination of theoretical and experimental studies on the structural, microstructural, electronic and magnetic properties of $CoFe_2O_4$ and $SrFe_{12}O_{19}$ materials. We have sought to understand the origin of the magnetic properties of those materials by studying their structural, electronic and magnetic properties using different numerical tools such as density functional theory, mean-field approximation and Monte Carlo simulation. Furthermore, we have looked for easy and low-cost preparation of ferrites and nanoferrites with enhanced magnetic properties by studying either the effects of the synthesis methods or the possibility of the exchange-coupling mechanism in hard/soft nanocomposites.

Indeed, We started our thesis work by a combination of theoretical and experimental study of the magnetic properties of bulk $CoFe_2O_4$. A high saturation magnetization (Ms) was shown for bulk Cobalt spinel ferrites. However, the bulk system exhibits a weak coercivity (Hc) leading to a low maximum energy product $(BH)_{max}$ of about 0.02 MG.Oe from the experimental measurements and 0.07 MG.Oe from Monte Carlo simulation. To overcome this weakness in the coercivity, We have studied the size-effects on the magnetic properties of "$CoFe_2O_4$" cubic-shaped single nanoparticles using Monte Carlo simulation. We found that the saturation and remanent magnetization increased with the increase of the particles size towards bulk values. Furthermore, the single-domain size limit is observed for a size of about 21 nm, where the performance of the cubic-shaped

nanoparticles, in term of the $(BH)_{max}$, achieved its maximum value of about 2.83 MG.Oe at room temperature.

On the other hand, we have explored the structural, microstructural and the electronic properties of $SrFe_{12}O_{19}$ in order to improve its magnetic properties. The effects of the synthesis method on the structural and magnetic properties of $SrFe_{12}O_{19}$ was investigated by considering two simple, easy and low-cost methods, i.e; Co-precipitation and Sol-gel Auto-combustion methods, with the same conditions of calcination. The crystalline purity of the obtained samples has been confirmed by the X-ray with a crystallite size of about 37.8 nm for the synthesized nanoparticles using co-precipitation method while the sol-gel auto-combustion route gives rise to bigger nanoparticles with an average crystallite size of about 85.4 nm. High saturation magnetization and remanent magnetization of about 95.11 emu/g and 46.39 emu/g, respectively were obtained for the prepared nanoparticles using the sol-gel auto-combustion method. Furthermore, it was shown that $SrFe_{12}O_{19}$ nanoparticles prepared by sol-gel auto-combustion exhibit a maximum energy product $(BH)_{max}$ of about 1.36 MG.Oe compared to the sample prepared by the co-precipitation method (1.13 MG.Oe). A theoretical work based on DFT was performed to study the substitution effects on the electronic and magnetic properties of $SrFe_{12}O_{19}$. It was found that the insertion of the Cobalt element in Sr sites leads to the improvement of the magnetic moment of the Strontium hexaferrites from 40.03 μ_B to 42.24 μ_B with a clear change of the electronic behavior to a half-metallic character.

The last chapter of this thesis concerns the preparation of $(SrFe_{12}O_{19})_{1-X}/(CoFe_2O_4)_X$ nanocomposites of with various molar ratio (x= 0.05, 0.10, 0.20), where $CoFe_2O_4$ material was used as a soft magnetic material. The parent spinel ferrites and M-type hexaferrites were prepared using the conventional coprecipitation method followed by a physical mixing. The X-ray diffraction (XRD) showed the existence of mixed phases of the spinel ferrite and the M-type hexaferrite which has been confirmed by the images of the Scanning Electron Microscopy (SEM). The magnetic hysteresis loops of all samples showed a good single-phase magnetic behaviour, which proves the exchange-spring interaction between the soft magnetic phase $CoFe_2O_4$ and the hard magnetic phase $SrFe_{12}O_{19}$. More-

over, The $(SrFe_{12}O_{19})_{0.95}/(CoFe_2O_4)_{0.05}$ nanocomposite showed the highest values of the saturation magnetization, remanent magnetization and coercivity of about 93.77 emu/g, 45.34 emu/g and 5.50 KOe, respectively. An enhancement of the maximum energy product is observed for $(SrFe_{12}O_{19})_{0.95}/(CoFe_2O_4)_{0.05}$ by $\approx 26.5\%$ compared to the $SrFe_{12}O_{19}$ hexaferrite.

We believe that a research work never ends, for this reason we intend to complete our thesis work by :

- Introduction of other parameters to our Ising model such as the inter-particles interactions and the orientation of the nanoparticles in order to better understand the magnetic properties of the cubic-shaped nanoparticles.

- modeling and simulation of other forms of nanoparticles such as octahedrons and spheres using density functional theory and Monte Carlo simulation.

Bibliography

[1] J. M. D. Coey, "Magnetism and magnetic materials," Cambridge University Press, New York, NY, 2010.

[2] S. Moosavi, A. Djerdir, Y. Amirat, and D. Khaburi, "Demagnetization fault diagnosis in permanent magnet synchronous motors: A review of the state-of-the-art," *Journal of Magnetism and Magnetic Materials*, vol. 391, pp. 203 – 212, 2015.

[3] S. Hirosawa, "Preface to the viewpoint set on: Permanent magnets and underlining material science," *Scripta Materialia*, vol. 154, pp. 245 – 247, 2018.

[4] J. Coey, "Perspective and prospects for rare earth permanent magnets," *Engineering*, vol. 6, no. 2, pp. 119 – 131, 2020.

[5] K. Skokov and O. Gutfleisch, "Heavy rare earth free, free rare earth and rare earth free magnets - vision and reality," *Scripta Materialia*, vol. 154, pp. 289 – 294, 2018.

[6] D. Li, Y. Li, D. Pan, Z. Zhang, and C.-J. Choi, "Prospect and status of iron-based rare-earth-free permanent magnetic materials," *Journal of Magnetism and Magnetic Materials*, vol. 469, pp. 535–544, 2019.

[7] J. Mohapatra and J. Liu, "Rare-earth-free permanent magnets: The past and future," *Handbook of Magnetic Materials*, 2018.

[8] R. C. Pullar, "Hexagonal ferrites: A review of the synthesis, properties and applications of hexaferrite ceramics," *Progress in Materials Science*, vol. 57, no. 7, pp. 1191–1334, 2012.

[9] V. K. Chakradhary, A. Ansari, and M. J. Akhtar, "Design, synthesis, and testing of high coercivity cobalt doped nickel ferrite nanoparticles for magnetic applications," *Journal of Magnetism and Magnetic Materials*, vol. 469, pp. 674 – 680, 2019.

[10] M. De Gennaro, J. Jürgens, A. Zanon, J. Gragger, E. Schlemmer, A. Fricassè, L. Marengo, B. Ponick, E. T. Olabarri, J. Kinder, A. Cavallini, P. Mancinelli, M. Hernandez, and M. Messagie, "Designing, prototyping and testing of a ferrite permanent magnet assisted synchronous reluctance machine for hybrid and electric vehicles applications," *Sustainable Energy Technologies and Assessments*, vol. 31, pp. 86 – 101, 2019.

[11] C.-C. Huang, A.-H. Jiang, C.-H. Liou, Y.-C. Wang, C.-P. Lee, T.-Y. Hung, C.-C. Shaw, Y.-H. Hung, M.-F. Kuo, and C.-H. Cheng, "Magnetic property enhancement of cobalt-free m-type strontium hexagonal ferrites by caco3 and sio2 addition," *Intermetallics*, vol. 89, pp. 111 – 117, 2017.

[12] A. Kolhatkar, A. Jamison, D. Litvinov, R. Willson, and T. Lee, "Tuning the magnetic properties of nanoparticles," *International Journal of Molecular Sciences*, vol. 14, no. 8, pp. 15977–16009, 2013.

[13] L. Néel, "Some new results on antiferromagnetism and ferromagnetism," *Reviews of Modern Physics*, vol. 25, no. 1, pp. 58–63, 1953.

[14] C. Kittel and J. Galt, "Ferromagnetic domain theory," vol. 3 of *Solid State Physics*, pp. 437 – 564, Academic Press, 1956.

[15] P. V. Powar, "Development status in the meadow of nanostructure magnetic drug delivery system and its promising applications," *International Journal of Pharmacy and Pharmaceutical Sciences*, vol. 9, pp. 10–17, Dec. 2017.

[16] D. Jiles and D. Atherton, "Theory of ferromagnetic hysteresis," *Journal of Magnetism and Magnetic Materials*, vol. 61, no. 1, pp. 48 – 60, 1986.

[17] J. A. Ewing, "On the production of transient electric currents in iron and steel conductors by twisting them when magnetised or by magnetising them when twisted," *Royal Society*, vol. 33, pp. 21–23, Dec. 1882.

[18] D. Jiles and D. Atherton, "Ferromagnetic hysteresis," *IEEE Transactions on Magnetics*, vol. 19, no. 5, pp. 2183–2185, 1983.

[19] A. Visintin, *Differential Models of Hysteresis*, vol. 111. Springer-Verlag Berlin Heidelberg, 1994.

[20] R. Zhao, X. Jiang, H. Xu, Q. Yan, and Y. Wang, "An iron loss estimation method based on dual current-ripple envelopes for three-phase two-level grid-connected converters," *IEEE Access*, vol. 7, pp. 159994–160003, 2019.

[21] E. Stoner and E. Wohlfarth, "A mechanism of magnetic hysteresis in heterogeneous alloys," *IEEE Transactions on Magnetics*, vol. 27, no. 4, pp. 3475–3518, 1991.

[22] A. Inoue and F. Kong, "Soft magnetic materials," in *Reference Module in Materials Science and Materials Engineering*, Elsevier, 2020.

[23] F. Fiorillo, G. Bertotti, C. Appino, and M. Pasquale, "Soft magnetic materials," *Wiley Encyclopedia of Electrical and Electronics Engineering*, 11 2016.

[24] E. Pellicer, M. Cabo, A. Lopez-Ortega, M. Estrader, S. Surinach, M. Baro, J. Nogués, and J. Sort, *Oxide-Matrix Based Nanocomposite Materials for Advanced Magnetic and Optical Functionalities*. 04 2011.

[25] A. Hamler, V. Goričan, B. Šuštaršič, and A. Sirc, "The use of soft magnetic composite materials in synchronous electric motor," *Journal of Magnetism and Magnetic Materials*, vol. 304, no. 2, pp. e816 – e819, 2006.

[26] T. Lamichhane, L. Sethuraman, A. Dalagan, H. Wang, J. Keller, and M. Paranthaman, "Additive manufacturing of soft magnets for electrical machines—a review," *Materials Today Physics*, vol. 15, p. 100255, 2020.

[27] E. Wohlfarth, "Hard magnetic materials," *Advances in Physics*, vol. 8, no. 30, pp. 87–224, 1959.

[28] K. H. J. Buschow, "New developments in hard magnetic materials," *Reports on Progress in Physics*, vol. 54, pp. 1123–1213, sep 1991.

[29] H. R. Kirchmayr, "Permanent magnets and hard magnetic materials," *Journal of Physics D: Applied Physics*, vol. 29, pp. 2763–2778, nov 1996.

[30] J. M. D. Coey, "Hard magnetic materials: A perspective," *IEEE Transactions on Magnetics*, vol. 47, no. 12, pp. 4671–4681, 2011.

[31] J. M. D. Coey, *Applications of hard magnets*, p. 464–493. Cambridge University Press, 2010.

[32] H. Sung and C. Rudowicz, "Physics behind the magnetic hysteresis loop—a survey of misconceptions in magnetism literature," *Journal of Magnetism and Magnetic Materials*, vol. 260, no. 1, pp. 250 – 260, 2003.

[33] H. Stadelmaier and E.-T. Henig, "Graphical methods for determining the maximum energy product of magnets," *Journal of Magnetism and Magnetic Materials*, vol. 88, no. 3, pp. 365 – 368, 1990.

[34] G. Fridgen, A. Michaelis, M. Rinck, M. Schöpf, and M. Weibelzahl, "The search for the perfect match: Aligning power-trading products to the energy transition," *Energy Policy*, vol. 144, p. 111523, 2020.

[35] R. Jha, *Combined Computational-Experimental Design of High-Temperature, High-Intensity Permanent Magnetic Alloys with Minimal Addition of Rare-Earth Elements*. PhD thesis, 05 2016.

[36] J. Park, Y.-K. Hong, S.-G. Kim, S. Kim, L. S. Liyanage, J. Lee, W. Lee, G. S. Abo, K.-H. Hur, and S.-Y. An, "Maximum energy product at elevated temperatures for hexagonal strontium ferrite (srfe12o19) magnet," *Journal of Magnetism and Magnetic Materials*, vol. 355, pp. 1 – 6, 2014.

[37] R. Skomski and J. Coey, "Giant energy product in nanostructured two-phase magnets," *Physical Review B*, vol. 48, no. 21, pp. 15812–15816, 1993.

[38] A. Pathak, D. Paudyal, Y. Mudryk, J. Gschneidner, K.A., and V. Pecharsky, "Tunable magnetism and structural transformations in mixed light- and heavy-lanthanide dialuminides," *Physical Review B*, vol. 94, no. 22, 2016.

[39] B. Balamurugan, D. Sellmyer, G. Hadjipanayis, and R. Skomski, "Prospects for nanoparticle-based permanent magnets," *Scripta Materialia*, vol. 67, no. 6, pp. 542–547, 2012.

[40] H. Zeng, J. Li, J. Liu, Z. Wang, and S. Sun, "Exchange-coupled nanocomposite magnets by nanoparticle self-assembly," *Nature*, vol. 420, no. 6914, pp. 395–398, 2002.

[41] R. J. Elliott and F. A. Wedgwood, "The temperature dependence of magnetic ordering in the heavy rare earth metals," *Proceedings of the Physical Society*, vol. 84, pp. 63–75, jul 1964.

[42] H. Park, A. J. Millis, and C. A. Marianetti, "Site-selective mott transition in rare-earth-element nickelates," *Phys. Rev. Lett.*, vol. 109, p. 156402, Oct 2012.

[43] H.-S. Li and J. Coey, "Magnetic properties of ternary rare-earth transition-metal compounds," *Handbook of Magnetic Materials*, vol. 28, pp. 87–196, 2019.

[44] Z. Hammache, S. Bensaadi, Y. Berbar, N. Audebrand, A. Szymczyk, and M. Amara, "Recovery of rare earth elements from electronic waste by diffusion dialysis," *Separation and Purification Technology*, vol. 254, 2021.

[45] Q. Zhu, Y. Lin, Z. Ma, W. Li, Z. Song, B. Zheng, C. Xu, L. Yang, and H. Li, "Coercivity enhancement of sintered ce-substituted nd-fe-b magnets by grain boundary diffusion process of tb," *Journal of Magnetism and Magnetic Materials*, vol. 515, 2020.

[46] I. Makarova, J. Ryl, Z. Sun, I. Kurilo, K. Górnicka, M. Laatikainen, and E. Repo, "One-step recovery of ree oxalates in electro-leaching of spent ndfeb magnets," *Separation and Purification Technology*, vol. 251, 2020.

[47] F. Chen, "Recent progress of grain boundary diffusion process of nd-fe-b magnets," *Journal of Magnetism and Magnetic Materials*, vol. 514, 2020.

[48] Q. Chen, S. Ni, G. Ai, T. Zhang, and X. Sun, "A recovery strategy of sm, co for waste smco magnets by fatty acid based ionic liquids," *Minerals Engineering*, vol. 158, 2020.

[49] B. Das, R. Choudhary, R. Skomski, B. Balasubramanian, A. Pathak, D. Paudyal, and D. Sellmyer, "Anisotropy and orbital moment in sm-co permanent magnets," *Physical Review B*, vol. 100, no. 2, 2019.

[50] B. Cui, X. Liu, A. H. King, G. Ouyang, C. I. Nlebedim, and J. Cui, "Overcoming mechanical fragility in sm-co permanent magnet materials," *Acta Materialia*, vol. 196, pp. 528 – 538, 2020.

[51] L. Lewis and F. Jimenez-Villacorta, "Perspectives on permanent magnetic materials for energy conversion and power generation," *Metallurgical and Materials Transactions A*, vol. 44-Suppl., p. 2, 01 2013.

[52] G. Hoffer and K. Strnat, "Magnetocrystalline anisotropy of yco5and y2c017," *IEEE Transactions on Magnetics*, vol. 2, no. 3, pp. 487–489, 1966.

[53] K. Strnat, G. Hoffer, J. Olson, W. Ostertag, and J. Becker, "A family of new cobalt-base permanent magnet materials," *Journal of Applied Physics*, vol. 38, no. 3, pp. 1001–1002, 1967.

[54] J. Croat, "Crystallization and magnetic properties of melt-spun neodymium-iron alloys," *Journal of Magnetism and Magnetic Materials*, vol. 24, no. 2, pp. 125–131, 1981.

[55] M. Sagawa, W. Yamagishi, and Z. Henmi, "Temperature-sensitive nd-co compounds produced by powder metallurgy," *Journal of Applied Physics*, vol. 52, no. 3, pp. 2520–2522, 1981.

[56] X. Song, X. Zhou, T. Yuan, J. Wang, M. Yue, and T. Ma, "Role of nanoscale interfacial defects on magnetic properties of the 2:17-type sm–co permanent magnets," *Journal of Alloys and Compounds*, vol. 816, p. 152620, 2020.

[57] S. Wang, Y. Fang, C. Wang, L. Wang, M. Zhu, W. Li, and G. C. Hadjipanayis, "Dependence of macromagnetic properties on the microstructure in high-performance sm2co17-type permanent magnets," *Journal of Magnetism and Magnetic Materials*, vol. 510, p. 166942, 2020.

[58] S. Wang, Y. Fang, K. Song, X. Zhu, L. Wang, W. Sun, W. Pan, M. Zhu, and W. Li, "Optimization of both coercivity and knee-point magnetic field of sm2co17-type magnets via solid solution process," *Journal of Rare Earths*, 2019.

[59] Z. Guo, W. Pan, and W. Li, "Sm(co, fe, cu, zr)z sintered magnets with a maximum operating temperature of 500°c," *Journal of Magnetism and Magnetic Materials*, vol. 303, no. 2, pp. e396 – e401, 2006.

[60] S. Liu, "Sm-co high-temperature permanent magnet materials," *Chinese Physics B*, vol. 28, no. 1, 2019.

[61] J. Croat, "Magnetic hardening of pr-fe and nd-fe alloys by melt-spinning," *Journal of Applied Physics*, vol. 53, no. 4, pp. 3161–3169, 1982.

[62] J. Herbst, J. Croat, F. Pinkerton, and W. Yelon, "Relationships between crystal structure and magnetic properties in nd2fe14b," *Physical Review B*, vol. 29, no. 7, pp. 4176–4178, 1984.

[63] M. Sagawa, S. Fujimura, H. Yamamoto, and Y. Matsuura, "Permanent magnet materials based on the rare earth-iron-boron tetragonal compounds (invited)," *IEEE Transactions on Magnetics*, vol. 20, no. 5, pp. 1584–1589, 1984.

[64] M. Sagawa, S. Fujimura, H. Yamamoto, Y. Matsuura, and K. Hiraga, "Permanent magnet materials based on the rare earth-iron-boron tetragonal compounds.," p. 64, 1984.

[65] M. Sagawa, S. Fujimura, H. Yamamoto, Y. Matsuura, and K. Hiraga, "Permanent magnet materials based on the rare earth-iron-boron tetragonal compounds.," *IEEE Transactions on Magnetics*, vol. MAG-20, no. 5, 1984.

[66] H. Onodera, Y. Yamaguchi, H. Yamamoto, M. Sagawa, Y. Matsuura, and H. Yamamoto, "Magnetic properties of a new permanent magnet based on a nd-fe-b compound (neomax). i. mössbauer study," *Journal of Magnetism and Magnetic Materials*, vol. 46, no. 1-2, pp. 151–156, 1984.

[67] B. Zhou, Z. Li, and C. Chen, "Global potential of rare earth resources and rare earth demand from clean technologies," *Minerals*, vol. 7, no. 11, 2017.

[68] R. McCurrie, "Chapter 3 the structure and properties of alnico permanent magnet alloys," vol. 3 of *Handbook of Ferromagnetic Materials*, pp. 107 – 188, Elsevier, 1982.

[69] Z. Ahmad, Z. Liu, and A. ul Haq, "Synthesis, magnetic and microstructural properties of alnico magnets with additives," *Journal of Magnetism and Magnetic Materials*, vol. 428, pp. 125 – 131, 2017.

[70] Y. Iwama, "Magnetic properties of alnico-type magnet alloys at elevated temperatures," *Transactions of the Japan Institute of Metals*, vol. 8, no. 1, pp. 18–25, 1967.

[71] C. Zhang, Y. Li, X.-H. Han, S. long Du, J. bing Sun, and Y. Zhang, "Structure and magnetic properties of alnico ribbons," *Journal of Magnetism and Magnetic Materials*, vol. 451, pp. 200 – 207, 2018.

[72] S. Collocott, "Magnetic materials: Domestic applications," in *Encyclopedia of Materials: Science and Technology* (K. J. Buschow, R. W. Cahn, M. C. Flemings,

B. Ilschner, E. J. Kramer, S. Mahajan, and P. Veyssière, eds.), pp. 4804 – 4812, Oxford: Elsevier, 2001.

[73] H. Szymczak, "Magnetic materials and applications," in *Encyclopedia of Condensed Matter Physics* (F. Bassani, G. L. Liedl, and P. Wyder, eds.), pp. 204 – 211, Oxford: Elsevier, 2005.

[74] A. Cochardt, "Modified strontium ferrite, a new permanent magnet material," *Journal of Applied Physics*, vol. 34, no. 4, pp. 1273–1274, 1963.

[75] Y. Matsuura, N. Kitai, S. Hosokawa, and J. Hoshijima, "Relation between the alignment dependence of coercive force decrease ratio and the angular dependence of coercive force of ferrite magnets," *Journal of Magnetism and Magnetic Materials*, vol. 411, pp. 1 – 6, 2016.

[76] J.-L. Mattei, C. N. Le, A. Chevalier, A. Maalouf, N. Noutehou, P. Queffelec, and V. Laur, "A simple process to obtain anisotropic self-biased magnets constituted of stacked barium ferrite single domain particles," *Journal of Magnetism and Magnetic Materials*, vol. 451, pp. 208 – 213, 2018.

[77] T. Aiso, D. Shindo, and T. Sato, "Magnetization analysis of ba ferrite magnets by electron holography," *Journal of Magnetism and Magnetic Materials*, vol. 318, no. 1, pp. 18 – 22, 2007.

[78] F. Kools, A. Morel, R. Grössinger, J. Le Breton, and P. Tenaud, "Laco-substituted ferrite magnets, a new class of high-grade ceramic magnets; intrinsic and microstructural aspects," *Journal of Magnetism and Magnetic Materials*, vol. 242-245, pp. 1270 – 1276, 2002.

[79] J. Ding, W. Miao, P. McCormick, and R. Street, "High-coercivity ferrite magnets prepared by mechanical alloying," *Journal of Alloys and Compounds*, vol. 281, no. 1, pp. 32 – 36, 1998.

[80] L. E. Caldeira, W. C. Guaglianoni, J. Venturini, S. Arcaro, C. P. Bergmann, and S. R. Bragança, "Sintering-dependent mechanical and magnetic properties of spinel

cobalt ferrite (cofe2o4) ceramics prepared via sol-gel synthesis," *Ceramics International*, vol. 46, no. 2, pp. 2465 – 2472, 2020.

[81] B. Abraime, K. E. Maalam, L. Fkhar, A. Mahmoud, F. Boschini, M. A. Tamerd, A. Benyoussef, M. Hamedoun, E. Hlil, M. A. Ali, A. E. Kenz, and O. Mounkachi, "Influence of synthesis methods with low annealing temperature on the structural and magnetic properties of cofe2o4 nanopowders for permanent magnet application," *Journal of Magnetism and Magnetic Materials*, vol. 500, p. 166416, 2020.

[82] J. Jalli, Y. Hong, S. Gee, S. Bae, J. Lee, J. C. Sur, G. S. Abo, A. Lyle, S. Lee, H. Lee, and T. Mewes, "Magnetic and microwave properties of sm-doped $srfe_{12}$ o_{19} single crystals," *IEEE Transactions on Magnetics*, vol. 44, no. 11, pp. 2978–2981, 2008.

[83] G. Soria, P. Jenus, J. Marco, A. Mandziak, M. Sanchez-Arenillas, F. Moutinho, J. Prieto, P. Prieto, J. Cerdá, C. Tejera-Centeno, S. Gallego, M. Foerster, L. Aballe, M. Valvidares, H. Vasili, E. Pereiro, A. Quesada, and J. de la Figuera, "Strontium hexaferrite platelets: a comprehensive soft x-ray absorption and mössbauer spectroscopy study," *Scientific Reports*, vol. 9, no. 1, 2019.

[84] A. E. Ramírez, N. J. Solarte, L. Singh, J. A. Coaquira, and S. G. J., "Investigation of the magnetic properties of srfe12o19 synthesized by the pechini and combustion methods," *Journal of Magnetism and Magnetic Materials*, vol. 438, pp. 100 – 106, 2017.

[85] F. Tenorio Gonzalez, A. Bolarín Miró, F. Sánchez De Jesús, C. Cortés Escobedo, and S. Ammar, "Mechanism and microstructural evolution of polyol mediated synthesis of nanostructured m-type srfe12o19," *Journal of Magnetism and Magnetic Materials*, vol. 407, pp. 188 – 194, 2016.

[86] P. Long, L. Lezhong, W. Rui, T. Xiaoqiang, and H. Yun, "Low temperature sintering characteristics of hot press sintered srfe12o19 ferrites for use in microwave ltcc

circulators," *Rare Metal Materials and Engineering*, vol. 46, no. 4, pp. 951 – 954, 2017.

[87] A. U. Rashid, P. Southern, J. A. Darr, S. Awan, and S. Manzoor, "Strontium hexaferrite (srfe12o19) based composites for hyperthermia applications," *Journal of Magnetism and Magnetic Materials*, vol. 344, pp. 134 – 139, 2013.

[88] X. Liu, C. Cui, T. Li, A. Xia, and Y. Lv, "Ni@c nanocapsules-decorated srfe12o19 hexagonal nanoflakes for high-frequency microwave absorption," *Journal of Alloys and Compounds*, vol. 678, pp. 234 – 240, 2016.

[89] Z. Szotek, W. M. Temmerman, D. Ködderitzsch, A. Svane, L. Petit, and H. Winter, "Electronic structures of normal and inverse spinel ferrites from first principles," *Phys. Rev. B*, vol. 74, p. 174431, Nov 2006.

[90] D. S. Mathew and R.-S. Juang, "An overview of the structure and magnetism of spinel ferrite nanoparticles and their synthesis in microemulsions," *Chemical Engineering Journal*, vol. 129, no. 1, pp. 51 – 65, 2007.

[91] M. Amiri, M. Salavati-Niasari, and A. Akbari, "Magnetic nanocarriers: Evolution of spinel ferrites for medical applications," *Advances in Colloid and Interface Science*, vol. 265, pp. 29 – 44, 2019.

[92] R. Lamouri, O. Mounkachi, E. Salmani, M. Hamedoun, A. Benyoussef, and H. Ez-Zahraouy, "Size effect on the magnetic properties of cofe2o4 nanoparticles: A monte carlo study," *Ceramics International*, vol. 46, no. 6, pp. 8092 – 8096, 2020.

[93] P. Chandramohan, M. Srinivasan, S. Velmurugan, and S. Narasimhan, "Cation distribution and particle size effect on raman spectrum of cofe2o4," *Journal of Solid State Chemistry*, vol. 184, no. 1, pp. 89 – 96, 2011.

[94] G. D. Rieck and J. J. M. Thijssen, "The cation distribution in $CoFe_2O_4$," *Acta Crystallographica Section B*, vol. 24, pp. 982–983, Jul 1968.

[95] D. Howe, *Review of Permanent Magnet Applications and the Potential for High Energy Magnets*, pp. 585–616. Dordrecht: Springer Netherlands, 1991.

[96] R. Petrie, "Permanent magnets in review," in *Proceedings of Electrical/Electronics Insulation Conference*, pp. 207–210, 1993.

[97] B. Bochenkov and S. Lutz, "A review of modern materials of permanent magnets," pp. 201– 203 vol. 1, 01 2004.

[98] L. H. Thomas, "The calculation of atomic fields," *Mathematical Proceedings of the Cambridge Philosophical Society*, vol. 23, no. 5, p. 542–548, 1927.

[99] W. Kohn and L. J. Sham, "Self-consistent equations including exchange and correlation effects," *Phys. Rev.*, vol. 140, pp. A1133–A1138, Nov 1965.

[100] D. Shechtman, I. Blech, D. Gratias, and J. W. Cahn, "Metallic phase with long-range orientational order and no translational symmetry," *Phys. Rev. Lett.*, vol. 53, pp. 1951–1953, Nov 1984.

[101] J. M. Seminario, "An introduction to density functional theory in chemistry," in *Modern Density Functional Theory* (J. Seminario and P. Politzer, eds.), vol. 2 of *Theoretical and Computational Chemistry*, pp. 1 – 27, Elsevier, 1995.

[102] C. Daniel, "Density functional theories and coordination chemistry," in *Reference Module in Chemistry, Molecular Sciences and Chemical Engineering*, Elsevier, 2020.

[103] M. J. Esteban and P.-L. Lions, *Stationary Solutions of Nonlinear Schrödinger Equations with an External Magnetic Field*, pp. 401–449. Boston, MA: Birkhäuser Boston, 1989.

[104] J. M. Combes, P. Duclos, and R. Seiler, *The Born-Oppenheimer Approximation*, pp. 185–213. Boston, MA: Springer US, 1981.

[105] H. Essén, "The physics of the born–oppenheimer approximation," *International Journal of Quantum Chemistry*, vol. 12, no. 4, pp. 721–735, 1977.

[106] H. J. Schnitzer, "Hartree approximation in relativistic field theory," *Phys. Rev. D*, vol. 10, pp. 2042–2046, Sep 1974.

[107] F. Reines and H. W. Sobel, "Test of the pauli exclusion principle for atomic electrons," *Phys. Rev. Lett.*, vol. 32, pp. 954–954, Apr 1974.

[108] P. Lykos and G. W. Pratt, "Discussion on the hartree-fock approximation," *Rev. Mod. Phys.*, vol. 35, pp. 496–501, Jul 1963.

[109] A. Dalgarno, G. A. Victor, and D. R. Bates, "The time-dependent coupled hartree-fock approximation," *Proceedings of the Royal Society of London. Series A. Mathematical and Physical Sciences*, vol. 291, no. 1425, pp. 291–295, 1966.

[110] M. Moshinsky, "How good is the hartree-fock approximation," *American Journal of Physics*, vol. 36, no. 1, pp. 52–53, 1968.

[111] E. H. Lieb and B. Simon, "The thomas-fermi theory of atoms, molecules and solids," *Advances in Mathematics*, vol. 23, no. 1, pp. 22 – 116, 1977.

[112] P. A. M. Dirac, "Note on exchange phenomena in the thomas atom," *Mathematical Proceedings of the Cambridge Philosophical Society*, vol. 26, no. 3, p. 376–385, 1930.

[113] A. Görling, "Density-functional theory beyond the hohenberg-kohn theorem," *Phys. Rev. A*, vol. 59, pp. 3359–3374, May 1999.

[114] P. Hohenberg and W. Kohn, "Inhomogeneous electron gas," *Physical Review*, vol. 136, no. 3B, pp. B864–B871, 1964.

[115] W. Kohn and L. Sham, "Quantum density oscillations in an inhomogeneous electron gas," *Physical Review*, vol. 137, no. 6A, pp. A1697–A1705, 1965.

[116] S. Kurth, M. Marques, M. Lüders, and E. K. U. Gross, "Local density approximation for superconductors," *Phys. Rev. Lett.*, vol. 83, pp. 2628–2631, Sep 1999.

[117] Z. Wu and R. E. Cohen, "More accurate generalized gradient approximation for solids," *Phys. Rev. B*, vol. 73, p. 235116, Jun 2006.

[118] A. Zupan and M. Causà, "Density functional lcao calculations for solids: Comparison among hartree–fock, dft local density approximation, and dft generalized gradient approximation structural properties," *International Journal of Quantum Chemistry*, vol. 56, no. 4, pp. 337–344, 1995.

[119] H. J. F. Jansen and A. J. Freeman, "Total-energy full-potential linearized augmented-plane-wave method for bulk solids: Electronic and structural properties of tungsten," *Phys. Rev. B*, vol. 30, pp. 561–569, Jul 1984.

[120] E. Sjöstedt, L. Nordström, and D. Singh, "An alternative way of linearizing the augmented plane-wave method," *Solid State Communications*, vol. 114, no. 1, pp. 15 – 20, 2000.

[121] E. Wimmer, H. Krakauer, M. Weinert, and A. J. Freeman, "Full-potential self-consistent linearized-augmented-plane-wave method for calculating the electronic structure of molecules and surfaces: o_2 molecule," *Phys. Rev. B*, vol. 24, pp. 864–875, Jul 1981.

[122] J. C. Slater, "An augmented plane wave method for the periodic potential problem," *Phys. Rev.*, vol. 92, pp. 603–608, Nov 1953.

[123] K. Schwarz and P. Blaha, "Solid state calculations using wien2k," *Computational Materials Science*, vol. 28, no. 2, pp. 259 – 273, 2003.

[124] K. Schwarz, P. Blaha, and G. Madsen, "Electronic structure calculations of solids using the wien2k package for material sciences," *Computer Physics Communications*, vol. 147, no. 1-2, pp. 71–76, 2002.

[125] R. Yu, D. Singh, and H. Krakauer, "All-electron and pseudopotential force calculations using the linearized-augmented-plane-wave method," *Phys. Rev. B*, vol. 43, pp. 6411–6422, Mar 1991.

[126] D. M. Bylander and L. Kleinman, "Exact phillips-kleinman-like pseudopotential for transition metals," *Phys. Rev. B*, vol. 46, pp. 9837–9840, Oct 1992.

[127] C. J. Smallwood, R. E. Larsen, W. J. Glover, and B. J. Schwartz, "A computationally efficient exact pseudopotential method. i. analytic reformulation of the phillips-kleinman theory," *The Journal of Chemical Physics*, vol. 125, no. 7, p. 074102, 2006.

[128] C. N. Likos, B. M. Mladek, D. Gottwald, and G. Kahl, "Why do ultrasoft repulsive particles cluster and crystallize? analytical results from density-functional theory," *The Journal of Chemical Physics*, vol. 126, no. 22, p. 224502, 2007.

[129] K. Binder, D. Heermann, L. Roelofs, A. J. Mallinckrodt, and S. McKay, "Monte carlo simulation in statistical physics," *Computers in Physics*, vol. 7, no. 2, pp. 156–157, 1993.

[130] K. Binder, "Applications of monte carlo methods to statistical physics," *Reports on Progress in Physics*, vol. 60, pp. 487–559, may 1997.

[131] S. Zhang and Y. Tan, "Risk assessment of earth dam overtopping and its application research," *Natural Hazards*, vol. 74, no. 2, pp. 717–736, 2014.

[132] I. Buvat and D. Lazaro, "Monte carlo simulations in emission tomography and gate: An overview," *Nuclear Instruments and Methods in Physics Research Section A: Accelerators, Spectrometers, Detectors and Associated Equipment*, vol. 569, no. 2, pp. 323 – 329, 2006.

[133] D. P. Landau and K. Binder, *A guide to Monte Carlo simulations in statistical physics*. Cambridge university press, 2014.

[134] I. Beichl and F. Sullivan, "The metropolis algorithm," *Computing in Science Engineering*, vol. 2, no. 1, pp. 65–69, 2000.

[135] G. Bhanot, D. Duke, and R. Salvador, "Finite-size scaling and the three-dimensional ising model," *Phys. Rev. B*, vol. 33, pp. 7841–7844, Jun 1986.

[136] H. Herrmann, "Fast algorithm for the simulation of ising models," *Journal of statistical physics*, vol. 45, no. 1-2, pp. 145–151, 1986.

[137] S.-J. Cho, M.-J. Uddin, and P. Alaboina, "Chapter three - review of nanotechnology for cathode materials in batteries," in *Emerging Nanotechnologies in Rechargeable Energy Storage Systems* (L. M. Rodriguez-Martinez and N. Omar, eds.), Micro and Nano Technologies, pp. 83 – 129, Boston: Elsevier, 2017.

[138] L. Fkhar, A. Mahmoud, F. Boschini, M. Hamedoun, A. Benyoussef, E.-K. Hlil, M. Ali, and O. Mounkachi, "Structural, magnetic, and magnetocaloric properties in rare earth orthochromite (sm, nd, and la)cro3 for cooling product," *Journal of Superconductivity and Novel Magnetism*, vol. 33, no. 4, pp. 1023–1030, 2020.

[139] G. R. Amiri, M. Yousefi, M. Abolhassani, S. Manouchehri, M. Keshavarz, and S. Fatahian, "Magnetic properties and microwave absorption in ni–zn and mn–zn ferrite nanoparticles synthesized by low-temperature solid-state reaction," *Journal of magnetism and magnetic materials*, vol. 323, no. 6, pp. 730–734, 2011.

[140] S. Bera, A. Prince, S. Velmurugan, P. Raghavan, R. Gopalan, G. Panneerselvam, and S. Narasimhan, "Formation of zinc ferrite by solid-state reaction and its characterization by xrd and xps," *Journal of materials science*, vol. 36, no. 22, pp. 5379–5384, 2001.

[141] Y. I. Kim, D. Kim, and C. S. Lee, "Synthesis and characterization of cofe2o4 magnetic nanoparticles prepared by temperature-controlled coprecipitation method," *Physica B: Condensed Matter*, vol. 337, no. 1-4, pp. 42–51, 2003.

[142] K. Petcharoen and A. Sirivat, "Synthesis and characterization of magnetite nanoparticles via the chemical co-precipitation method," *Materials Science and Engineering: B*, vol. 177, no. 5, pp. 421–427, 2012.

[143] V. Gandhi, R. Ganesan, H. H. Abdulrahman Syedahamed, and M. Thaiyan, "Effect of cobalt doping on structural, optical, and magnetic properties of zno nanoparticles synthesized by coprecipitation method," *The Journal of Physical Chemistry C*, vol. 118, no. 18, pp. 9715–9725, 2014.

[144] O. Mounkachi, R. Lamouri, B. Abraime, H. Ez-Zahraouy, A. El Kenz, M. Hamedoun, and A. Benyoussef, "Exploring the magnetic and structural properties of nd-doped cobalt nano-ferrite for permanent magnet applications," *Ceramics International*, vol. 43, no. 16, pp. 14401–14404, 2017.

[145] P. Thakur, R. Sharma, M. Kumar, S. Katyal, N. Negi, N. Thakur, V. Sharma, and P. Sharma, "Superparamagnetic la doped mn-zn nano ferrites: Dependence on dopant content and crystallite size," *Materials Research Express*, vol. 3, 06 2016.

[146] Z. Yue, J. Zhou, L. Li, H. Zhang, and Z. Gui, "Synthesis of nanocrystalline nicuzn ferrite powders by sol–gel auto-combustion method," *Journal of magnetism and magnetic materials*, vol. 208, no. 1-2, pp. 55–60, 2000.

[147] B. Toksha, S. E. Shirsath, S. Patange, and K. Jadhav, "Structural investigations and magnetic properties of cobalt ferrite nanoparticles prepared by sol–gel auto combustion method," *Solid State Communications*, vol. 147, no. 11-12, pp. 479–483, 2008.

[148] S. S. Ebrahimi and J. Azadmanjiri, "Evaluation of nife2o4 ferrite nanocrystalline powder synthesized by a sol–gel auto-combustion method," *Journal of Non-Crystalline Solids*, vol. 353, no. 8-10, pp. 802–804, 2007.

[149] A. Sutka and G. Mezinskis, "Sol–gel auto-combustion synthesis of spinel-type ferrite nanomaterials," *Frontiers of Materials Science*, vol. 6, p. 128–141, 04 2012.

[150] J. I. DnnvBn, "The preparation of oriented clay mineral specimens for x-ray diffraction analysis by a filter-membrane peel technique," *American Mineralogist*, vol. 58, pp. 553–554, 1973.

[151] N. Iwashita, "Chapter 2 - x-ray powder diffraction," in *Materials Science and Engineering of Carbon* (M. Inagaki and F. Kang, eds.), pp. 7 – 25, Butterworth-Heinemann, 2016.

[152] T. Arii, A. Kishi, and Y. Kobayashi, "A new simultaneous apparatus for x-ray

diffractometry and differential scanning calorimetry (xrd-dsc)," *Thermochimica acta*, vol. 325, no. 2, pp. 151–156, 1999.

[153] C. G. Pope, "X-ray diffraction and the bragg equation," *Journal of Chemical Education*, vol. 74, no. 1, p. 129, 1997.

[154] A. A. Bunaciu, E. Udristioiu, and H. Aboul-Enein, "X-ray diffraction: Instrumentation and applications," *Critical reviews in analytical chemistry / CRC*, vol. 45, 04 2015.

[155] L. Reimer, "Scanning electron microscopy: Physics of image formation and microanalysis, second edition," *Measurement Science and Technology*, vol. 11, pp. 1826–1826, nov 2000.

[156] S. L. Flegler and S. L. Flegler, *Scanning & Transmission Electron Microscopy*. Oxford University Press, 1997.

[157] F. J. Pedrosa, J. Rial, K. M. Golasinski, M. N. Guzik, A. Quesada, J. F. Fernández, S. Deledda, J. Camarero, and A. Bollero, "Towards high performance cofe2o4 isotropic nanocrystalline powder for permanent magnet applications," *Applied Physics Letters*, vol. 109, no. 22, p. 223105, 2016.

[158] M. A. Ahmed, N. Imam, M. Hefny, and H. Gomaa, ""synthesis and characterization of nanoparticulate crystallite cobalt ferrite for permanent magnet applications"," *Journal of Ceramic Science and Technology*, vol. 7, 09 2016.

[159] L. Zhao, H. Yang, X. Zhao, L. Yu, Y. Cui, and S. Feng, "Magnetic properties of cofe2o4 ferrite doped with rare earth ion," *Materials Letters*, vol. 60, no. 1, pp. 1 – 6, 2006.

[160] A. Lima, M. Morales, J. Araújo, J. Soares, D. Melo, and A. Carriço, "Evaluation of (bh)max and magnetic anisotropy of cobalt ferrite nanoparticles synthesized in gelatin," *Ceramics International*, vol. 41, no. 9, Part B, pp. 11804 – 11809, 2015.

[161] N. Li, M. Zheng, X. Chang, G. Ji, H. Lu, L. Xue, L. Pan, and J. Cao, "Preparation of magnetic cofe2o4-functionalized graphene sheets via a facile hydrothermal method and their adsorption properties," *Journal of Solid State Chemistry*, vol. 184, no. 4, pp. 953 – 958, 2011.

[162] Y. Shi, J. Ding, and H. Yin, "Cofe2o4 nanoparticles prepared by the mechanochemical method," *Journal of Alloys and Compounds*, vol. 308, no. 1, pp. 290 – 295, 2000.

[163] A. Ponce, E. Chagas, R. Prado, C. Fernandes, A. Terezo, and E. Baggio-Saitovitch, "High coercivity induced by mechanical milling in cobalt ferrite powders," *Journal of Magnetism and Magnetic Materials*, vol. 344, pp. 182 – 187, 2013.

[164] P. R. Varma, R. S. Manna, D. Banerjee, M. R. Varma, K. Suresh, and A. Nigam, "Magnetic properties of cofe2o4 synthesized by solid state, citrate precursor and polymerized complex methods: A comparative study," *Journal of Alloys and Compounds*, vol. 453, no. 1, pp. 298 – 303, 2008.

[165] S. Eddahri, A. Razouk, M. Karimou, M. Sajieddine, and M. Sahlaoui, "Magnetic behaviors of spinel ferrite nanoparticles: a monte carlo simulation," *Applied Physics A*, vol. 125, no. 10, p. 694, 2019.

[166] A. Hossain, M. Sarker, M. Khan, and M. Rahman, "Spin effect on electronic, magnetic and optical properties of spinel cofe2o4: A dft study," *Materials Science and Engineering: B*, vol. 253, p. 114496, 2020.

[167] S. Mirzaee, S. Farjami Shayesteh, S. Mahdavifar, and S. Hekmatara, "Synthesis, characterization and monte carlo simulation of cofe2o4/polyvinylpyrrolidone nanocomposites: The coercivity investigation," *Journal of Magnetism and Magnetic Materials*, vol. 393, 05 2015.

[168] F. Liu, J. Dai, J. Liu, Y. Yang, and R. Fang, "Density functional theory study on the reaction mechanism of spinel cofe2o4 with co during chemical-looping combustion," *The Journal of Physical Chemistry C*, vol. 123, no. 28, pp. 17335–17342, 2019.

[169] R. Kodama, "Magnetic nanoparticles," *Journal of Magnetism and Magnetic Materials*, vol. 200, no. 1, pp. 359 – 372, 1999.

[170] R. Lamouri, L. Fkhar, E. Salmani, O. Mounkachi, M. Hamedoun, M. Ait Ali, A. Benyoussef, and H. Ez-Zahraouy, "A combined experimental and theoretical study of the magnetic properties of bulk cofe 2 o 4," *Applied Physics A*, vol. 126, pp. 1–6, 2020.

[171] M. Houshiar, F. Zebhi, Z. J. Razi, A. Alidoust, and Z. Askari, "Synthesis of cobalt ferrite (cofe2o4) nanoparticles using combustion, coprecipitation, and precipitation methods: A comparison study of size, structural, and magnetic properties," *Journal of Magnetism and Magnetic Materials*, vol. 371, pp. 43 – 48, 2014.

[172] X. Zeng, J. Zhang, S. Zhu, X. Deng, H. Ma, J. Zhang, Q. Zhang, P. Li, D. Xue, N. J. Mellors, *et al.*, "Direct observation of cation distributions of ideal inverse spinel cofe2o4 nanofibres and correlated magnetic properties," *Nanoscale*, vol. 9, no. 22, pp. 7493–7500, 2017.

[173] K. Schwarz, "Dft calculations of solids with lapw and wien2k," *Journal of Solid State Chemistry*, vol. 176, no. 2, pp. 319 – 328, 2003.

[174] P. Blaha, K. Schwarz, F. Tran, R. Laskowski, G. K. H. Madsen, and L. D. Marks, "Wien2k: An apw+lo program for calculating the properties of solids," *The Journal of Chemical Physics*, vol. 152, no. 7, p. 074101, 2020.

[175] J. P. Perdew, K. Burke, and M. Ernzerhof, "Generalized gradient approximation made simple," *Phys. Rev. Lett.*, vol. 77, pp. 3865–3868, Oct 1996.

[176] O. Iglesias and A. Labarta, "Finite-size and surface effects in maghemite nanoparticles: Monte carlo simulations," *Physical Review B*, vol. 63, no. 18, p. 184416, 2001.

[177] S. W. Hyun and C. S. Kim, "Superexchange interactions in inverse spinel lithium ferrites," *physica status solidi (b)*, vol. 244, no. 12, pp. 4586–4589, 2007.

[178] C. Srivastava, G. Srinivasan, and N. Nanadikar, "Exchange constants in spinel ferrites," *Phys. Rev. B*, vol. 19, 01 1979.

[179] J. S. Smart, "The néel theory of ferrimagnetism," *American Journal of Physics*, vol. 23, no. 6, pp. 356–370, 1955.

[180] Y. Kumar, A. Sharma, and P. M. Shirage, "Impact of different morphologies of cofe2o4 nanoparticles for tuning of structural, optical and magnetic properties," *Journal of Alloys and Compounds*, vol. 778, pp. 398 – 409, 2019.

[181] A. Kadiri, G. Ngantso, Y. El Amraoui, H. Ez-Zahraouy, A. Elkenz, and A. Benyoussef, "Ferromagnetic nanoparticles of ising spin-1 with a rubik's cube structure: Monte carlo simulations," *Journal of Superconductivity and Novel Magnetism*, vol. 31, 04 2018.

[182] M.-h. Zhang, C.-w. Zhang, P.-j. Wang, and S.-s. Li, "Prediction of high-temperature chern insulator with half-metallic edge states in asymmetry-functionalized stanene," *Nanoscale*, vol. 10, no. 43, pp. 20226–20233, 2018.

[183] Y. Kumar, A. Sharma, M. A. Ahmed, S. S. Mali, C. K. Hong, and P. M. Shirage, "Morphology-controlled synthesis and enhanced energy product (bh) max of cofe2o4 nanoparticles," *New Journal of Chemistry*, vol. 42, no. 19, pp. 15793–15802, 2018.

[184] B. H. Liu and J. Ding, "Strain-induced high coercivity in cofe2o4 powders," *Applied Physics Letters*, vol. 88, no. 4, p. 042506, 2006.

[185] A. López-Ortega, E. Lottini, C. d. J. Fernandez, and C. Sangregorio, "Exploring the magnetic properties of cobalt-ferrite nanoparticles for the development of a rare-earth-free permanent magnet," *Chemistry of Materials*, vol. 27, no. 11, pp. 4048–4056, 2015.

[186] A. Hubert and R. Schäfer, *Magnetic domains: the analysis of magnetic microstructures*. Springer Science & Business Media, 2008.

[187] J. Went, G. Rathenau, E. Gorter, and G. Van Oosterhout, "Hexagonal iron-oxide compounds as permanent-magnet materials," *Physical Review*, vol. 86, no. 3, p. 424, 1952.

[188] J. Zhang, J. Fu, F. Li, E. Xie, D. Xue, N. J. Mellors, and Y. Peng, "Bafe12o19 single-particle-chain nanofibers: preparation, characterization, formation principle, and magnetization reversal mechanism," *Acs Nano*, vol. 6, no. 3, pp. 2273–2280, 2012.

[189] F. Gu, W. Pan, Q. Liu, and J. Wang, "Electrospun magnetic srfe12o19 nanofibres with improved hard magnetism," *Journal of Physics D: Applied Physics*, vol. 46, no. 44, p. 445003, 2013.

[190] N. Yang, H. Yang, J. Jia, and X. Pang, "Formation and magnetic properties of nanosized pbfe12o19 particles synthesized by citrate precursor technique," *Journal of Alloys and Compounds*, vol. 438, no. 1-2, pp. 263–267, 2007.

[191] F. Pereira, M. Santos, R. Sohn, J. Almeida, A. Medeiros, M. Costa, and A. Sombra, "Magnetic and dielectric properties of the m-type barium strontium hexaferrite (ba x sr 1- x fe 12 o 19) in the rf and microwave (mw) frequency range," *Journal of Materials Science: Materials in Electronics*, vol. 20, no. 5, pp. 408–417, 2009.

[192] C. Doroftei, E. Rezlescu, N. Rezlescu, F. Tudorache, and P. Popa, "Strontium ferrite for magnetic recording prepared by self-combustion method," *J. Optoelectron. Adv*, pp. 2919–023, 2008.

[193] M. Radwan, M. Rashad, and M. Hessien, "Synthesis and characterization of barium hexaferrite nanoparticles," *Journal of Materials Processing Technology*, vol. 181, no. 1-3, pp. 106–109, 2007.

[194] Z. Zi, Y. Sun, X. Zhu, Z. Yang, W. Song, *et al.*, "Structural and magnetic properties of srfe12o19 hexaferrite synthesized by a modified chemical co-precipitation method," *Journal of Magnetism and Magnetic Materials*, vol. 320, no. 21, pp. 2746–2751, 2008.

[195] N. R. Panchal and R. B. Jotania, "Effect of swift heavy ion irradiation on structural and magnetic properties of strontium hexaferrites," in *Defect and Diffusion Forum*, vol. 341, pp. 155–168, Trans Tech Publ, 2013.

[196] Y. C. Wong, J. Wang, and G. B. Teh, "Structural and magnetic studies of srfe12o19 by sol-gel method," *Procedia Engineering*, vol. 76, pp. 45–52, 2014.

[197] M. Sadeghi, "Erratum to: Facile synthesis of srfe 12 o 19 nanoparticles and its photocatalyst application," *Journal of Materials Science: Materials in Electronics*, vol. 28, no. 14, pp. 10048–10048, 2017.

[198] M. Jean, V. Nachbaur, J. Bran, and J.-M. Le Breton, "Synthesis and characterization of srfe12o19 powder obtained by hydrothermal process," *Journal of Alloys and compounds*, vol. 496, no. 1-2, pp. 306–312, 2010.

[199] A. Z. Eikeland, M. Stingaciu, A. H. Mamakhel, M. Saura-Múzquiz, and M. Christensen, "Enhancement of magnetic properties through morphology control of srfe 12 o 19 nanocrystallites," *Scientific reports*, vol. 8, no. 1, pp. 1–9, 2018.

[200] P. Jing, J. Du, J. Wang, L. Pan, J. Li, Q. Liu, *et al.*, "Width-controlled m-type hexagonal strontium ferrite (srfe 12 o 19) nanoribbons with high saturation magnetization and superior coercivity synthesized by electrospinning," *Scientific reports*, vol. 5, p. 15089, 2015.

[201] M. Urbano-Peña, S. Palomares-Sánchez, I. Betancourt, T. Pérez-Juache, and F. Ruiz, "Effect of temperature on the magnetic properties of strontium hexaferrite synthesized by the pechini method," *Applied Physics A*, vol. 125, no. 10, p. 711, 2019.

[202] B. Liu, S. Zhang, B.-M. Steenari, and C. Ekberg, "Controlling the composition and magnetic properties of nano-srfe12o19 powder synthesized from oily cold mill sludge by the citrate precursor method," *Materials*, vol. 12, no. 8, p. 1250, 2019.

[203] D. Chen, Y. Meng, K. H. Gandha, D. Zeng, H. Yu, and J. Ping Liu, "Morphology

control of hexagonal strontium ferrite micro/nano-crystals," *AIP Advances*, vol. 7, no. 5, p. 056214, 2017.

[204] S. Mirkazemi, S. Alamolhoda, and Z. Ghiami, "Erratum to: Microstructure and magnetic properties of srfe 12 o 19 nano-sized powders prepared by sol-gel auto-combustion method with ctab surfactant," *Journal of Superconductivity and Novel Magnetism*, vol. 28, no. 5, pp. 1551–1558, 2015.

[205] D. Chen, Y. Meng, D. Zeng, Z. Liu, H. Yu, and X. Zhong, "Ctab-assisted low-temperature synthesis of srfe12o19 ultrathin hexagonal platelets and its formation mechanism," *Materials Letters*, vol. 76, pp. 84–86, 2012.

[206] G. A. Al-Garalleh, I. Bsoul, Y. Maswadeh, E. Al-Hwaitat, and S. H. Mahmood, "Effects of synthesis route on the structural and magnetic properties of sr1-xrexfe12o19 nanocrystalline hexaferrites," *Applied Physics A*, vol. 125, no. 7, p. 467, 2019.

[207] V. Dixit, C. N. Nandadasa, S.-G. Kim, S. Kim, J. Park, and Y.-K. Hong, "Site preference and magnetic properties of ga/in-substituted strontium hexaferrite: An ab initio study," *Journal of Applied Physics*, vol. 118, no. 20, p. 203908, 2015.

[208] V. Dixit, S.-G. Kim, J. Park, and Y.-K. Hong, "Effect of ionic substitutions on the magnetic properties of strontium hexaferrite: A first principles study," *AIP Advances*, vol. 7, no. 11, p. 115209, 2017.

[209] R. Skomski, "Nanomagnetics," May 2003.

[210] D. J. Sellmyer, "Strong magnets by self-assembly," *Nature*, vol. 420, no. 6914, pp. 374–375, 2002.

[211] E. F. Kneller and R. Hawig, "The exchange-spring magnet: a new material principle for permanent magnets," *IEEE Transactions on Magnetics*, vol. 27, no. 4, pp. 3588–3560, 1991.

[212] D. Roy, C. Shivakumara, and P. A. Kumar, "Observation of the exchange spring

behavior in hard–soft-ferrite nanocomposite," *Journal of magnetism and magnetic materials*, vol. 321, no. 5, pp. L11–L14, 2009.

[213] H. Yang, M. Liu, Y. Lin, and Y. Yang, "Simultaneous enhancements of remanence and (bh) max in bafe12o19/cofe2o4 nanocomposite powders," *Journal of Alloys and Compounds*, vol. 631, pp. 335–339, 2015.

[214] X. Meng, T. Liu, L. Yu, K. Jin, and S. Xu, "Nanocrystalline ni0.8zn0.2fe2o4/srfe12o19 composite fibers with enhanced exchange coupling behavior," *RSC Advances*, vol. 5, no. 59, pp. 48005–48011, 2015.

[215] A. Hilczer, K. Kowalska, E. Markiewicz, A. Pietraszko, and B. Andrzejewski, "Dielectric and magnetic response of srfe12o19–cofe2o4 composites obtained by solid state reaction," *Materials Science and Engineering: B*, vol. 207, pp. 47–55, 2016.

[216] L. Pan, D. Cao, P. Jing, J. Wang, and Q. Liu, "A novel method to fabricate cofe 2 o 4/srfe 12 o 19 composite ferrite nanofibers with enhanced exchange coupling effect," *Nanoscale research letters*, vol. 10, no. 1, p. 131, 2015.

[217] N. Pang, F. Ye, and Y. Jiang, "Synthesis of magnetically exchange coupled srfe12o19/feco composites through cryogenic ball milling," *Materials Research Express*, vol. 4, no. 7, p. 075031, 2017.

[218] F. Tavakolinia, M. Yousefi, S. S. S. Afghahi, S. Baghshahi, and S. Samadi, "Synthesis of novel hard/soft ferrite composites particles with improved magnetic properties and exchange coupling," *Processing and Application of Ceramics*, vol. 12, no. 3, pp. 248–256, 2018.

[219] M. Almessiere, Y. Slimani, and A. Baykal, "Exchange spring magnetic behavior of sr0. 3ba0. 4pb0. 3fe12o19/(cufe2o4) x nanocomposites fabricated by a one-pot citrate sol-gel combustion method," *Journal of Alloys and Compounds*, vol. 762, pp. 389–397, 2018.

[220] B. Abraime, M. A. Tamerd, A. Mahmoud, F. Boschini, A. Benyoussef, M. Hamedoun, Y. Xiao, A. El Kenz, and O. Mounkachi, "Experimental and theoretical in-

vestigation of srfe12o19 nanopowder for permanent magnet application," *Ceramics International*, vol. 43, no. 17, pp. 15999–16006, 2017.

[221] A. Weizenmann, M. Santos, and W. Figueiredo, "Coupling of ferromagnetic nanoparticles through dipolar interactions," *Physics Letters A*, vol. 376, no. 18, pp. 1535–1539, 2012.

[222] J. García-Otero, M. Porto, J. Rivas, and A. Bunde, "Influence of dipolar interaction on magnetic properties of ultrafine ferromagnetic particles," *Physical review letters*, vol. 84, no. 1, p. 167, 2000.

[223] D. Kechrakos and K. Trohidou, "Magnetic properties of dipolar interacting single-domain particles," *Physical Review B*, vol. 58, no. 18, p. 12169, 1998.

[224] G. Barrera, P. Tiberto, P. Allia, B. Bonelli, S. Esposito, A. Marocco, M. Pansini, and Y. Leterrier, "Magnetic properties of nanocomposites," *Applied Sciences*, vol. 9, no. 2, p. 212, 2019.

[225] J. N. Dahal, D. Neupane, and S. R. Mishra, "Exchange-coupling behavior in srfe12o19/la0. 7sr0. 3mno3 nanocomposites," *Ceramics*, vol. 2, no. 1, pp. 100–111, 2019.

[226] H. Yang, M. Liu, Y. Lin, G. Dong, L. Hu, Y. Zhang, and J. Tan, "Enhanced remanence and (bh) max of bafe12o19/cofe2o4 composite ceramics prepared by the microwave sintering method," *Materials Chemistry and Physics*, vol. 160, pp. 5–11, 2015.

[227] S. Torkian and A. Ghasemi, "Energy product enhancement in sufficiently exchange-coupled nanocomposite ferrites," *Journal of Magnetism and Magnetic Materials*, vol. 469, pp. 119–127, 2019.

List of publications

[1]: **R. Lamouri**, L. Fkhar, O. Mounkachi, A. Mahmoud, F. Boschini, S. Difi, E. Salmani, M. Hamedoun, M. Ait Ali,A. Benyoussef, H. Ez-zahraouy, "Improved magnetic properties of $SrFe_{12}O_{19}/CoFe_2O_4$ nanocomposite," submitted.

---

[2]: **R. Lamouri**, L. Fkhar, A. Mahmoud, F. Boschini, M. Hamedoun, M. Ait Ali, A. Benyoussef, O. Mounkachi, H. Ez-zahraouy, "Effect of the synthesis route on the magnetic properties of $SrFe_{12}O_{19}$ nanoparticles," submitted.

---

[3]: **R. Lamouri**, O. Mounkachi, E. Salmani, M. Hamedoun, A. Benyoussef, and H. Ez-Zahraouy, "Ab initio and Monte Carlo simulation of the magnetic properties of $MnFe_2O_4$," submitted.

---

[4]: **R. Lamouri**, O. Mounkachi, E. Salmani, M. Hamedoun, A. Benyoussef, and H. Ez-Zahraouy, "First principles calculations of the substitution effects on the electronic and magnetic properties of $SrFe_{12}O_{19}$," submitted.

---

[5]: L. Fkhar, **R. Lamouri**, A. Nayad, M. Hamedoun, A. Benyoussef, H. Ez-Zahraouy,O. Mounkachi, and M. Ait Ali, "Cobalt substitution effect on the structure andmagnetic proprieties of Fe_3O_4 nano-particles," Advances in Materials and Processing Technologies, 2020.

---

[6]: L. Fkhar, **R. Lamouri**, A. Mahmoud, F. Boschini, M. Hamedoun, H. Ez-Zahraouy,A. Benyoussef, E.-K. Hlil, M. Ali, and O. Mounkachi, "Enhanced magnetic and magnetocaloric properties of $La_{0.45}Nd_{0.25}Sr_{0.3}MnO_3/CuO$ composite," Journal of Superconductivity and Novel Magnetism, vol. 33, no. 8, pp. 2543–2549, 2020.

---

[7]: **R. Lamouri**, L. Fkhar, E. Salmani, O. Mounkachi, M. Hamedoun, M. Ait Ali,A. Benyoussef, and H. Ez-Zahraouy, "A combined experimental and theoretical study of the magnetic properties of bulk $CoFe_2O_4$," Applied Physics A, vol. 126,pp. 1–6, 2020.

---

[8]: **R. Lamouri**, O. Mounkachi, E. Salmani, M. Hamedoun, A. Benyoussef, and H. Ez-Zahraouy, "Size effect on the magnetic properties of $CoFe_2O_4$ nanoparticles: A Monte Carlo study," Ceramics International, vol. 46, no. 6, pp. 8092 – 8096, 2020.

---

[9]: E. Salmani, **R. Lamouri**, M. Rouchdi, M. Dehmani, H. Ez-Zahraouy, N. Hassanain,A. Mzerd, and A. Benyoussef, "Ab-initio studies of a half-metallic ferromagnetic behavior in $Ga_{1-2x}Mn_xCo_xN$ (x= 3 % and 6 %),"Physica A: Statistical Mechanics and its Applications, vol. 509, pp. 1120–1127, 2018.

---

[10]: **R. Lamouri**, E. Salmani, M. Dehmani, H. Ez-Zahraouy, and A. Benyoussef, "Electronic properties and magnetocaloric effect of $GdNi_4Si$: Ab initio calculations, mean-field approximation, and monte carlo simulation," Journal of Superconductivity and Novel Magnetism, vol. 31, no. 6, pp. 1819–1825, 2018.

---

[11]: E. Salmani, A. Laghrissi, **R. Lamouri**, M. Rouchdi, M. Dehmani, H. Ez-Zahraouy, N. Hassanain, A. Mzerd, and A. Benyoussef, "Theoretical study of doped and co-doped gallium nitride with (Cr, Ni): an LDA-SIC and Monte Carlo study," Journal of Superconductivity and Novel Magnetism, vol. 31, no. 4, pp. 1139–1148, 2018.

---

[12]: E. Salmani, A. Laghrissi, **R. Lamouri**, M. Rouchdi, M. Dehmani, H. Ez-Zahraouy,N. Hassanain, A. Mzerd, and A. Benyoussef, "Theoretical study of electronic, magnetic and optical properties of TM(V, Cr, Mn and Fe) doped SnO_2: ab-initio and Monte Carlo simulation," Optical and Quantum Electronics, vol. 50, no. 2, 2018.

---

[13]: O. Mounkachi, **R. Lamouri**, M. Hamedoun, H. Ez-Zahraouy, E. Salmani, andA. Benyoussef, "Effect of defects disorder on the half-metallicity, magnetic proper-ties, and gap states of Fe_3O_4: a first-principles study," Journal of Superconductivity and Novel Magnetism, vol. 30, no. 11, pp. 3221–3224, 2017.

---

[14]: O. Mounkachi, **R. Lamouri**, B. Abraime, H. Ez-Zahraouy, A. El Kenz, M. Hamedoun, and A. Benyoussef, "Exploring the magnetic and structural properties of Nd-doped cobalt nano-ferrite for permanent magnet applications," Ceramics Inter-national, vol. 43, no. 16, pp. 14401–14404, 2017.

---

[15]: **R. Lamouri**, M. Tadout, M. Hamedoun, A. Benyoussef, H. Ez-zahraouy, M. Benaissa, and O. Mounkachi, "Effect of the cations distribution on the magnetic properties of $SnFe_2O_4$: First-principles study," Journal of Magnetism and Magnetic Materials, vol. 436, pp. 6–10, 2017.

---

[16]: **R. Lamouri**, E. Salmani, H. Ez-Zahraouy, and A. Benyoussef, "Band-gap engineering of CdS, CdSe and ZnSe first-principles calculations," Proceedings of 2016 International Renewable and Sustainable Energy Conference, IRSEC 2016, pp. 120–123, 2017.

---

[17]: E. Salmani, A. Laghrissi, **R. Lamouri**, M. Dehmani, E. Benchafia, H. Ez-Zahraouy,and A. Benyoussef, "Electronic, optical and magnetic properties of TM (Cr and Fe)doped titania TiO_2: Ab-initio calculations, mean-field approximation and Monte Carlo simulation," Optical and Quantum Electronics, vol. 49, no. 3, 2017.

---

[18]: E. Salmani, A. Laghrissi, **R. Lamouri**, H. Ez-Zahraouy, and A. Benyoussef, "The electronic, magnetic and optical properties of ZnO doped with doubles impurities (Cr, Fe): An LDA-SIC and Monte Carlo study," Journal of Magnetism and Magnetic Materials, vol. 422, pp. 348–355, 2017.

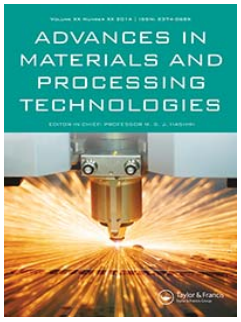

Advances in Materials and Processing Technologies

ISSN: (Print) (Online) Journal homepage: https://www.tandfonline.com/loi/tmpt20

Cobalt substitution effect on the structure and magnetic proprieties of Fe3O4 nano-particles

L. Fkhar , R. Lamouri , A. Nayad , M. Hamedoun , A. Benyoussef , H. Ez-Zahraouy , O. Mounkachi & M. Ait Ali

To cite this article: L. Fkhar , R. Lamouri , A. Nayad , M. Hamedoun , A. Benyoussef , H. Ez-Zahraouy , O. Mounkachi & M. Ait Ali (2020): Cobalt substitution effect on the structure and magnetic proprieties of Fe3O4 nano-particles, Advances in Materials and Processing Technologies, DOI: 10.1080/2374068X.2020.1812325

To link to this article: https://doi.org/10.1080/2374068X.2020.1812325

Published online: 31 Aug 2020.

Journal of Superconductivity and Novel Magnetism
https://doi.org/10.1007/s10948-020-05509-y

ORIGINAL PAPER

Enhanced Magnetic and Magnetocaloric Properties of $La_{0.45}Nd_{0.25}Sr_{0.3}MnO_3$/CuO Composite

L. Fkhar[1] · R. Lamouri[2] · A. Mahmoud[3] · F. Boschini[3] · M. Hamedoun[2] · H. Ez-Zahraouy[2] · A. Benyoussef[2,4] · E-K. Hlil[5] · M. Ait Ali[1] · O. Mounkachi[2]

Received: 6 March 2020 / Accepted: 8 April 2020

Abstract
This work is devoted to investigating the magnetic and magnetocaloric properties of $La_{0.45}Nd_{0.25}Sr_{0.3}MnO_3$-CuO composite prepared by the solid-state reaction with various concentration of CuO (2 wt.%, 5 wt.%, and 10 wt.%). The X-ray diffraction (XRD) and the scanning electron microscopy (SEM) techniques were used to identify the obtained structural phases and microstructural morphologies in the prepared pellets. A second-order transition was observed with critical a temperature around 294 K for 2 wt.% and 10 wt.% and 321 K for 5 wt.% of the CuO phase in the composite. Magnetic entropy changes in $La_{0.45}Nd_{0.25}Sr_{0.3}MnO_3$-CuO composites were calculated using the Maxwell approximation around the magnetic transition. The highest values of magnetic entropy change were found for 5 wt.% of CuO in $La_{0.45}Nd_{0.25}Sr_{0.3}MnO_3$-CuO pellet composites which is attributed to the localization of the copper oxide in the grains boundaries of $La_{0.45}Nd_{0.25}Sr_{0.3}MnO_3$ perovskite.

Keywords $La_{0.45}Nd_{0.25}Sr_{0.3}MnO_3$/CuO pellet · Composites · Magnetic properties · Magnetocaloric effect

1 Introduction

Magnetic refrigeration based on the magnetocaloric effect (MCE) has taken a great interest over the past decade as a promising technology to replace the conventional cooling techniques. Since the discovery of the magnetocaloric effect (MCE) in 1881 [1], magnetic materials have stimulated theoretical and experimental groups to look for ferromagnetic materials with magnetic transition near room temperature [2–5]. The gadolinium metal and its derivative intermetallic compounds have been widely studied fundamentally and proved their efficiency in functional devices [6, 7]. Although, their difficult synthesis route with high cost and their easy oxidation and corrosion in the presence of water limited their use in a wide range of applications. Recently, manganite perovskite materials with the general foruma $Ln_{1-x}A_xMnO_3$ (Ln = La, Nd… A = Ca, Sr, Br…) have attracted much attention because of their large magnetocaloric effect [8–12]. Several low cost and simple synthesis methods have been used to prepare rare-earth manganite perovskite such as coprecipitation, sol-gel method, solid-state reaction, and others [13–17]. Besides the optimization of the synthesis parameters, a number of studies have been devoted to improve the structural and magnetic, as well as the magnetocaloric, properties of rare-earth manganite perovskites and their applicability as refrigerants. Cherif et al. [18] have studied the magnetocaloric effect in Nd-doped $LaSrMnO_3$ perovskite prepared by solid-state reaction and it was found that the magnetic entropy change increases with Nd insertion in the $(La_{0.7-x}Nd_x)Sr_{0.3}MnO_3$ material. Shalpa et al. [19] studied the crystallographic and magnetic properties of Nd-doped $La_{0.7}Sr_{0.3}MnO_3$ nanoparticles synthesized using sol-gel method with two different annealing temperatures. Cr-doped $La_{0.7}Sr_{0.3}MnO_3$ pollycrystalline compounds have been synthesized by Kallel et al. [20], using solid-state reaction and large magnetic entropy change and RCP of 1.203 J/kg. K and 59 J/kg, respectively, have been obtained for

✉ O. Mounkachi
omar.mounkachi@um5.ac.ma

1 Coordination Chemistry Laboratory, Faculty of Sciences Semlalia (UCA-FSSM), Cadi Ayyad University, B.P. 2390 -, 40000 Marrakech, Morocco

2 Laboratory of Condensed Matter and Interdisciplinary Sciences (LaMCScI), Faculty of Science, Mohammed V University, B. P. 1014, Rabat, Morocco

3 GREENMAT, CESAM, Institute of Chemistry B6, University of Liege, 4000 Liège, Belgium

4 Hassan II Academy of Science and Technology, Rabat, Morocco

5 CNRS-UJF, Institut Néel, B. P. 166, 38042 Grenoble Cedex, France

Published online: 09 May 2020

Applied Physics A (2020) 126:325
https://doi.org/10.1007/s00339-020-03510-9

Applied Physics A
Materials Science & Processing

A combined experimental and theoretical study of the magnetic properties of bulk $CoFe_2O_4$

R. Lamouri[1,2] · L. Fkhar[2,3] · E. Salmani[1] · O. Mounkachi[1] · M. Hamedoun[2] · M. Ait Ali[3] · A. Benyoussef[1,2,4] · H. Ez-Zahraouy[1]

Received: 5 February 2020 / Accepted: 27 March 2020

Abstract
This work is devoted to studying experimentally and theoretically the structural and magnetic properties of bulk cobalt spinel ferrite. Solid-state reaction with optimized synthesis conditions is used to prepare $CoFe_2O_4$. The crystallization of $CoFe_2O_4$ in the FCC structure was confirmed with the X-ray diffraction. The microstructural properties are performed using the scanning electron microscopy. The magnetic properties of the bulk cobalt ferrite were performed experimentally using the superconducting quantum interference device magnetometer (SQUID). Monte Carlo simulation with periodic boundary conditions was used to simulate bulk $CoFe_2O_4$ with a large enough size of the system. The obtained magnetization and susceptibility as a function of temperature show that $CoFe_2O_4$ exhibits a second-order transition to paramagnetic phase around 725 K. To carry out the maximum energy product, experimental and theoretical magnetic hysteresis loops at room temperature were performed. It is found that the synthesized $CoFe_2O_4$ has a high saturation magnetization of about 87.89 emu/g, which is close to the theoretical value of 97.13 emu/g. Lower coercivity–sugariness ratio was found which indicates that bulk cobalt spinel ferrite is a magnetic multi-domain in nature. To evaluate the efficiency of bulk $CoFe_2O_4$, the maximum energy product was calculated at room temperature. Our results demonstrate from a microscopic to the macroscopic scale the performance of $CoFe_2O_4$ as a promising magnetic material in the new energy technology generation.

Keywords Bulk $CoFe_2O_4$ · Solid-state reaction · Monte carlo simulation · Magnetic properties

1 Introduction

The spinel ferrites are a class of materials with the general formula $[Me^{2+}][Fe^{3+}]_2O_4$ (Me is transition metal; Me = Fe, Co, Ni, Zn, Cu) which crystallize in a face-centered cubic system. Two types of interstices called tetrahedral "A-site" and octahedral sites "B-site" are present in the spinel structure. Depending on the preference site of the metal ions, the spinel structure is regrouped into three categories: a normal spinel structure where the Me^{2+} cations occupy the tetrahedral sites and Fe^{3+} cations occupy the octahedral sites. The second type of the spinel structure is known as a random spinel structure where the Me^{2+} and Fe^{3+} cations are randomly distributed among the tetrahedral and octahedral sites with an inversion factor that varies according to the metal ion and the method of synthesis, while the third type is the inverse spinel structure where the tetrahedral sites are occupied by the Fe^{3+} cations and the octahedral sites are shared between the Fe^{3+} and Me^{2+} cations [1]. This family of material is well used in the modern technology such as catalysis [2], electronic circuit [3], power delivering devices [4], magnetic refrigeration [5] and others [6, 7].

Cobalt ferrite is considered as one of the most studied materials in the spinel ferrite family because of its chemical and mechanical stability, low synthesis cost, high coercivity, significant saturation magnetization and high cubic

✉ R. Lamouri
rachida.lamouri@gmail.com

1 LaMCScI, B.P. 1014, Faculty of Science, Mohammed V University, Rabat, Morocco

2 Materials and Nanomaterials Center, MAScIR Foundation, Rabat Design Center Rue Mohamed Al Jazouli – Madinat Al Irfane, 10 100 Rabat, Morocco

3 Coordination Chemistry Laboratory, Faculty of Sciences Semlalia (UCA-FSSM), Cadi Ayyad University, B.P. 2390, 40000 Marrakech, Morocco

4 Hassan II Academy of Science and Technology, Rabat, Morocco

Published online: 07 April 2020

Ceramics International 46 (2020) 8092–8096

Contents lists available at ScienceDirect

Ceramics International

journal homepage: www.elsevier.com/locate/ceramint

Size effect on the magnetic properties of CoFe2O4 nanoparticles: A Monte Carlo study

R. Lamouri[a,b,*], O. Mounkachi[a], E. Salmani[a], M. Hamedoun[b], A. Benyoussef[a,b,c], H. Ez-Zahraouy[a]

[a] LaMCScI, B.P. 1014, Faculty of Science, Mohammed V University, Rabat, Morocco
[b] Materials and Nanomaterials Center, MAScIR Foundation, Rabat Design Center Rue Mohamed Al Jazouli – Madinat Al Irfane, Rabat, 10 100, Morocco
[c] Hassan II Academy of Science and Technology, Rabat, Morocco

ARTICLE INFO

Keywords:
$CoFe_2O_4$ single nanoparticles
Monte Carlo simulation
Permanent magnet

ABSTRACT

In this study, we report the size-effects on the magnetic properties of $CoFe_2O_4$ hard ferrite single nanoparticles using Monte Carlo simulation within the Ising model. Free boundaries conditions were used to simulate the cubic nanoparticles with different sizes. Saturation and remanent magnetization increased with the increase of the particle size. Rise of the squareness ratio (Mr/Ms) towards high values is observed. Furthermore, the single-domain size limit is shown for the size of 21 nm. Besides, we evaluated the performance of the cubic shaped $CoFe_2O_4$ permanent magnet in term of the maximum energy product. A high value of the $(BH)_{max}$ of about 2.83 MG Oe at room temperature for 21 nm was achieved. The obtained results allowed us to determine the theoretical limits of the magnetic properties of the cubic shaped $CoFe_2O_4$ nanoparticles and pave the way for the development of $CoFe_2O_4$ spinel ferrites for permanent magnet applications.

1. Introduction

In the last decade, a great interest has been given to nano-sized magnetic materials because of the high demand for miniaturized technological devices. Understanding the magnetic properties at the nanoscale is a crucial issue to enhance the performance of permanent magnet material. As it is well known, the magnetic properties of nanoparticles depend strongly on their shape and size, surface effects, magnetic anisotropy, etc. As the particle size decreases, a reduction of the saturation magnetization (Ms) is observed due to the existence of a disordered spin configuration at the surface compared to the core configuration. The surface effects become predominant as the size of the particles decreases which make the surface and the finite-size effects commonly correlated [1].

Nowadays, Rare-earth based magnets are still the strongest type of permanent magnet [2]. Although, the risk of supply of rare-earth elements increases progressively because of the natural exhaustion and some political and environmental restrictions. Therefore, researchers all over the world are looking for suitable magnetic materials to replace the rare-earth magnets [3]. To make a good choice of the alternative material, two quantities should be as high as possible: Remanent induction (Br) and coercive field (Hc). From those quantities, the energy product of a magnetic material, which is the main property of permanent magnets, is calculated [4].

The hard magnetic material $CoFe_2O_4$ has been considered as a promising candidate for permanent magnet application due to its interesting properties such as high coercivity, significant saturation magnetization, and easy synthesis route with low cost and good chemical stability [5]. Early works were devoted to enhancing the magnetic properties of $CoFe_2O_4$ using various synthesis methods and optimizing some steps and parameters from those conventional methods [6–8]. Effect of doping on the properties of $CoFe_2O_4$ spinel ferrite has been performed [9–11]. Thus, synthesizing nanocomposites based on $CoFe_2O_4$ spinel ferrite has been explored by others [12–14]. Recently, several experimental studies have been focused on the shape-controlled synthesis of $CoFe_2O_4$ with different size of nanoparticles and without modifying the chemical composition of the pure ferrite [15,16]. Until now, a maximum energy product of about 2.41 MG.Oe at room temperature is obtained experimentally [16].

Although, numerous models have been postulated to explain the magnetic properties in nanoparticles compared to those of bulk materials [17–19], No numerical simulation, to our knowledge, has been dedicated to predicting the maximum energy product that can be achieved for $CoFe_2O_4$. To contribute to the understanding and development of $CoFe_2O_4$ for permanent magnet application, we present in this work a Monte Carlo simulation of cubic shaped single particles of $CoFe_2O_4$ that aims to study the size effect on the magnetic properties and take out the theoretical limits of the maximum energy product of

* Corresponding author. LaMCScI, B.P. 1014, Faculty of Science, Mohammed V University, Rabat, Morocco.
E-mail address: rachida.lamouri@gmail.com (R. Lamouri).

https://doi.org/10.1016/j.ceramint.2019.12.035
Received 14 October 2019; Received in revised form 25 November 2019; Accepted 3 December 2019
Available online 04 December 2019

Physica A 509 (2018) 1120–1127

Contents lists available at ScienceDirect

Physica A

journal homepage: www.elsevier.com/locate/physa

Ab-initio studies of a half-metallic ferromagnetic behavior in $Ga_{1-2x}Mn_xCo_xN$ ($x = 3\%$ and 6%)

E. Salmani [a], R. Lamouri [a], M. Rouchdi [c,*], M. Dehmani [a], H. Ez-Zahraouy [a], N. Hassanain [c], A. Mzerd [c], A. Benyoussef [b]

[a] Laboratoire de la Matière Condensée et Sciences Interdisciplinaires (LaMCScI), Morocco
[b] Institute for Nanomaterials and Nanotechnologies, MAScIR, Rabat, Morocco
[c] Équipe des semi-conducteurs et technologie des capteur d'environnement STCE-Centre de Recherche en É nergie-Mohammed V University, Faculty of Sciences, B.P. 1014, Rabat, Morocco

HIGHLIGHTS

- Doped GaN were executed by using both ab-initio calculations and Monte Carlo Simulation.
- The ferromagnetic stability state is investigated by comparing the total energies.
- Doped GaN with half-metallic behavior and high Neel temperature could be used for spintronic technologies.

ARTICLE INFO

Article history:
Received 1 June 2017
Received in revised form 29 May 2018
Available online 23 June 2018

Keywords:
Diluted semiconductor
Half-metallic ferromagnetic and Monte Carlo approach

ABSTRACT

The half-metallic ferromagnetic of Gallium nitride doped with double impurities $Ga_{1-2x}Mn_xCo_xN$ ($x = 3\%$ and 6%) has been investigated by means of first principles investigation combined with Monte Carlo Simulation. The stability of the ferromagnetic state is investigated by comparing the total energies to the spin-glass state. The exchange interactions obtained from first principle calculations and used in a classical Ising model by a Monte Carlo approach resulted in half-metallic ferromagnetic states with high Neel temperature.

0. Introduction

GaN compound doped with transition metal belongs to the materials family which exhibit a half-metallic (HM) behavior referred generally as half-metallic ferromagnetic (HM-FM). This property consists of separating the spins, where one spin direction presents an insulating behavior but a metallic for the other spin channel. Their electronic density of states is completely spin polarized on the Fermi level and the conductivity is dominated by these metallic single-spin charges carriers. Groot et al. [1,2] was the first introducing this property. Recently, the diluted magnetic semiconductors (DMS) systems have designated that the local magnetic states are created at the impurity bands that come into view semiconductor gap [3]. In fact, the complex and intriguing properties of the DMS has also been demonstrated that these materials became suitable for practical applications in spintronic and future electronics devices and provided new importance to these materials [4–7]. In the same way, the half metallic antiferromagnetic DMSs can be achieved for impurities bands in the gap. Nevertheless, this kind of materials has not been examined by experimental studies. However, it can be considered as a promising material to spintronic application.

* Corresponding author.
E-mail address: rouchdi.mus@gmail.com (M. Rouchdi).

https://doi.org/10.1016/j.physa.2018.06.109
0378-4371/

J Supercond Nov Magn
https://doi.org/10.1007/s10948-017-4394-9

ORIGINAL PAPER

Electronic Properties and Magnetocaloric Effect of $GdNi_4Si$: Ab Initio Calculations, Mean Field Approximation, and Monte Carlo Simulation

Rachida Lamouri[1] · El Mehdi Salmani[1] · Mustapha Dehmani[1] · Hamid Ez-Zahraouy[1] · Abdelilah Benyoussef[1,2]

Received: 17 August 2017 / Accepted: 19 October 2017

Abstract We investigated the magnetic properties and magnetocaloric effect of $GdNi_4Si$ by using a combination of first-principle density functional theory (DFT) calculations and Monte Carlo Simulation. Ab initio calculations show the stability of the ferromagnetic phase in this material. The Monte Carlo simulations combined with ab initio exchange coupling constants as input parameters lead to discuss the transition temperature, critical exponents, and isothermal entropy changes. The measured critical temperature and the isothermal magnetic entropy changes for a field change of $14T$ in good agreement with the experimental data.

Keywords Magnetocaloric effect · Exchange coupling · Monte Carlo · Ab initio · Critical exponent · Ising model

1 Introduction

The ternary Gd–Ni–Si alloy system has attracted many research interests due mainly to the variety of the crystallographic structures and their interesting magnetic properties, mainly in magnetic refrigeration which is based on the modification of the thermodynamic properties of the materials under the influence of an external magnetic field [1, 2].

Hence, The magnetic properties of rare earth transition-metal compounds, which are orthorhombic derivatives of the basic CaCu5-type structure, have been investigated experimentally by A.V. Morozkin et al. [3]. The magnetic properties of $GdNi_4Si$ show a ferromagnetic-type ordering at 25 K. The saturation behavior of magnetization at 2 K and the value of the magnetic moment of 7.2 μ_B/fu (in a 140-kOe field at 2 K) suggest a collinearly ordered ferromagnetic state of GdNi4Si. The ΔS_m reaches a maximum value of − 22.9 J/kg K for a field change of 140 kOe and the maximal value of − 12.7 J/kg K for a field change of 50 kOe in the neighborhood of 26 K [3].

In this work, we extend the zero-temperature first-principles calculations of GdNi4Si within the density functional theory (DFT) scheme to finite-temperature Monte Carlo (MC) simulations, where exchange coupling constants and magnetic moments are taken from ab initio calculations. This allows us to simulate the temperature dependence of magnetic, structural, and thermodynamic properties as well as the magnetocaloric effect of the material $GdNi_4Si$.

This paper is organized as follows. Section 2 describes the computational approach used in this work. The structural and magnetic stability of GdNi4Si are given in Section 3. Section 4 gives the Monte Carlo simulation results. Finally, Section 5 presents our conclusions.

2 Computational Details

The investigations of magnetic and magnetocaloric properties of GdNi4Si are carried out using full-potential linearized augmented plane wave (FP-LAPW) approach as implemented in WIEN2k code [4]. The generalized gradient approximation (GGA) has been used for the parameterization of the exchange energy [5].

✉ Mustapha Dehmani
dehmani01@yahoo.fr

1 Laboratoire de la Matière Condensée et Sciences Interdisciplinaires (LaMCScI), Department of Physics, Faculty of Sciences, University Mohammed V, Rabat, Morocco

2 Institute of Nanomaterials and Nanotechnology, MASciR, Rabat, Morocco

Published online: 03 November 2017

J Supercond Nov Magn
DOI 10.1007/s10948-017-4287-y

ORIGINAL PAPER

Theoretical Study of Doped and Co-doped Gallium Nitride with (Cr, Ni): an LDA-SIC and Monte Carlo Study

E. Salmani[1] · A. Laghrissi[1] · R. Lamouri[1] · M. Rouchdi[3] · M. Dehmani[1] · H. Ez-Zahraouy[1] · N. Hassanain[3] · A. Mzerd[3] · A. Benyoussef[2]

Received: 31 May 2017 / Accepted: 2 August 2017

Abstract Using a composition of first-principle density functional theory (DFT) calculations and Monte Carlo simulation with the calculation within the self-interaction-correction local-density approximation, the electronic, magnetic, and optical properties of doped and co-doped GaN ($Ga_{1-x}Cr_xN$, $Ga_{1-x}Ni_xN$) and GaN ($Ga_{1-2x}Cr_xNi_xN$) ($x = 0.03$ and 0.06), respectively, have been investigated. Our results have proven that the half-metallic ferromagnetic state still persists of co-doped GaN. In comparing the total energies, ab initio calculations certify the magnetic-state stability of the ferromagnetic phase compared with the spin-glass state. The exchange interactions obtained from the ab initio calculations were used as input parameters in a classical Ising model by Monte Carlo simulation to confirm the half-metallic ferromagnetic states with high Neel temperature.

Keywords Diluted semiconductor · Half-metallic ferromagnetic · Monte Carlo simulation

✉ M. Rouchdi
rouchdi.mus@gmail.com

[1] Laboratoire de la Matière Condensée et Sciences Interdisciplinaires (LaMCScI), Mohammed V University, Rabat, Morocco

[2] Institute for Nanomaterials and Nanotechnologies, MAScIR, Rabat, Morocco

[3] Équipe des semi-conducteurs et technologie des capteur d'environnement STCE, Centre de Recherche en Énergie, Faculty of Sciences, Mohammed V University, B.P. 1014, Rabat, Morocco

1 Introduction

GaN compound belongs to the family of materials which exhibit a half-metallic (HM) behavior referred generally as half-metallic ferromagnetic (HM-FM). This property consists of separating the spins, where one spin direction presents an insulating behavior but a metallic for the other spin channel. Their electronic density of states is completely spin polarized on the Fermi level, and the conductivity is dominated by these metallic single-spin charge carriers. Groot et al. [1, 2] was the first in introducing this property. Recently, the diluted magnetic semiconductor (DMS) systems have designated that the local magnetic states are created at the impurity bands that come into view in a semiconductor gap [3]. In the same way, the half-metallic antiferromagnetic DMSs can be achieved for impurities of the bands in the gap. Nevertheless, this kind of materials has not been examined by experimental studies. However, it can be considered a promising material to spintronic application.

In this work, we aim to investigate a complex DMS doped with double impurities $Ga_{1-2x}Cr_xNi_xN$ with $x = 0.03$ and 0.06 in turn to obtain a HM-FM behavior with high Neel temperature by discussing the electronic, optical, and magnetic properties, using the self-interaction-correction local-density approximation (SIC-LDA) and Monte Carlo simulation.

2 Computational Details

The investigations of the electronic, optical, and magnetic properties co-doped GaN with (Cr, Ni) $Ga_{1-2x}Cr_xNi_xN$ with $x = 0.03$ and 0.06 are executed by Korringa-Kohn-Rostoker method combined with the coherent potential

Published online: 15 August 2017

Opt Quant Electron (2018)50:85
https://doi.org/10.1007/s11082-018-1355-x

Theoretical study of electronic, magnetic and optical properties of TM (V, Cr, Mn and Fe) doped SnO_2: ab-initio and Monte Carlo simulation

E. Salmani[1] · A. Laghrissi[1,4] · R. Lamouri[1] · M. Rouchdi[5] · M. Dehmani[1] · H. Ez-Zahraouy[1] · N. Hassanain[5] · A. Mzerd[5] · A. Benyoussef[2,3]

Received: 3 February 2017 / Accepted: 29 January 2018

Abstract SnO_2:TM (V, Cr, Mn and Fe) based dilute magnetic semiconductors are investigated within self-interaction-corrected local density approximation (LSDA-SIC) from first-principles calculation. LSDA-SIC results are compared with the calculated ones within standard LSDA, the stable magnetic state of the system is evaluated by comparing the total energies of ferromagnetic state and spin-glass state. The Ferromagnetic and half metallic behaviors was observed and conformed with the local-moment-disordered state energy for LSDA and LSDA-SIC approximation in [Sn 0.95 TM 0.05 (V, Cr, Mn and Fe)]O_2. The exchange interactions obtained from first principle calculations and used in a classical Ising model by a Monte Carlo approach resulted in ferromagnetic states with Curie temperatures within the ambient conditions.

Keywords Ab-initio · Self-interaction correction · SnO_2 · Monte Carlo approach · X-ray absorption spectra

✉ M. Rouchdi
rouchdi.mus@gmail.com

[1] Laboratoire de la Matière Condensée et Sciences Interdisciplinaires (LaMCScI), Faculty of science, Mohammed V University, Rabat, Morocco

[2] Institute for Nanomaterials and Nanotechnologies, MAScIR, Rabat, Morocco

[3] Académie Hassan II des Sciences et Techniques, Rabat, Morocco

[4] Institute for Materials and Surface Technology (IMST), HAW Kiel-University of Applied Sciences, Grenztrasse 3, 24149 Kiel, Germany

[5] Centre de Recherche en Énergie- Équipe des semi-conducteurs et technologie des capteurs d'environnement (STCE)- Faculty of Sciences, Mohammed V University, B.P. 1014, Rabat, Morocco

Published online: 01 February 2018

J Supercond Nov Magn
DOI 10.1007/s10948-017-4108-3

ORIGINAL PAPER

Effect of Defects Disorder on the Half-Metallicity, Magnetic Properties, and Gap States of Fe_3O_4: a First-Principles Study

O. Mounkachi[1] · R. Lamouri[2] · M. Hamedoun[1] · H. Ez-Zahraouy[2] · E. Salmani[2] · A. Benyoussef[1,2]

Received: 15 February 2017 / Accepted: 11 April 2017

Abstract The magnetic properties of Fe_3O_4, with the presence of Fe and O vacancy atoms, were carried out using the KKR-CPA method in density functional theory (DFT) implemented in the MACHIKANYAMAv2009 package, by considering local density approximation (LDA) and local density approximation-self-interaction-correction (LDA-SIC) approximations. Our study presents total, atoms projected density of states (DOS), and magnetic moments of different atoms in Fe_3O_4 with and without vacancy atoms; we provide an atomic level insight for magnetite which is a necessary step to understand their electronic, half-metallicity, and magnetic properties. We also noticed that the half-metallic behaviors of Fe_3O_4 contribute to a better understanding of the utility of this material in spintronic applications.

Keywords Fe_3O_4 · Spinel ferrites · Spintronic · Ab initio calculation · KKR-CPA · Fe and O vacancies

1 Introduction

Since the discovery of the spintronic field in the 1980s, scientists and researchers have been focused on the investigation of materials with a high spin polarization [1]. The spinel ferrites form a wide class of transition metal oxides with electronic and magnetic properties potentially interesting in spintronic application [2]. The most known material of this family is the magnetite (Fe_3O_4) which has been studied in numerous works because of its half-metallic behavior at room temperature, its Verwey transition temperature from half-metal to insulator compound ($T_V = 120$ K), and its ferrimagnetism below Curie temperature [3]. Since the X-ray analyses performed by Bragg et al. in 1915 [4], magnetite is known to crystallize in the cubic inverse spinel structure showing a ferromagnetic phase that originates from the magnetic moment of anti-parallel spins between Fe^{3+} ions at tetrahedral sites (A-sites) and both Fe^{3+} and Fe^{2+} ions at octahedral sites (B-sites) [5]. The defects which may exist in magnetite are varied; they may correspond to oxygen atom vacancies or cation vacancies, to the presence of cations in normally empty atomic sites, or to changes in atomic sites for certain Fe atoms. The two-dimensional defects are also added such as the anti-phase walls which appear when the stacking of different atomic planes is different from that of the solid crystal. All these anomalies in the atomic structure are responsible for a more or less local modification of the electronic structure [6–10]. In this work, we aim to investigate the effect of Fe and O vacancies atoms on the half-metallic and ferromagnetic behaviors of Fe_3O_4. We organized this paper as follows: in Section 2, we describe the computational approach used in this work; discussion of results is given in Section 3, while Section 4 is reserved for the conclusion.

2 Computational Details

In the present work, the calculations are based on the density functional theory [11] by using the Korringa-Kohn-Rostoker Green's function method combined with the coherent

✉ O. Mounkachi
o.mounkachi@gmail.com; o.mounkachi@mascir.com

1 Materials and Nanomaterials Center, MAScIR Foundation, Rabat Design Center, Rue Mohamed Al Jazouli – Madinat Al Irfane, Rabat, 10 100, Morocco

2 LMPHE Laboratory, Faculty of Science, Mohammed V University, B.P. 1014, Rabat, Morocco

Published online: 02 May 2017

Ceramics International 43 (2017) 14401–14404

Contents lists available at ScienceDirect

Ceramics International

journal homepage: www.elsevier.com/locate/ceramint

Exploring the magnetic and structural properties of Nd-doped Cobalt nano-ferrite for permanent magnet applications

O. Mounkachi[a,*], R. Lamouri[a,b], B. Abraime[a,b], H. Ez-Zahraouy[b], A. El Kenz[a], M. Hamedoun[a], A. Benyoussef[a,b,c]

[a] Materials and Nanomaterials Centre, Moroccan Foundation for Advanced Science, Innovation and Research, MAScIR, Rabat, Morocco
[b] Laboratoire de Matière Condensée et Sciences Interdisciplinaires (LaMCScI), B.P. 1014, Faculty of Science-Mohammed V University, Rabat, Morocco
[c] Hassan II Academy of Science and Technology, Rabat, Morocco

ARTICLE INFO

Keywords:
Cobalt ferrite nano-particles
$CoFe_2O_4$
Magnetic proprieties
Permanent magnets application

ABSTRACT

$CoFe_2O_4$ and $Co_{0.5}Nd_{0.5}Fe_2O_4$ spinel ferrites have been synthesized by coprecipitation method, X-ray diffraction (XRD), Transmission electron microscopy (TEM), and superconducting quantum interference device magnetometer (SQUID) techniques were used to characterize crystal structure, morphology and magnetic properties. Spinel structure of single phase is obtained according to XRD results for both samples. From TEM characterization results, we obtained a spherical morphology for $CoFe_2O_4$ with an average of 8.71 nm and a nanorod morphology for Nd doped Cobalt ferrite with a particle diameter of about 6 nm and length of 40 nm. According to the hysteresis loop, $Co_{0.5}Nd_{0.5}Fe_2O_4$ exhibits a maximum energy product $(BH)_{max}$ of 0.431 MGOe (3.434 kJ/m^3) at room temperature, with an enhancement of 7% compared to pure cobalt ferrites nanoparticles, which prove the efficiency of this material in permanent magnets application.

1. Introduction

Nano-structured materials have proven their various applicabilities with the increased demand for size reduction materials. Nd-Fe-B and Sm-Co systems have taken for many years the interest of researchers as efficient permanent magnets. Although, the high synthesis cost and low corrosion resistance have turned research towards materials that can replace these systems such as ferrites materials [1]. Nanoparticles of spinel ferrites have been largely used in different applications, because of their properties, such as electronic circuits [2], high-frequency systems [3], power delivering devices [4], permanent magnets [5] and many others [5–12], which make this family a fairly wide field of research. Cobalt ferrite is considered as one of the most important material in the spinel family because of its interesting properties such as good chemical stability, low synthesis cost, high coercivity and significant saturation magnetization. These properties influence the magnetic properties of the material, in particular, the maximum energy product $(BH)_{max}$ [13], which is the main characteristic of a permanent magnet. Cobalt ferrite crystallizes in the cubic inverse spinel structure where half of the trivalent Iron cations (Fe^{3+}) occupy tetrahedral sites and the octahedral sites are shared by divalent cations of Cobalt (Co^{2+}) and the remaining trivalent cations [14]. On the basis of its properties, Cobalt nano-ferrite has been intensively investigated using different synthesis methods such as auto-combustion method [15], Co-precipitation method [16] and others [17–19]. Others have explored the exchange spring behavior in hard/soft ferrite Nano composite in order to obtain high energy products [20–23]. Thus, optimizing the synthesis parameters and varying Cobalt nano-ferrite composition could improve their properties. Cobalt spinel ferrite is considered to be one of the most important materials in the spinel family for permanent magnets application because of its interesting magnetic properties (strong coercive field). These intrinsic properties influence its total magnetic properties, in particular the maximum energy product $(BH)_{max}$, which is the main characteristic of permanent magnets. But the $(BH)_{max}$ found until now remains low. In our study, we are looking to enhance the magnetic properties of $CoFe_2O_4$, in particular, the maximum energy product $(BH)_{max}$ by doping the Cobalt (Co) by neodymium (Nd). We have used coprecipitation method to prepare pure and neodymium doped $CoFe_2O_4$ nanoparticles and then we have measured magnetic properties such as blocking temperature, remanence, coercivity and maximum energy product which shows an enhancement of 7% of $(BH)_{max}$ compared to the pure Cobalt ferrite nanoparticles.

2. Experimental details

We have used $FeCl_2{\cdot}4H_2O$, $NdCl_3$, $FeCl_3{\cdot}6H_2O$, $CoCl_2{\cdot}6H_2O$ and

* Corresponding author.
E-mail addresses: o.mounkachi@gmail.com, o.mounkachi@mascir.com (O. Mounkachi).

http://dx.doi.org/10.1016/j.ceramint.2017.07.209
Received 12 June 2017; Received in revised form 27 July 2017; Accepted 29 July 2017
Available online 29 July 2017

Journal of Magnetism and Magnetic Materials 436 (2017) 6–10

Contents lists available at ScienceDirect

Journal of Magnetism and Magnetic Materials

journal homepage: www.elsevier.com/locate/jmmm

Research articles

Effect of the cations distribution on the magnetic properties of $SnFe_2O_4$: First-principles study

R. Lamouri [a,b], M. Tadout [a,b], M. Hamedoun [a], A. Benyoussef [a,b,c], H. Ez-zahraouy [b], M. Benaissa [b], O. Mounkachi [a,*]

[a] Materials and Nanomaterials Center, MAScIR Foundation, Rabat Design Center, Rue Mohamed Al Jazouli – Madinat Al Irfane, Rabat 10 100, Morocco
[b] LaMCScI (ex LMPHE), B.P. 1014, Faculty of Science-Mohammed V University, Rabat, Morocco
[c] Hassan II Academy of Science and Technology, Rabat, Morocco

ARTICLE INFO

Article history:
Received 19 January 2017
Received in revised form 10 March 2017
Accepted 29 March 2017
Available online 31 March 2017

Keywords:
$SnFe_2O_4$
Spinel ferrites
Spintronic
Ab initio calculation
FP-LAPW method

ABSTRACT

In this work, a study of the electronic and magnetic properties of $SnFe_2O_4$ spinel ferrite for different case of octahedral and tetrahedral distribution was carried out by using the Full Potential Linearized Plane Wave (FP-LAPW) method in density functional theory (DFT) implemented in the WIEN2K package, with the generalized gradient (GGA) and Tran-Blaha modified Becke-Johnson approximations for the exchange and correlation functional. Our spin-polarized calculations based on mBJ correction show a half metallic behavior for $SnFe_2O_4$ which confirm the usefulness of $SnFe_2O_4$ in spintronic application. From the magnetic properties calculations, it is found that the magnetic moment per formula unit is 8.0327 μ_β, 0.000015 μ_β and 3.99μ_β in $SnFe_2O_4$ 100% normal, 100% inverse and 50% inverse, respectively.

1. Introduction

For many years, ferrite compounds have been the subject of several investigations, because of their potential applications in many industrial fields such as microwave devices [1], inductance components [2], magnetic refrigeration [3], photocatalytic [4] and many others [5–8]. These applications depend on the ferrites properties: magnetic properties, electrical resistivity and losses, and a good chemical stability. In nature, ferrites exist in three different crystal systems which have specific properties tailor to specific application. The spinel ferrites structure was determined for first time by Bragg [9]. It has the general formula AFe_2O_4, where A is a metal transition element. We distinguish between three categories of spinel ferrites according to the distribution of cations among the tetrahedral and octahedral sites, which largely changed the magnetic properties of the system. Nanocrystalline Tin ferrite ($SnFe_2O_4$) was investigated experimentally by using various synthesis methods [10–12]. Drokin et al. [13] presented the spectral temperature of the photoconductivity in polycrystalline samples of doped tin ferrite $Sn_xFe_{3-x}0_4$ (x = 0, 0.1, 0.2, 0.3, 0.4, 1). Liu et al. [14] characterized nanoparticles of SnFe204, synthesized by the co-precipitation method relatively to low temperature. Berry et al. [15] studied $Sn_{o.1}Fe_{2.9}O_4$ by Mossbauer spectroscopy. R.K. Gupta et al. [16,17] interested to the epitaxial tin ferrite thin films using KrF excimer pulsed laser deposition technique. Up to now, theoretical and numerical studies are focused on spinel ferrites others than tin ferrite by different methods of ab initio calculations such as ASW, FPLO, LAPW and others, for normal and inverse spinel [18–23]. Our work is devoted to the investigation of magnetic properties of bulk $SnFe_2O_4$ by considering the three different categories of cationic distribution: Normal, inverse, and an intermediate spinel ferrite. We organize this paper as follows: in Section 2, we describe the computational approach used in this work. The electronic and magnetic properties are given and discussed in Section 3, while, Section 4 is reserved for the conclusion

2. Computational details

In this work, the calculations are performed by using the Density Functional Theory (DFT) within the Full Potential Linearized Augmented Plane Wave (FP-LAPW) implemented in the WIEN2K package [21]. For which the exchange-correlation energy is described by the Generalized Gradient Approximation proposed by Perdew, Burke, and Ernzerhof (GGA-PBE) [24,25], and we used the modified Becke-Johnson correction (mBJ) to obtain the self-consistency. The atomic spheres are expanded up to the angular

* Corresponding author.
E-mail addresses: o.mounkachi@mascir.com, o.mounkachi@gmail.com (O. Mounkachi).

http://dx.doi.org/10.1016/j.jmmm.2017.03.075
0304-8853/

Band-Gap Engineering of CdS, CdSe and ZnSe : First-Principles Calculations

Rachida Lamouri*[1], El mehdi Salmani[1],
Hamid Ez-zahraouy[1] and Abdelilah Benyoussef[1,2,3]
[1]LMPHE, Department of Physics,
Faculty of Sciences, University Mohammed V
Rabat, Morocco
* rachida.lamouri@gmail.com

[2] Institute of Nanomaterial's and
Nanotechnology MASclR
Rabat, Morocco
[3] Hassan II Academy of Science and
Technology
Rabat, Morocco

Abstract— **The electronic structures of CdS, CdSe and ZnSe bulk and thin films materials are carried out Using the first principles calculations based on the Korringa-Kohn-Rostoker method (KKR) combined with the Coherent Potential Approximation (CPA).It is found that the band gaps of those materials in the case of thin films with 2, 4 and 8 layers are larger than the one of the bulk with Zinc blende structures and decreases with increasing the film thickness.**

Keywords- II-VI Semiconductors; CdS; CdSe; ZnSe; Band-gap Engineering; Multilayer; KKR-CPA.

I. INTRODUCTION

The II-VI semiconductors compounds have received considerable attention as important semiconductors because of their extensive industrial application in solar cell, and other modern technologies. The photovoltaic technology represents one of the most important branches of the high-technology industry. Among the materials that have been investigated, binaries CdS, CdSe and ZnSe compounds are very interesting due to their applicability [1]. Solar cells based on CIGS, consisting of a stack of thin layers, in particular contain a thin layer called the buffer layer between the absorber and the front contact, necessary for obtaining high conversion efficiencies [2-5]. This buffer layer is currently generally composed of sulphide Cadmium (CdS) and present a major environmental problem because cadmium is a carcinogenic element which although present in very low quantities in the cell (approximately 0.9% of the mass of standard stack off the substrate and encapsulation) and can be recycled at end of life panels, represents a potential danger during storage on production sites and is not in line with the green energy image conveyed by energy solar [6].

It goes without saying, the crystals CdS, CdSe and ZnSe crystallizes in two distinct forms, zinc-blende and Wurtzite forms. Of these forms, zinc-blende is the most stable, and as such, the most suitable for studying their electronic properties.

Using the GW approximation , the electronic structure of CdS, CdSe and ZnSe were investigated by Zakharov et al. [7]. Rodriguez et al. [8] studied the electronic projected bulk band structure, surface band structure and the wave vector resolved density of state for II-VI semiconductors using the tight binding scheme. Other studies have been carried out for the alloys of these semiconductors [9-12].

In the present work, the electronic band structure of CdS, CdSe, And ZnSe bulk and thin films compounds using first-principle calculations are proposed for photovoltaic application. We organized this paper as follows: in section 2, we describe the computational approach used in the work. Band structures are presented and discussed in section 3 while section 4 is reserved for conclusion.

II. COMPUTATIONAL DETAILS

The electronic structure is studied using the density-functional theory [13] based on the Korringa–Kohn–Rostoker method combined with the coherent potential approximation (KKR-CPA , the parameterization of Moruzzi, Janak, and Williams (MJW) and Vosko, Wilk, and Nusair (VWN) has been used for the parameterization of the exchange energy[14].

The KKR-CPA-LDA package as implemented into MACHIKANEYAMA2002 [15] is used for a more realistic description of this materials under investigation. The CPA treatment is considered one of the most efficient band structure calculation . K-points up to 425 in the irreducible part of the first Brillouin zone were used with the KKR-CPA code package [16] throughout all calculations. The relativistic effects have been considered using the scalar relativistic approximation and the real harmonics up to $l = 2$, where l is the angular momentum defined at different sites.

All studied CdS, CdSe and ZnSe layers, of various thicknesses (2, 4 and 8 layers), are constructed from 3D zinc-blende structure. The optimized structures are obtained by calculating the total energy of compounds as a function of their volumes. The minimum value for the energy was obtained for a

978-1-5090-5713-9/16/$31.00 ©2016 IEEE

Opt Quant Electron (2017)49:97
DOI 10.1007/s11082-017-0932-8

Electronic, optical and magnetic properties of TM (Cr and Fe) doped Titania TiO_2: Ab initio calculations, mean field approximation and Monte Carlo simulation

El Mehdi Salmani[1] · Ayoub Laghrissi[1,3] · Rachida Lamouri[1] · Mustapha Dehmani[1] · El Mostafa Benchafia[2] · Hamid Ez-Zahraouy[1] · Abdelilah Benyoussef[4,5]

Received: 30 September 2016 / Accepted: 30 January 2017

Abstract TiO_2:TM (TM: Cr and Fe) based dilute magnetic semiconductors are investigated within self-interaction-corrected local density approximation (SIC-PBE) from first-principles calculation. These results are compared with those calculated within standard PBE, In this system, the stability of the ferromagnetic state compared with the spin-glass state is investigated by comparing their total energies. The Ferromagnetic and half metallic behaviors was observed and conformed with the local-moment-disordered state energy for PBE and PBE-SIC approximation in $[Ti_{0.95}\ TM_{0.05}$ (Cr and Fe)$]O_2$. The exchange interactions obtained from first principle calculations and used in a classical Ising model by a Monte Carlo approach resulted in ferromagnetic states with Curie temperatures within the ambient conditions.

Keywords First-principles calculation · Self-interaction correction · TiO_2 · Monte Carlo approach

1 Introduction and motivation

In order of decreasing abundance, Titania (TiO_2) crystallizes in four distinction polymorphs: rutile, anatase, brookite and An–TiO_2 (Labat et al. 2007; Martienssen and Madelung). Of these forms, rutile TiO_2 is the most stable, and as such, the most suitable for

✉ Mustapha Dehmani
dehmani01@yahoo.fr

[1] LMPHE, Faculté des Sciences, Université Mohammed V, Rabat, Morocco

[2] Department of Materials Science and Engineering, New Jersey Institute of Technology, Newark, NJ 07102, USA

[3] Institute for Materials & Surface Technology (IMST), HAW Kiel-University of Applied Sciences, Grenztrasse 3, 24149 Kiel, Germany

[4] Institute for Nanomaterials and Nanotechnologies, MAScIR, Rabat, Morocco

[5] Académie Hassan II des Sciences et Techniques, Rabat, Morocco

Published online: 09 February 2017

Journal of Magnetism and Magnetic Materials 422 (2017) 348–355

Contents lists available at ScienceDirect

Journal of Magnetism and Magnetic Materials

journal homepage: www.elsevier.com/locate/jmmm

The electronic, magnetic and optical properties of ZnO doped with doubles impurities (Cr, Fe): An LDA-SIC and Monte Carlo study

El Mehdi Salmani [a,*], Ayoub Laghrissi [a], Rachida Lamouri [a], Hamid Ez-Zahraouy [a], Abdelilah Benyoussef [b,c]

[a] LMPHE, Faculté des Sciences, Université Mohammed V, Rabat, Morocco
[b] Institute for Nanomaterials and Nanotechnologies, MAScIR, Rabat, Morocco
[c] Académie Hassan II des Sciences et Techniques, Rabat, Morocco

ARTICLE INFO

Article history:
Received 19 May 2016
Received in revised form
2 September 2016
Accepted 3 September 2016
Available online 7 September 2016

Keywords:
Diluted semiconductor
Half-metallic ferromagnetic
Self interaction corrected local density approximation (SIC-LDA)

ABSTRACT

Electronic structure, magnetic and optical properties of ZnO doped with single and double impurities $\mathbf{Zn_{1-x}Cr_xO}$, $\mathbf{Zn_{1-x}Fe_xO}$, and $\mathbf{Zn_{1-2x}Cr_xFe_xO}$ (x=0.03 and 0.06) are investigated using first-principles calculations. Based on the Korringa–Kohn–Rostoker method combined with the coherent potential approximation, we investigated the half-metallic ferromagnetic behavior of doubles impurities (Cr, Fe) doped ZnO. To support our results, we apply the self-interaction-corrected local density approximation (SIC-LDA) to study the electronic structure, optical and magnetic properties of Co-doped ZnO with doubles impurities (Cr, Fe) showing that the half-metallic ferromagnetic state still persists. The stability of the ferromagnetic state compared with the spin-glass state is investigated by comparing their total energies. The exchange interactions obtained from first principle calculations and used in a classical Ising model by a Monte Carlo approach resulted in ferromagnetic states with high Neel temperature.

1. Introduction

During the last decade, a lot of interest has been devoted to diluted magnetic semiconductors (DMS) considered as one of the materials for spintronics application, where both charge and spin are considered. The DMS are objects that offer the possibility to control properties related to the charge and spin of electrons. The introduction of ferromagnetic order in DMS expands its already wide range of applications into the emerging domain of spintronics. The most investigated candidates are those based on ZnO, GaN, TiO2, and SnO2 because of their ferromagnetic (FM) property observed at high Curie temperature under special conditions [1–5].

ZnO is an attractive semiconductor for solid state blue to UV optoelectronic including laser development. Transparency to visible light provides opportunities to develop transparent electronics, UV optoelectronic, and integrated sensors, all from the same material system. ZnO is a semiconductor with direct band gap Eg=3.37 eV. Doping with certain transition metals yields ferromagnetism. Moreover, zinc oxide is a well-known piezoelectric and electro-optic material, and can be easily deposited in thin film [6]. As ZnO is usually n-type doped with free carriers in the conduction band or p-type with free holes carriers in the valence band.

In case of semiconductor spintronic materials, Half-metallic (HM) materials are defined as those which are insulating for one spin direction (spin down, say) but metallic for other spin channel (spin up), there electronic density of states is completely spin polarized on the Fermi level and the conductivity are dominated by these metallic single-spin charges carriers. This property can be generally referred to as half-metallic ferromagnetic (HM-FM), which was first introduced by Groot et al. [7], based on their electronic structure calculations for Heusler systems NiMnSb and PtMnSb. A consequence of half-metallicityis that the spin magnetization is always an integer number of Bohr magnetons per unit cell. Usually, the ideal case of research on HM materials would be a half-metallic antiferromagnetic (HM-AFM). There are several structures which can be considered as possible candidates such as half Heusler, which was the first HM-AFM material predicted on the basis of Heusler compound (V 7 MnFe 8 Sb7) and proposed by Van Leuken and de Groot [8]. As shown recently by Akai and Ogura [9], in diluted magnetic semiconductors (DMS) systems, local magnetic states are formed at the impurity bands that appear in semiconductor gap. Similarly, half metallic antiferromagnetic diluted magnetic semiconductors can be realized for impurities bands in the gap. However, the existence of such materials has not been verified experimentally. Since by molecular beam epitaxy, many thermodynamically unstable systems can be produced. This

* Corresponding author.
E-mail addresses: elmehdisalmani@gmail.com, salmanielmehdi@gmail.com (E.M. Salmani).

http://dx.doi.org/10.1016/j.jmmm.2016.09.027
0304-8853/

Abstract

Permanent magnet materials have attracted a lot of interest of researchers worldwide because of their use in many technological and industrial applications. The largest market of permanent magnets is essentially made up of rare-earth based magnets or ferrites magnets. However, it should be noticed that each permanent magnet application is particular and responds to specific needs, and therefore to different conditions. The present thesis work was focused on Cobalt spinel ferrites $CoFe_2O_4$ and M-type Strontium hexaferrites $SrFe_{12}O_{19}$ by studying their structural, electronic and magnetic properties using a combination of theoretical and experimental investigations. Our theoretical results based on density functional theory and Monte Carlo simulation showed the strong dependence of the magnetic properties of Cobalt spinel nanoferrites to the nanoparticles size and we extracted a theoretical value of the maximum energy product $(BH)_{max}$ of about 2.83 MG.Oe for cubic-shaped $CoFe_2O_4$ nanoparticles with an average particle size of about 21 nm. A possibility to enhance the maximum energy product $(BH)_{max}$ of the M-type strontium hexaferrites has been proved experimentally by varying the synthesis methods and through the preparation of hard/soft nanocomposites with the presence of the exchange-coupling behavior.

Keywords: Spinel ferrites, M-type hexaferrites, Density Functional Theory, Monte Carlo simulation, Co-precipitation method, Sol-gel auto-combustion, Solid-State reaction, Magnetic properties, Permanent magnet applications.

Résumé

Les matériaux pour aimants permanents ont suscité beaucoup d'intérêt de la part des chercheurs du monde entier en raison de leur utilisation dans de nombreuses applications technologiques et industrielles. Les aimants à base de terres-rares ou de ferrites constituent le marché le plus large des aimants permanents. Cependant, il convient de noter que chaque application d'aimant permanent est particulière et répond à des besoins spécifiques et donc à des conditions différentes. Le présent travail s'est concentré sur les ferrites spinelles "$CoFe_2O_4$", et les hexaferrites de type-M "$SrFe_{12}O_{19}$", en étudiant leurs propriétés structurelles, électroniques et magnétiques grâce à une combinaison d'études théoriques et expérimentales. Nos résultats théoriques basés sur la théorie de la fonctionnelle de la densité et la simulation de Monte Carlo montrent la forte dépendance des propriétés magnétiques des ferrites spinelles de Cobalt à la taille des nanoparticules et nous avons extrait une valeur théorique du produit énergétique maximal $(BH)_{max}$ d'environ 2,83 MG.Oe pour une taille moyenne de particule de 21 nm. La possibilité d'améliorer le $(BH)_{max}$ des hexaferrites de strontium de type-M a été prouvée expérimentalement en variant les méthodes de synthèse et en utilisant des nano-composites durs/doux avec un comportement de couplage d'échange.

Mots-clés : Ferrites spinelles, Hexaferrites de type-M, Théorie de la fonctionnelle de la densité, Simulation Monte Carlo, Méthode de co-précipitation, Méthode de sol-gel auto-combustion, Réaction à l'état solide, Propriétés magnétiques, Applications des aimants permanents.